Development of a Bypass Current Model in Modular Alkaline Water Electrolysis

Simulation and Application of 3D Models

F.B.E. Kolff

Technische Universiteit Delft

TU Delft

Development of a Bypass Current Model in Modular Alkaline Water Electrolysis

Simulation and Application of 3D Models

by

F.B.E. Kolff

to obtain the degree of Master of Science
at the Delft University of Technology,
to be defended publicly on Monday February 19, 2024 at 14:00 PM.

Student number:	4715179	
Project duration:	May 22, 2023 – February 2, 2024	
Thesis committee:	Prof. dr. K. Hooman,	TU Delft, chair and supervisor
	Dr. O.A. Moultos,	TU Delft
	Dr. ir. M.J.B.M. Pourquie,	TU Delft
	Dr. ir. A. Rahbari,	XINTC B.V., daily supervisor

This thesis is confidential and cannot be made public until February 12, 2026.

Acknowledgements

Just over eight months ago, I started on my master's thesis. After completing a bachelor's in a different degree, Life Sciences & Technology, the start of my master's had been bumpy. As it slowly got better, instead of dreading such a large project as my thesis, I began looking forward to it. Even though almost every technique used in this thesis was new to me, I am proud of what this project has become. While only my name appears on the front, it is important to acknowledge the invaluable assistance I received from a few others without whom this would not have been possible.

First of all, I could not have completed this thesis without Ahmadreza, my daily supervisor. Your level of involvement in both the research of XINTC and my thesis impresses me a lot. You always had time to help me with small or big challenges. I enjoyed the meetings, especially your endless drive to optimise and refine our product, but also the many discussions about languages and the numerous quirks of living in the Netherlands. I am grateful for the opportunity to work under your supervision.

I want to show my appreciation to Kamel, my supervisor from TU Delft. Even before I started my thesis, you helped me think critically about what I wanted to do. Even though our weekly meetings were not so weekly, you always made the time to meet with me and figure out how I could best proceed with my project. I value all the feedback and input you gave me over the past couple of months.

Also, I would like to thank all my other colleagues at XINTC in both Delft and Eerbeek. In particular, I would like to thank Owen for all his help with the experiments. Especially when the setup had to be often changed, you stayed just as excited as me to see the outcome of the results. To all other colleagues: thank you for my great time at XINTC, and I wish you the best!

And lastly, I want to say thanks to my family and friends. You have supported me for the past couple of years, and I am very grateful for that. To everyone who motivated me throughout my thesis and studies, listened to my stories, made my student life a great time, or for a hundred other reasons: I am thankful to have you!

Fenna B.E. Kolff
Delft, February 2024

Abstract

The world is witnessing unprecedented climate changes, which have worsened over the past couple of years. Despite significant progress in renewable energy, achieving a reduction of global warming remains challenging. Renewable energy sources like solar, wind, and hydroelectric technologies offer promising solutions, but challenges persist due to their intermittency and geographical dependency. Green hydrogen, generated through electrolysis using renewable energy, has come up as a solution for storing electric energy and providing a constant energy supply.

Alkaline water electrolysis has emerged as one the most promising electrolysis methods due to its large-scale operation, long durability and low costs. This does not come without challenges, one of them being leakage currents, which reduces the efficiency of the electrolyser. Leakage currents occur when not all current is used for hydrogen production, but some of it leaks into, for example, the produced hydrogen stream.

To reduce these leakage currents, more research into the origins is needed. The first step is modelling the electrolysis while considering as much as possible of the physics happening inside the system. Current models of alkaline water electrolysers are either modelled using only mathematical equations or neglect the operating parameters, which makes the results highly variable per system. Other models do use analytical methods with experimental results, but these models only comprise one electrolysis cell rather than a full stack.

This work consists of developing two three-dimensional models, validating them using experiments, and using them to predict the effect of changes in geometry. The first model was made using COMSOL Multiphysics software and used to research the water electrolysis stack, which comprised one or eight cells using electrochemical relations and physical data. It was found that a model could be made that fitted the experiments within the error margin of the experiments (<2.5%). It lacked flexibility but overall showed good results for an electrolyser stack of one or eight cells. The second model was made using an equivalent electrical circuit (EEC) of the electrolyser in Python via the PySpice module. A steady-state model, including the leakage currents, could be developed by calculating all system resistances, namely the cell, inlet/outlet, and manifold resistances. This model overestimated the performance of the electrolyser by 10-15% for low current densities and 2-4% for high current densities. Nevertheless, it was highly adaptable for different scenarios, making it valuable for research into optimising the electrolysis stack. Both models were used to predict the effect of changes in geometry; the effect of the length of the inlets, and the number of cells. This showed that the EEC model was better suited for this research.

Contents

List of Figures

List of Tables

Nomenclature

Table 1: List of abbreviations

Abbreviation	Definition
AWE	Alkaline Water Electrolyser
CAPEX	Capital Expenditures
EEC	Equivalent Electrical Circuit
GHG	Greenhouse Gas
HER	Hydrogen Evolution Reaction
KOH	Kalium Hydroxide
OER	Oxygen Evolution Reaction
OPEX	Operating Expenditures
PEME	Proton Exchange Membrane Electrolyser
SOE	Solid Oxide Electrolyser

Table 2: List of symbols

Symbol	Definition	Unit
A	Area	[m^2]
d	Length	[m]
D	Diameter	[m]
$E°$	Cell potential or cell voltage	[V]
f	frequency factor or external forces or friction factor	[-] or [kg m s^{-2}] or [-]
F	Faraday constant	96,485 [C mol^{-1}]
g	Gravitational constant	9.81 [m s^{-2}]
i or I	Current	[A]
j or J	Current density	[A m^{-2}]
h	Height	[m]
$k°$	Standard rate constant	[mol s^{-1}]
K	Reaction rate or frictional loss coefficient	[-]
l/L	Length	[m]
m	Concentration	[mol L^{-1}]
M	Molar mass	[kg $mol^{-}1$]
$\dot{n}$	Hydrogen production rate	[kg s^{-1}]
N_c/N_{cell}	Number of cells	[-]
P	Pressure or power	[bar] or [W]
$Q/\dot{Q}$	Heat/ heat rate	[J]/[J s^{-1}]
R	Resistance or gas constant	[Ω] or 8.314 [J mol^{-1} K^{-1}]
t	Time	[s]
T	Temperature	[°C]
u	Velocity	[m s^{-1}]
V	Voltage	[V]
wt	Weight percentage	[%]
z	Number of electrons transferred per reaction	[-]
α	Charge transfer coefficient	[-]
ΔG	Gibbs free energy change	[J]
ΔH	Reaction enthalpy	[J]
ΔS	Reaction entropy	[J K^{-1}]
ϵ	Void fraction electrolyte	[-]
ϵ_s	Porosity membrane	[-]
η	Efficiency or overpotential	[%] or [V]
θ	Gas surface coverage	[-]
κ	Specific electrical conductivity	[$\Omega^{-1}m^{-1}$]
μ	Viscosity	[kg $m^{-1}s^{-1}$]
ρ	Density	[kg m^{-3}]
σ	Conductivity	[$kg^{-1}m^{-3}s^3A^2$]
τ_s	Tortuosity	[-]
Φ	Volume fraction	[-]
ω	wettability or vorticity	[-] or [-]

Table 3: List of subscripts

Subscript	Definition
a/act	activation
an	anodic
b	bubble
c/cath	cathodic
c/cell	cell
con	concentration
e	outlet
eq	equilibrium
exp	expansion
f	friction
F	Faraday
g	gas
gen	generation
H	hydraulic
i	inlet
l	liquid
loss	losses
m	mixture or manifold
ohm	ohmic
ox	oxidation
P	pressure
red	reduction
ref	reference
rev	reversible
s	separator
stack	stack
t	tube
T	temperature
tn	thermo-neutral
volt	voltaic
w	water

1 Introduction

As the world grapples with the alarming rise in forest fires, hurricanes, heatwaves, and floods, it has become undeniably clear that the climate is undergoing unprecedented changes. These harrowing events, along with the overwhelming abundance of social media items, scientific papers, and films on the subject, underscore the urgency of the climate crisis. The root cause of this climate change phenomenon lies in global warming, which has steadily worsened over the past two centuries. Unless decisive actions are taken, the situation will continue to escalate [1]. The large increase in research into renewable energy sources and storage methods has yielded significant progress in the past decade. Despite these advancements, achieving the critical goal of keeping global warming below 2°C, as set in the 2015 Paris Agreement - one of the most widely accepted climate treaties, remains a monumental challenge [2].

1.1. Future of Energy

No. 1 of the seven key recommendations to scale up hydrogen by the IEA is to establish a role for hydrogen in long-term energy strategies, with one of them focusing on revising the electricity grid and stimulating solutions that facilitate the variable energy generation from renewables [3]. Two primary challenges must be overcome to pave the way for a future of widespread green energy. The first challenge revolves around the maturity of renewable sources, which requires more research and development to enlarge the scale of operation and reduce costs. While substantial strides have been taken in recent decades, the renewable energy market has not reached its full potential in terms of scale and price [4, 5]. The best alternatives to replace fossil fuels are solar, wind, and hydroelectric technologies [6, 7]. The second challenge is the intermittency of solar and wind power, while hydroelectricity is highly dependent on geographical position. The location can improve the intermittent nature of the former two but is still dependent on weather and seasonal effects [8].

The Dutch government has greenhouse gas (GHG) reduction targets of 49% by 2030 and 95% by 2050 (compared to 1990) [9]. Aside from more energy production from renewables, the energy must be stored efficiently to compensate for fluctuations to reach those targets. In this context, green hydrogen emerges as a vital enabler. In 2021, the Netherlands had an electrolyser capacity of only 3MW, and this is set to grow to 3-4GW by 2030 and to 13-45GW in 2050 [10, 11].

Using hydrogen, electric energy can be stored, and this is currently one of the most intensively researched renewable storage methods. Its versatile applications range from replacing fossil fuels in various sectors to providing storage for surplus renewable energy, thus ensuring a constant energy supply. Implementing an effective energy buffering system utilising hydrogen will contribute to a more flexible and resilient energy infrastructure [1, 9, 12, 13].

Currently, electrolysis contributes to less than 4% of green hydrogen production, while the majority is derived from fossil fuels [6, 14]. To reduce the dependence on fossil-produced hydrogen, the share of hydrogen produced using renewable energy needs to be increased. Among the most feasible renewable options, solar and wind energy stand out due to their widespread distribution [6, 7]. These renewable sources offer the potential to produce large amounts of hydrogen without carbon dioxide emissions or other pollutants associated with fossil fuels [15].

1.2. Generation of Hydrogen

Within the landscape of hydrogen production technologies, alkaline water electrolysis has emerged as a crucial and most promising method for sustainable hydrogen gas generation, which plays a pivotal role in the transition towards a clean and renewable energy landscape. It has a 59% market share within the global electrolyser market, and the total market is set to grow from an estimated 0.5-3.7 billion USD in 2023 to 7.1-34.3 billion USD in 2032 [16, 17]. In recent years, there has been increasing interest in the design, development, and optimisation of alkaline water electrolysers due to their potential in large-scale hydrogen generation [18]. Alkaline water electrolysis is a mature method of producing hydrogen from water, which uses electricity to dissociate water into oxygen and hydrogen gas. It is more robust than other electrolysis technologies because it uses less critical materials and has a longer lifetime; therefore, in this work, the focus lies on alkaline water electrolysis. The hydrogen produced from this method has a high purity of 99.5% up to 99.999% [14].

While the concept of alkaline water electrolysis is straightforward, its practical implementation requires precise engineering and material selection to optimise performance and ensure prolonged operation. Electrical costs can be up to 90% of the total operating costs (OPEX) of hydrogen production and up to 70% of the total costs (OPEX and CAPEX), so it is quite interesting to improve the efficiency of electrolysers and therefore reduce the hydrogen costs [19].

1.3. Optimisation of Hydrogen Production

While alkaline water electrolysis offers numerous advantages, it is not without challenges. One critical issue that demands attention is the presence of leakage currents, which can significantly impact the overall efficiency of alkaline water electrolysis systems. Leakage currents, also known as shunt currents or parasitic currents, have emerged as a substantial concern in the operation of alkaline water electrolysers. These currents, often induced by unintended defects or imperfections in the electrolysis system, result in the diversion of electric current away from the desired electrolysis reactions. Instead, the electrons follow unwanted pathways [20]. Figure 1.1 shows a simplified electrolysis stack, with the electrolysis cells as grey rectangles. All inlets and outlets are shown in green and are connected in parallel. The leakage currents can travel via these pathways, visualised as the dotted lines. These leakage currents lead to energy losses, reduced efficiency, and possible safety hazards. Identifying and mitigating these leakage currents are thus vital to enhance the overall performance and reliability of alkaline water electrolysers [21, 22].

1.4. Thesis Outline

As stated above, it is important to extend the knowledge of leakage currents by identifying and reducing them. These insights can then be used to optimise the electrolysis stack and achieve higher efficiencies in producing green hydrogen. This thesis can be divided into two parts: the first part will focus on building two three-dimensional models of a test stack in collaboration with

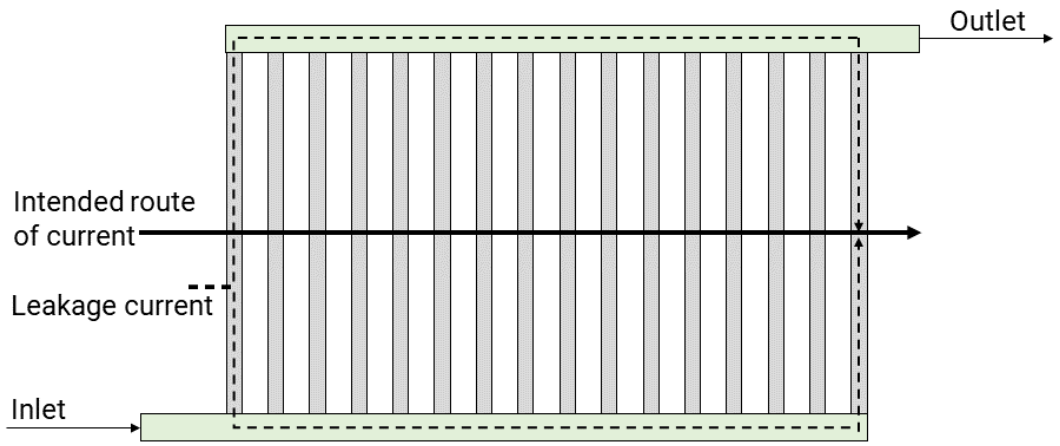

Figure 1.1: Schematic of leakage currents. The electrolyte and product streams are indicated in green, while the electrolysis cells are grey. The leakage current does not follow all electrodes but is diverted to the inlet or outlet stream earlier in the system and returns to the last cells.

XINTC using COMSOL Multiphysics and a model of an equivalent electrical circuit in Python. The second part predicts the effect of geometrical changes on this existing design. To help this process, the main research question and subquestions are formulated as follows:

Can a three-dimensional model of an electrolyser help to predict leakage currents?

Some subquestions are set to define the scope of the thesis further.

1. Can a 3D electrolyser be accurately modelled in COMSOL Multiphysics?
2. Can a 3D electrolyser be accurately modelled using an equivalent electrical circuit (EEC) model?
3. What is the influence of design choices on the leakage currents?

1.4.1. Thesis Approach

In chapter 2, background information will be given on the basic principles of alkaline water electrolysis and its thermodynamics and electrochemistry. This is then used to dive further into existing knowledge about various forms of cell losses and leakage currents. This chapter ends with information about electrical circuits, which are needed to build the EEC model using Python. The methods to perform experiments and to create both models are described in chapter 3. In this chapter, it is also stated which assumptions are made to develop the models. After comes chapter 4 with the found results and discussion points. The models are compared to the experiments in 2D and 3D, and the resulting parameters are used to predict the performance of the electrolysis stack for various scenarios. Lastly, conclusions and recommendations are presented in chapter 5.

1.4.2. Software Used

In this thesis, three different software are used. Below is an overview of the version of the software and what it is used for.

COMSOL Multiphysics v6.2

COMSOL is a finite element software capable of combining various 3D multiphysics models. All relevant input parameters and constraints can be entered, after which a mesh is built. The

software can then calculate the required output for all mesh nodes and show this in tables and plots. Version 6.1 could also be used, but no earlier versions since those did not contain the right modules yet.

Python v3.11
Python is a programming language specifically tailored to data analysis and scientific purposes. It can import libraries to help with mathematical and statistical computations, which is favourable for iterative processes and calculations with large sets of equations. This work uses the PySpice module v1.5 to make an electrical circuit analysis. The electrical circuit can be entered manually, after which corresponding resistances, currents and voltages for each node can be simulated.

Microsoft Excel 2023
This software is mainly used to perform simple calculations and order and plot data from other software.

1.5. XINTC

This research is done in collaboration with XINTC B.V. This Dutch company produces highly modular alkaline water electrolysers for the global middle market. The modular production ranges from 150kW to 100MW. Due to its modular nature, it can quickly scale up or down when connected to an intermittent power source. The system consists of a large number of gas modules that can be turned on or off separately, as presented in figure 1.2.

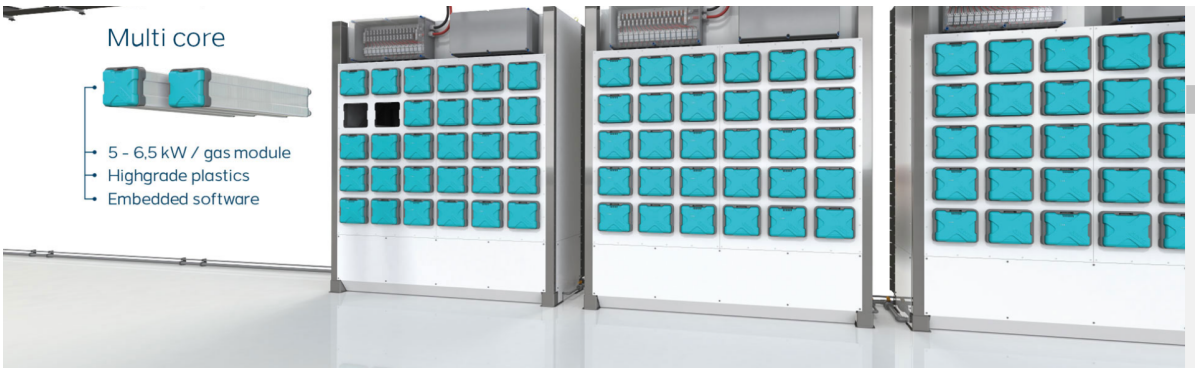

Figure 1.2: XINTC modular system. Modules (left) can be turned on or off per pair to adapt to the power source, resulting in a large modular system (right).

These electrolysers are used for manufacturing, mobility sectors, and the production of bulk chemicals. The electrolyser operates at atmospheric pressure and low temperature (around 45°C). The system, including the Balance of Plant (BoP), power electronics, and water pretreatment, is built in a container, as shown in figure 1.3, to keep the installation and transportation costs low [23].

Figure 1.3: XINTC Total product of the service station (left) and production station with modules (right).

2

Theoretical background

Hydrogen is an energy carrier, which can be considered green if the energy source is green. Renewable energy sources are then utilised to power the splitting of water into hydrogen and oxygen gas. This chapter discusses the background of water electrolysis and the related thermodynamics and electrochemistry. Furthermore, the resulting cell losses and their sources are explained.

2.1. Alkaline Water Electrolysis

The process of splitting water (H_2O) into hydrogen (H_2) and oxygen (O_2) is called electrolysis. In short, electrolysis is performed by applying a direct current through water to split water into hydrogen and oxygen gas. This current flows between two electrodes, from the anode to the cathode, separated by some separator, such as a membrane. This whole setup is immersed in an electrolyte to increase the ionic conductivity. Since the system can have very different properties, the electrodes must be resistant to corrosion and have good electric conductivity. The electrolyte should be a stable, unreactive compound with the electrodes [14].

The separator should at least prevent the produced hydrogen and oxygen gas from mixing. Furthermore, the electrical resistance must be such that it prevents the electrodes from short-circuiting. The overall reaction is shown in equation 2.1, but the half-reactions differ for different types of electrolysers. In every type of electrolyser, the oxidation reaction, in which electrons are released, occurs at the anode. Then, the electrons are used in the reduction reaction, which takes place at the cathode. The hydrogen is formed at the cathode, and oxygen is formed at the anode [14].

$$H_2O \rightarrow H_2 + \frac{1}{2}O_2 \tag{2.1}$$

For water electrolysis, there are three main options: Alkaline water electrolysis (AWE), proton-exchange membrane electrolyser (same as polymer electrolyte membrane electrolyser, PEME), and solid-oxide electrolyser (SOE) [6]. In short, the required reactions differ, and the electrically charged compound that transfers the diaphragm differs per method. Furthermore, AWE and PEME operate at low temperatures, 40-90 °C, while SOE requires a higher temperature, 500-900 °C [24–26]. These three options are shown in figure 2.1. This thesis focuses on alkaline water electrolysis since this is the most mature and widely used technique.

The electrodes in the alkaline electrolyser are from non-noble materials, for example, nickel, because of its stability, with an electrocatalytic coating. The electrodes are ordinarily a perforated sheet or expanded mesh [6, 21, 27]. AWE uses concentrated liquid lye as an electrolyte; usually a corrosive 25-35% KOH-solution [25]. Sometimes, a 20-30% NaOH

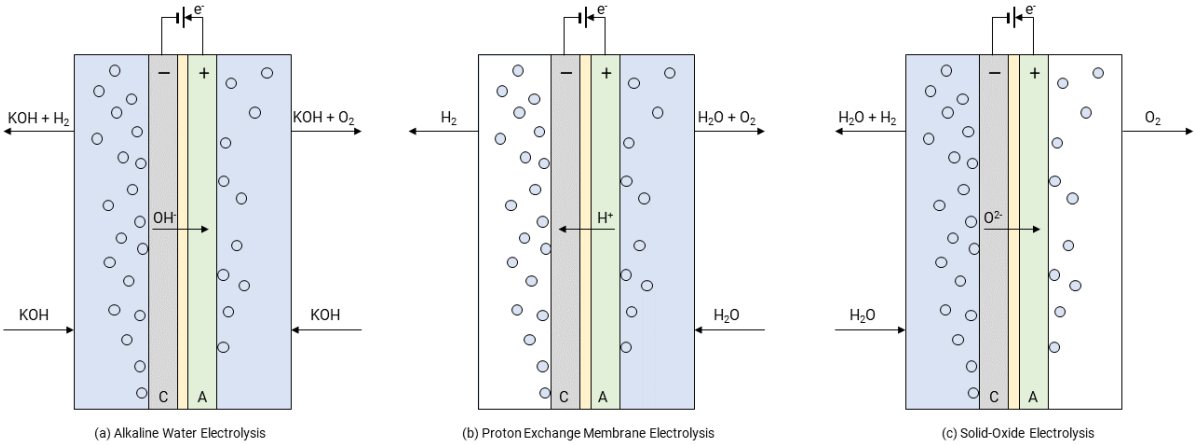

Figure 2.1: Schematic diagrams of various types of electrolysers. The current is applied across the separator (yellow) to produce hydrogen at the cathode (grey) and oxygen at the anode (green). The bulk gases are not able to pass the separator. (a) Alkaline Water electrolyser with a diaphragm between the electrodes. (b) Proton Exchange Membrane Electrolyser with a membrane between electrodes. (c) Solid-Oxide Electrolysis with ionic conducting electrolyte between electrodes [14].

solution can also be used [28]. This solution helps to maximise ionic conductivity and is circulated to remove gas bubbles and retain concentration homogeneity. A heat pump or natural circulation performs the circulation due to temperature gradients, which makes the solution concentration more homogeneous and increases the heat transfer rate [14, 24].

Equations 2.2 and 2.3 show the partial reactions in the alkaline electrolyser [14, 24]. In the cathode, the water is split into hydrogen and hydroxide ions (OH^-). The hydrogen flows out of the cell with the remaining electrolyte, and the hydroxide ions permeate through the membrane or diaphragm to the anode side. The production of hydrogen is called the Hydrogen Evolution Reaction (HER). At the anode, the hydroxide ions are used to produce oxygen gas and water, called the Oxygen Evolution Reaction (OER).

$$2H_2O + 2e^- \rightarrow H_2 + 2OH^- \quad \text{(cathode)} \tag{2.2}$$

$$2OH^- \rightarrow \frac{1}{2}O_2 + H_2O + 2e^- \quad \text{(anode)} \tag{2.3}$$

A gas-impermeable separator must be used to prevent the hydrogen and oxygen gas from mixing but allow the ions to migrate through, for which a membrane or diaphragm is used. Another function of the diaphragm is to have enough resistance to prevent the cell from short-circuiting. In earlier times, asbestos was used, but nowadays, composite materials or microporous materials such as Zirconium Oxide (Zirfon) are used. There is a gap between the separator and the electrodes, with a width varying from a millimetre to various centimetres [28–30].

A typical alkaline electrolyser can have an operating pressure of up to 30 bar, and the operating temperature is around 60-90°C. The current density is low, around 100-400mA/cm^2 [22, 28]. An alkaline water electrolyser is the most reliable type of electrolysis due to its long durability and lifetime [31, 32]. The lifetime of AWE is higher than PEME systems, while the maintenance costs are lower [6, 24]. A limitation is the large effect of the dynamic operation on efficiency, gas purity and durability. Furthermore, conventional AWE has a slow start-up of around 1-2 hours compared to the 5-15 minutes of PEME systems, making it hard to use in combination with renewable forms of energy from intermittent sources. They require a minimum base load to operate since the operation will otherwise lead to more gas crossover

[24, 28]. The total nominal stack efficiency is around 70% and reaches up to 82% [19, 31]. The achieved purity is in the range of 99.5-99.9%.

2.1.1. Electrolyser Design

Apart from the difference in chemical reactions and materials described above, the design of the electrolyser can also differ. The first option is a monopolar design, where every electrode is either negative or positive. If the electrodes are connected in parallel, the total voltage is the same as the voltage of one cell, and it can use high currents. The system allows for higher voltages when the electrodes are connected in series. In the case of the bipolar cell, the positive and negative electrodes are fixed together. In this design, the electrodes are automatically connected in series, so this is not possible in parallel. The oxidation and reduction reactions happen simultaneously on different sides of the electrode. This is all illustrated in figure 2.2 [33, 34].

If the total number of cells per stack is kept constant, then the power for the whole stack will be the same for the monopolar configuration in parallel and series, as illustrated by equation 2.4.

$$P_{stack} = I_{cell} \cdot V_{cell} \cdot N_{cell} \tag{2.4}$$

For the configuration in series, the stack voltage V_{stack} will increase linearly with the number of cells while the current stays constant. For the configuration in parallel, the current I_{stack} will increase linearly with the number of cells while the cell voltage remains the same. Therefore, both configurations result in the same stack power.

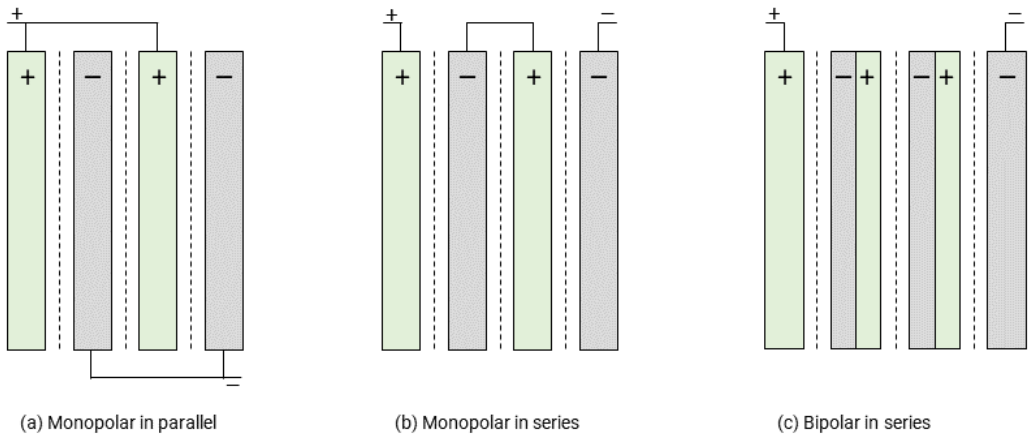

Figure 2.2: Possible cell designs for alkaline electrolyser stacks. (a) Monopolar electrode connections because every electrode is either positive or negative. (b) Monopolar electrode connections in series. (c) Bipolar electrode connections in series, where the electrodes have a different charge per side, adapted from [33].

2.1.2. Electrolysis Process

The total electrolysis system does not only comprise the cell described above. Firstly, after the hydrogen and oxygen gas are produced in the cells, these move on to the hydrogen and oxygen separator tanks, where the remaining liquid electrolyte is separated from the gas bubbles. The gases undergo more purification steps to increase the purity and drying of both gases. The remaining electrolyte is then pumped back into the electrolysis cells to be reused. Before it goes into the cells, it is cooled back to the inlet temperature. Since the voltage used is generally higher than the thermoneutral voltage, the electrolyte is heated inside the cells. As a result of the reactions shown in equations 2.2 and 2.3, the cathode side consumes water while the anode side produces water. Therefore, the electrolyte from the anode (anolyte)

and cathode (catholyte) are also mixed before re-entering the cell to prevent concentration differences.

2.2. Thermodynamics

The energy balance must be known to understand what takes place in the electrolysis cell. The overall reaction of splitting water into hydrogen and oxygen is:

$$H_2O \rightarrow H_2 + \frac{1}{2}O_2 \tag{2.5}$$

This can be used to calculate the required cell voltage, which depends on thermodynamics, specifically the Gibbs free energy, ΔG. This Gibbs free energy can be used to know more about the thermodynamics of the reaction. If it is positive, then the reaction will not occur spontaneously. If it is negative, the reaction could happen spontaneously, so the Gibbs free energy is the minimum energy for the reaction to start. For standard conditions, a temperature of 25 °C, a pressure of 1 bar, the required Gibbs free energy is as in equation 2.6,

$$\Delta G = \Delta H - T \cdot \Delta S \tag{2.6}$$

where the standard enthalpy of formation ΔH of 286.0 kJ mol^{-1}, and the standard ideal gas entropy ΔS is 0.163 kJ mol^{-1}. Therefore, the corresponding Gibbs free energy of this reaction is +237 kJ/mol. Equation 2.7 is used to convert this free energy to the required voltage.

$$V_{rev} = -\frac{\Delta G}{z \cdot F} \tag{2.7}$$

Using this Gibbs free energy, the reversible cell voltage V_{rev} can be calculated with the Faraday constant F (96,485 C mol^{-1}) and the number of exchanged electrons z, which in this case is 2. For standard conditions, a temperature of 25 °C and pressure of 1 bar, V_{rev} can be calculated to be 1.23V [35]. This cell voltage is the same as the cell potential E°, as in equation 2.8.

$$E^\circ = E^\circ_{an} - E^\circ_{cath} = (-0.40) - (0.83) = -1.23V \tag{2.8}$$

$$\begin{aligned} \Delta G &= -zFE^\circ \\ &= -2 \cdot 96485 \cdot -1.23 \\ &= 237.4\text{kJ mol}^{-1} \end{aligned} \tag{2.9}$$

The reversible voltage is as shown in equation 2.8. This voltage is defined for a reversible reaction in the absence of cell current [22], so the minimum voltage is required. Using this in equation 2.9, the Gibbs free energy can be calculated for a reversible reaction. The Gibbs free energy is positive at this voltage, so this is a non-spontaneous reaction and will need an external energy source. Using a standard temperature of 25 °C and the found value for the Gibbs free energy, the standard enthalpy of formation can be calculated.

To calculate the reversible cell potential for various temperatures, the following relation is used [36]:

$$V_{rev} = 1.50342 - 9.956 \cdot 10^{-4} \cdot T + 2.5 \cdot 10^{-7} \cdot T^2 \tag{2.10}$$

Various other relations can be used to calculate the reversible potential; however, these are mainly designed for PEM electrolysers. Still, for the temperature range used in alkaline water electrolysis, these give very similar results [37].

The enthalpy of the reaction is higher than the Gibbs free energy, so more external energy

is needed to drive the reaction, which results in a higher required cell voltage. With this enthalpy, the required cell potential for a thermo-neutral reaction can be calculated in equation 2.11.

$$V_{tn} = -\frac{\Delta H}{z \cdot F} \tag{2.11}$$

For standard conditions, ΔH = 285.8 kJ mol^{-1} is used and V_{tn} = -1.48V is found [25, 38]. If the cell potential is smaller than V_{rev}, electrolysis can not occur, and hydrogen generation is impossible. If the cell potential V_{cell} is lower than the thermoneutral voltage V_{tn}, but larger than V_{rev} then heat loss occurs, which is shown in the endothermic region in figure 2.3 [22]. If the cell potential is higher than V_{tn}, then heat is generated, and no external heat is required. The thermoneutral voltage increases due to vapour formation, while the reversible voltage decreases due to the reduction of the activation energy.

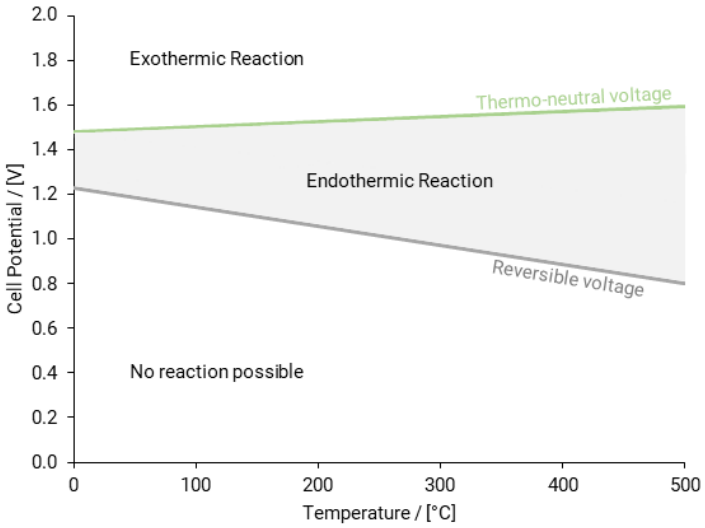

Figure 2.3: Cell potential for hydrogen production by water electrolysis as a function of temperature for a 35wt% KOH-solution at ambient pressure. For the lowest region, no reaction is possible. In the endothermic region, the reaction is possible but will need an external heat source. In the exothermic region, there will be a production of heat and cooling is required. Adapted from [22].

The amount of produced heat is linear with the current and the voltage difference as shown in equation 2.12. Part of this heat is lost via heat radiation via neighbouring electrolysis cells, as in equation 2.13 [25].

$$Q_{gen} = N \cdot I \cdot (V_{cell} - V_{tn}) \tag{2.12}$$

$$Q_{excess} = Q_{gen} - Q_{loss} \tag{2.13}$$

The reversible cell voltage is not only dependent on temperature but also pressure and molarity, as can be found using the Nernst equation [39],

$$V_{T,P}^{rev} = V_{T,P_0}^{rev} + \frac{RT}{zF} \cdot \ln\left[\frac{(P - P_w)^{1.5} \cdot P_w^*}{P_w}\right] \tag{2.14}$$

where V_{T,P_0}^{rev} is the reversible cell voltage at a temperature T and atmospheric pressure, P is the system pressure, P_w is the partial pressure of the electrolyte (KOH), and P_w^* is the partial pressure of the pure water vapour. This equation needs some changes due to the non-ideality of the produced hydrogen and oxygen gases, which is done by turning it into a virial equation of state with a second- and third-order coefficient [36, 40].

2.3. Electrochemistry

In this part, the electrochemical relations for the redox reaction are discussed. In general, electrons are transferred from the reducing species to the oxidised species:

$$\text{red} \Leftrightarrow \text{ox} + z \cdot e^{-} \tag{2.15}$$

The electrochemical reactions at the electrodes are caused by the applied voltage to the electrolyser. Earlier, the applied voltage was discussed, but the rate of reaction is also dependent on several conditions, such as the pre-treatment of the electrodes, composition and concentration of the electrolyte at the electrode and the overpotentials [36]. The Gibbs free energy of the redox reaction is proportional to the activation overpotential at the electrode.

$$\begin{aligned} \Delta G_c &= \Delta G_c^{eq} + \alpha_c z F \eta \\ \Delta G_a &= \Delta G_a^{eq} - \alpha_a z F \eta \end{aligned} \tag{2.16}$$

in which α_a and α_c are the anodic and cathodic transfer coefficients, respectively. The transfer coefficient defines the level of symmetry of the energy barrier, which, in turn, determines the direction of the reaction. If the intermediate transition state of the reaction is more like the original reactant, then α becomes closer to 0, but if it is more like the product, then α becomes closer to 1. For the hydrogen electrolysis reaction, it is often between 0.3 and 0.7 and set at 0.5 if unknown. Using the Gibbs free energy corrected for the overpotential in equation 2.16, the rate of the reduction K_{red} and oxidation reaction K_{ox} can be calculated by the Arrhenius equation, and expressed as a function of the Gibbs free energy change:

$$\begin{aligned} K_{red} &= f_{red} \exp\left[\frac{\Delta G_a}{RT}\right] \\ &= f_{red} \exp\left[\frac{\Delta G_a^{eq}}{RT}\right] \exp\left[\frac{\alpha_a z F \eta}{RT}\right] \end{aligned} \tag{2.17}$$

$$\begin{aligned} K_{ox} &= f_{ox} \exp\left[\frac{\Delta G_c}{RT}\right] \\ &= f_{ox} \exp\left[\frac{\Delta G_c^{eq}}{RT}\right] \exp\left[\frac{-\alpha_c z F \eta}{RT}\right] \end{aligned} \tag{2.18}$$

where η is the activation overpotential, $f_{red/ox}$ is the frequency factor, and $\alpha_{a/c}$ is the charge coefficient or transfer-charge factor for a multi-electron reaction. The net cell current is described as

$$i = i_a - i_c \tag{2.19}$$

where the partial current of the anode or cathode is proportional to the constant rate of the reaction at that electrode, the local concentration and the electrode surface. Combining equations 2.17, 2.18, and 2.19 results in the Butler-Volmer equation for each electrode [41]:

$$i_{A/C} = F k^0 \left(A_{red} C_{red} \exp\left[\frac{\alpha_{red} z F \eta}{RT}\right] - A_{ox} C_{ox} \exp\left[\frac{-\alpha_{ox} z F \eta}{RT}\right] \right) \tag{2.20}$$

where $A_{red/ox}$ is the electrode surface area, k^0 is the standard rate constant, and $C_{red/ox}$ is the concentration of the reaction species at the electrode. This current is determined for both the anode and the cathode. At the anode, the overpotential is positive and often the second exponential term can be neglected. The overpotential is negative, and then the first

exponential term can be neglected compared to the second. Therefore, the overall Butler-Volmer is often described as:

$$i = Fk^0 \left(A_a C_a \exp\left[\frac{\alpha_a z F \eta}{RT}\right] - A_c C_c \exp\left[\frac{-\alpha_c z F \eta}{RT}\right] \right) \tag{2.21}$$

For a larger k^0, the equilibrium of the reaction is reached faster, while for a small k^0, this takes more time. Suppose the potential is increased by η. In that case, the relative energy of the electrons will decrease by $zF\eta$, which results in a reduction of the Gibbs free energy at the cathode by $zF\alpha_a\eta$ and an increase of the Gibbs free energy at the anode by $zF\alpha_c\eta$. The exchange current i_0 is the current for which $A_a C_a$ in equation 2.21 is equal to $A_c C_c$. Inserting i_0 into the Butler-Volmer equation gives:

$$i = i_0 \left(\exp\left[\frac{\alpha_a z F \eta}{RT}\right] - \exp\left[\frac{-\alpha_c z F \eta}{RT}\right] \right) \tag{2.22}$$

This is valid if it is assumed that the electrolyte concentration is the same at the electrode surface and in the bulk. If the overpotential η is very small, the net current has a linear relation with the overpotential, which further simplifies the Butler-Volmer relation to:

$$i = \frac{j_0 A_{a/c} z F (\alpha_c + \alpha_a)}{RT} \cdot \eta \tag{2.23}$$

where j_0 is the current density corresponding to $i_0/A_{a/c}$. If the magnitude of overpotential $\eta \geq [RT/zF(\alpha_a + \alpha_c))] \cdot [4.605 + \ln(A_{ox}/A_{red})]$, then one of the exponential terms of the overpotential becomes less than 1% of the other exponential term and becomes negligible. Equation 2.23 is then simplified, and the Tafel equation can be used as an approximation [36, 41]:

$$\eta_{a/c} = \frac{RT}{zF\alpha_{a/c}} \cdot \ln\left[\frac{i}{i_{0,a/c}}\right] \tag{2.24}$$

2.4. Cell Losses

The electrolysis reaction does not yield a 100% efficiency due to cell losses. These can be caused by various processes, which will be described below. Due to these losses, the actual cell potential must be higher than the reversible one.

2.4.1. Stack Efficiency

The most accepted way to calculate the cell efficiency is by taking the product of the Faraday efficiency and the voltaic efficiency [38].

$$\eta_{cell} = \eta_F \cdot \eta_{volt} \tag{2.25}$$

The Faraday efficiency is a mass conservation efficiency. The higher the temperature in the electrolysis process, the lower the Faraday efficiency because the electrolyte resistance decreases for higher temperatures. This leads to higher crossover currents. The same principle applies to pressure, so the higher the pressure, the lower the efficiency. The Faraday efficiency is used to determine the losses via leakage currents and is calculated as follows [42]:

$$\eta_F = \frac{i\Delta t/2F - \Delta N_{H_2 loss}}{i\Delta t/2F} = \frac{i - 2F\dot{n}_{H_2 loss}}{i} = \frac{i - i_{loss}}{i} \tag{2.26}$$

where $\dot{n}_{H_2 loss} = \Delta N_{H_2 loss}/\Delta t$. The voltaic efficiency is an energy efficiency and is calculated as in the following equation [24, 38, 42]:

$$\eta_{\text{volt}} = \frac{\Delta H_{rev}}{\Delta H_{rev} + zF\eta_{loss}} = \frac{\Delta G_{rev} + \Delta Q_{rev}}{zFV_{cell} + \Delta Q_{rev}} = \frac{V_{tn}}{V_{tn} + V_{cell} - V_{rev}} \tag{2.27}$$

where $\eta_{loss} = V_{cell} - V_{rev}$. The voltaic efficiency is 100% for a reversible cell potential. The real cell voltage can also be determined differently. In this case, it is the sum of the reversible voltage and all overpotentials; activation overvoltages (V_{cat}, V_{an}), ohmic overpotentials (V_{ohm}), and concentration overpotentials (V_{conc}) [14, 25, 37]:

$$V_{cell} = V_{rev} + V_{act} + V_{ohm} + V_{con} \tag{2.28}$$

According to David et al. [27], the greatest loss of efficiency in an electrolyser, in order of priority, is as follows:

1. Hydrogen bubble phenomena on the surface of electrodes
2. Ionic resistance of the electrolyte
3. Presence of oxygen bubbles
4. Resistance of diaphragm

2.4.2. Ohmic Overvoltage

In equation 2.28, ohmic overvoltage V_{ohm} is mainly caused by the resistance of cell elements to the electron flow, such as a bubble layer on the electrodes and current collectors (R_{anode} and $R_{cathode}$). It can also be due to the ion flow being in the opposite direction to electrolyte flow (R_{ions}) or gas bubbles ($R_{bubbles,O2/H2}$). Therefore, the losses due to the flow are proportional to the gap distance and the distance. In current electrolysers, a minimal gap or zero-gap is used to reduce this because it was shown that the voltage decreased as the gap size decreased. However, for larger current densities but within the range of an alkaline electrolyser, there is an optimum space of around 1-2mm because the voltage increases when the gap becomes very small. This is due to bubbles taking up a large space of the little electrolyte volume, which increases the resistance again [21, 43]. All ohmic resistances can be added in series [44]:

$$\sum R_i = R_{circuit} + R_{anode} + R_{bubble,O2} + R_{membrane} + R_{ions} + R_{bubble,H2} + R_{cathode} \tag{2.29}$$

The resistance of the membrane ($R_{membrane}$) or diaphragm is determined by the material and the thickness. For a zero-gap cell, the diaphragm becomes more important. The ohmic losses due to the diaphragm are proportional to the thickness of the membrane.
The resistance can be calculated using two methods, in which the first is Ohm's law and the second is to calculate the resistance of the circuit:

$$R = \frac{V}{I} \tag{2.30}$$

$$R = \frac{l}{\kappa A} \tag{2.31}$$

in which l is the length of the wires, κ is the specific electrical conductivity, and A is the cross-sectional area of the wires.

2.4.3. Activation Voltage Electrodes

The activation overvoltage results from electrode kinetics, which is the loss when energy is transferred between the charge of the electrode and the chemical species. This highly depends on the catalytic properties of the electrode, as discussed before. The overpotential of the cathode is generally higher than the overpotential of the anode, and together, they are non-linear with the electric current because the relation is logarithmic [22]. The overpotentials can be calculated using equation 2.24.

2.4.4. Concentration Overvoltage

The last overvoltage is caused by concentration differences in the cell due to mass transport processes. For high current densities, the electrode reaction rate becomes so high that the diffusion of substrates and products is the limiting reaction rate. This leads to a concentration gradient between the electrolyte at the electrode and the bulk of the electrolyte. However, this phenomenon only occurs for higher current densities, while alkaline electrolysers use lower current densities. Therefore, this concentration overvoltage V_{con} is much smaller than the other overvoltages above [14, 37]. This can thus often be neglected for low current densities.

2.4.5. I-V Curve

The reversible and thermoneutral cell voltages depend on the cell's current density, which can be visualised in a polarisation curve, also known as an I-V curve. This curve is needed because it shows the energy demand needed for hydrogen production. This curve varies for different temperatures because both the reversible and the thermoneutral cell voltage decrease for higher temperatures. This is logical, considering the increased energy input from heat. This curve is almost independent of pressure. The required voltage very slightly increases for higher pressures, while the excess heat decreases [25].

The I-V curve is affected by different components, as described before, shown in figure 2.4 [39]. This shows that the increase in cell voltage for higher current densities mainly originates from the linear increase in ohmic loss in the electrolyte [22, 45, 46].

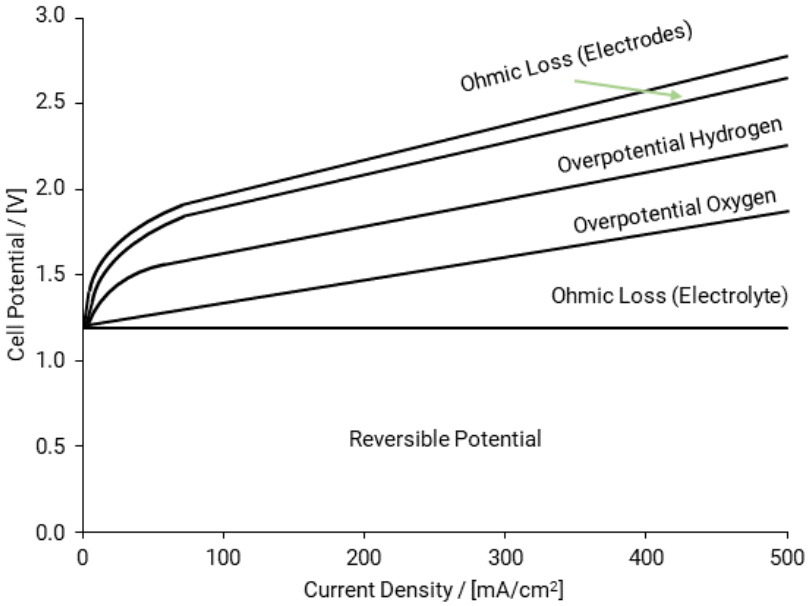

Figure 2.4: Characteristic I-V curve of a typical electrolysis cell. The several elements contributing to the total cell potential are shown. This is an example, and the total cell potential will vary depending on parameters such as pressure, temperature and electrolyte concentration.

2.4.6. Bubble Effect

During the electrolysis, gas bubbles of hydrogen and oxygen form on the electrodes, which reduces the reaction area of the electrodes and blocks the transfer of electrons from the electrode to the electrolyte. The bubbles grow in size and are released into the electrolyte when they have reached a critical size. Due to the reduced area of the electrodes, the local current density increases. As the current density increases, the gas formation also increases, resulting in a larger bubble effect and more losses [36, 47]. These losses can lead to a high

overpotential and are part of the ohmic losses as described before because they block the ion flow from and to the electrode [22]. Usually, the reaction overpotential can be described using the Tafel equation, as in equation 2.32. To correct for the reduced area due to bubble formation, equation 2.34 is used [7]:

$$\eta = a + b \log i \tag{2.32}$$

To calculate the real overpotential η_θ, a current density j_θ correcting for the bubble coverage is used:

$$j_\theta = \frac{i}{A(1-\theta)} \tag{2.33}$$

which gives

$$\begin{aligned} \eta_\theta &= a + b \log \frac{i}{A(1-\theta)} \\ &= a + b \log \frac{i}{A} + b \log \frac{1}{(1-\theta)} \\ &= \eta + b \log \left(\frac{1}{1-\theta} \right) \end{aligned} \tag{2.34}$$

where θ is the bubble coverage ratio on the electrode surface and has a value between 0 and 1. To reduce the bubble effect, mechanical circulation can be introduced so the bubbles are released faster. Another option is to use additives to alter the electrolyte's surface tension, but of course, this might have side effects on the reaction chemistry [22]. Furthermore, it is thought that for increasing electrolyte flow, the bubble formation decreases [48].

2.5. Leakage Currents

One of the first papers that showed modelling of leakage currents used an electrical network for a bipolar cell stack [49–51]. Using Kirchoff's laws, it was found that the leakage current is higher for the cells at the beginning and end of the stack. The difference between the applied current and cell current builds up and is, therefore, highest in the middle of the stack [20, 49]. Using this resistance network to get a set of linear equations, it was found that the leakage current is larger for an increasing number of cells in the stack [52]. This leakage current was largely affected by internal resistances in the direction of the battery current.

The leakage current for an increasing number of cells does not increase linearly. If the number of cells increases, the average leakage current per cell decreases. Comninellis et al. [53] showed that this non-linear relation is mainly present at low current densities. For higher current densities, the curve does become almost linear, but the slope of the curve is flatter than for lower current densities. If this model is scaled up, the leakage currents become lower for high current densities and longer electrodes [20, 54].

If the bubble coverage and resistance due to bubbles are considered, the leakage current as a function of current density is an almost linear relation. The current efficiency increases to an asymptotic value for higher current densities [55]. Lastly, the voltage does not directly affect the leakage current [56].

2.5.1. Protective Currents

As described in various patents ([57–59]), it might be beneficial to add a protective current to the electrolysis system. This current is applied through the manifolds and reduces the potential difference between the active area of the cell and the manifold, reducing the loss of current through the manifold. It has not yet been described if this method results in a higher efficiency since the energy for the extra current must also be taken into account.

2.6. Electrical Circuits

An electrical circuit is a network of electrical elements. An electrical element can be, for instance, a resistance, voltage source, or current source. It is a closed loop, meaning all current stays within the network. There are a few basic laws for electrical circuits [60]; Kirchoff's current law states that all currents leaving a node must equal all currents entering that same node. Kirchoff's voltage law states the sum of all potential differences around a loop must be zero. Lastly, Ohm's law states that the voltage through a resistor is equal to the product of the current and resistance at that point, also known as $V = I \cdot R$.

A current will follow a path of least resistance if multiple routes are possible in a circuit. When there are multiple resistances in parallel, a current will divide itself between the resistances depending on the magnitude of the resistance. The higher the resistance, the less current will go through, assuming the voltage stays constant.

2.7. Flow Patterns and Pressure Drop

While modelling the stack, it could be interesting to research the pressure drop over the system. Several aspects need to be taken into account to calculate this pressure drop. Firstly, the flow is incompressible, so the density does not change with time. Also, the flow is considered diphasic with a liquid and gas flow. The momentum equation at the integral scale is as follows:

$$\frac{d}{dt}\iiint_{CV} \rho \underline{u}\, dV = -\oiint_{CS} \rho \underline{u} \cdot \underline{u}\hat{n}\, ds + \iiint_{CV} \underline{f}\, dV + \oiint_{CS} \underline{t}\, ds \tag{2.35}$$

where $\underline{u}$ is a flow velocity vector. The total momentum in the control volume (left of the equation) consists of the total flux of momentum through the control surface, the surface forces on the control surface, and the body forces in the control volume. The momentum equation in vector equation is as follows:

$$\rho\left(\frac{\partial \underline{u}}{\partial t} + \underline{u} \cdot \underline{\nabla u}\right) = -\underline{\nabla} p + \mu \underline{\nabla}^2 \underline{u} + \underline{f} \tag{2.36}$$

Then, some assumptions need to be made to use the momentum equation in 3D. In this case, ideal flow is considered, which means that the flow is both irrotational and incompressible.

1. The flow is irrotational, so the vorticity is 0: $\underline{\omega} \cdot (\underline{\nabla} \times \underline{u}) = 0$;
2. If $\underline{\nabla} \times \underline{u} = 0$, then $\underline{u} = \underline{\nabla}\Phi$;
3. The flow is incompressible, so $\underline{\nabla} \cdot \underline{u} = 0$. Considering the irrotational argument, this means that $\underline{\nabla} \times (\underline{\nabla}\Phi) = 0 \rightarrow \underline{\nabla}^2\Phi = 0$;
4. For an ideal flow $\underline{\omega} = \underline{\nabla} \times \underline{u}$, so $\underline{\nabla} \times \underline{\omega} = \underline{\nabla} \times (\underline{\nabla} \times \underline{u}) = \underline{\nabla}(\underline{\nabla} \cdot \underline{u}) - \underline{\nabla} \cdot (\underline{\nabla u})$. Using assumption 1 and 3, it is found that $-\underline{\nabla}^2 \underline{u} = 0$.

Using the steps above, the momentum equation from equation 2.36 becomes:

$$\rho\left(\frac{\partial \underline{u}}{\partial t} + \underline{u} \cdot \underline{\nabla u}\right) = -\underline{\nabla} p + \underline{f} \tag{2.37}$$

This results in the strong form of the Bernoulli equation:

$$\rho \frac{\partial \Phi}{\partial t} + P + \frac{1}{2}\rho |\underline{u}|^2 + \phi = \text{constant}(t) \tag{2.38}$$

2.7.1. Poiseuille Flow

In the case of the electrolyser, the flow is an unidirectional flow inside the cell. Since both walls are stationary, this can be seen as a Poiseuille flow. Now, the momentum equation reduces to:

$$0 = \frac{\partial p}{\partial x} + \mu \frac{\partial^2 u}{\partial y^2} \tag{2.39}$$

with the parameters as described in figure 2.5.

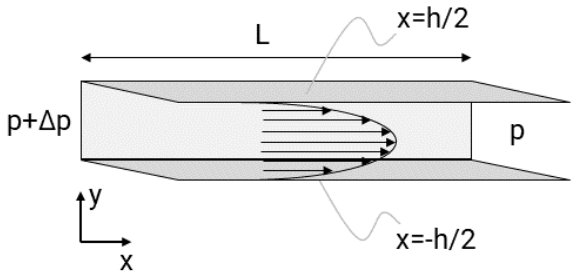

Figure 2.5: Horizontal Poiseuille flow. Pressure drop over length L in the x-direction. It is assumed that the walls are stationary and the flow is unidirectional.

Using the following steps, the flow velocity $u(x)$ can be found.

$$\begin{aligned} &\frac{p^- - p^+}{L} = \frac{\Delta P}{L} = \mu \frac{\partial^2 u}{\partial y^2} \\ &\frac{\partial^2 u}{\partial y^2} = -\frac{1}{\mu}\frac{\Delta p}{L} \xrightarrow{\int dy} \frac{\partial u}{\partial y} = -\frac{\Delta p}{\mu L} y + C_1 \xrightarrow{\int dy} u = -\frac{\Delta p}{2\mu L} y^2 + C_1 y + C_2 \end{aligned} \tag{2.40}$$

To find the values for the constants, the boundary conditions are used. The only boundary condition used is that the walls are a no-slip surface, so the flow velocity is zero at the wall.

$$\left.\begin{aligned} u(y = \frac{h}{2}) = 0 \\ u(y = -\frac{h}{2}) = 0 \end{aligned}\right\} \left.\begin{aligned} 0 = -\frac{\Delta p}{2\mu L}\frac{h^2}{4} + C_1\frac{h}{2} + C_2 \\ 0 = -\frac{\Delta p}{2\mu L}\frac{h^2}{4} - C_1\frac{h}{2} + C_2 \end{aligned}\right\} \left.\begin{aligned} 2C_2 = \frac{\Delta p}{4\mu L} \\ C_1 = 0 \end{aligned}\right\} u(y) = \frac{-\Delta p}{2\mu L}\left(y^2 - \frac{h^2}{4}\right) \tag{2.41}$$

For a single phase, laminar flow in a tube ($Re \leq 2100$), the pressure drop can be calculated using the Hagen-Poiseuille equation [61], adapted for pipes with a non-circular cross-section:

$$\frac{\Delta p}{L} = \frac{14.2}{Re}\left(\frac{1}{2}\rho U^2\right)\frac{4}{D_H} \tag{2.42}$$

in which D_H is the hydraulic diameter, an adjusted diameter for a non-circular pipe. This formula is explained further in section 2.7.4.

2.7.2. Pressure Drop in Two-Phase Flow

There are several vertical two-phase flow regime types, as shown in figure 2.6 [62]. Bubble flow is present at very low liquid and gas velocities when the liquid phase is continuous, and the gas phase is present in small bubbles. Bubble flow is split into two types, the first being bubbly flow, where the relatively larger gas bubbles move faster than the liquid phase. The second type is dispersed bubble flow, where the bubbles are smaller and have the same velocity as the liquid phase. Slug flow is characterised by coalescing bubbles, also known as Taylor bubbles. The diameter of these bubbles is almost equal to the diameter of the pipe,

creating a liquid film close to the wall. The length of the bubble can be multiple times the diameter. In between these large bubbles is liquid flow with smaller bubbles, known as liquid plugs. Overall, the velocity of the gas phase is larger than the velocity of the liquid phase [63, 64]. Churn flow arises when the liquid phase in between the Taylor bubbles is filled by gas. This process has an oscillatory nature and may turn the flow into froth. This phenomenon is usually not present in small-diameter pipes. When the gas phase becomes continuous in the centre of the pipe, while the liquid is present as a thin film at the wall, the flow is called annular flow. There may also be some tiny liquid drops dispersed into the gas phase.

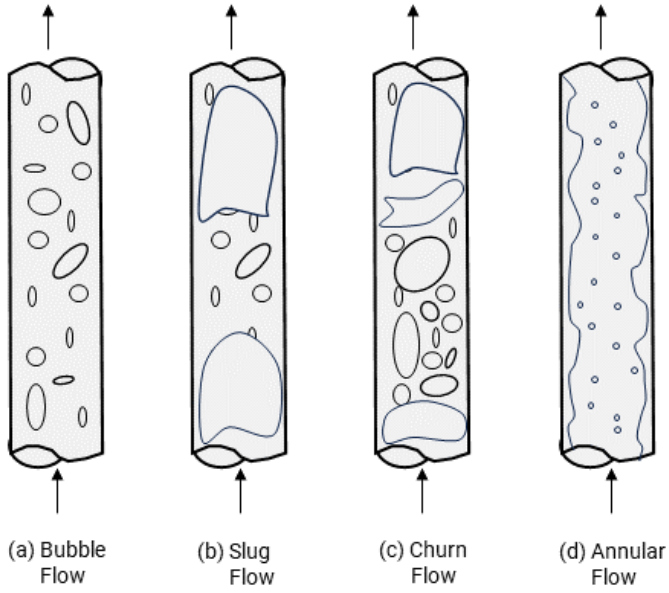

Figure 2.6: Types of vertical two-phase flow regimes, adapted from [62]. Bubble flow (a) presents as a liquid flow with gas bubbles. Slug flow (b) is still a liquid flow but with larger gas bubbles, almost equal to the diameter of the pipe. Churn flow (c) has an oscillatory nature because the space in between Taylor bubbles is filled with gas, which may turn into froth. In annular flow (d), the liquid is mostly present at the walls with a gas stream containing liquid droplets through the middle of the pipe.

The horizontal two-phase flow has different characteristics than the vertical flow, as presented in figure 2.7. Again, the bubble flow is present in a continuous liquid flow. The bubbles are more present in the upper half of the pipe due to buoyancy effects. The liquid and gas flow rate can be higher than for vertical bubble flow. For lower gas and liquid flow rates, the small bubbles coalesce to form larger pointy bubbles called plug flow. If the gravitational effects are also considered, this can cause total separation of the gas phase from the liquid phase. This is called stratified flow and can either be smooth or wavy, with the latter happening if the gas velocity increases. The liquid level becomes wavier for even higher gas and liquid flows until the wave is as high as the pipe diameter, which blocks the gas flow. This liquid part is then pushed forward by the gas flow, which causes the pipe to have large gas bubbles and high liquid levels (liquid slugs) alternate throughout the pipe. Liquid droplets can be entrapped in the gas flow, and gas droplets can be dispersed in the liquid flow. For an increasing gas flow rate, the gas phase can become present in a large part of the pipe, with the liquid present as a thin film, mostly at the bottom, due to gravity effects. The gas phase can contain dispersed liquid droplets.

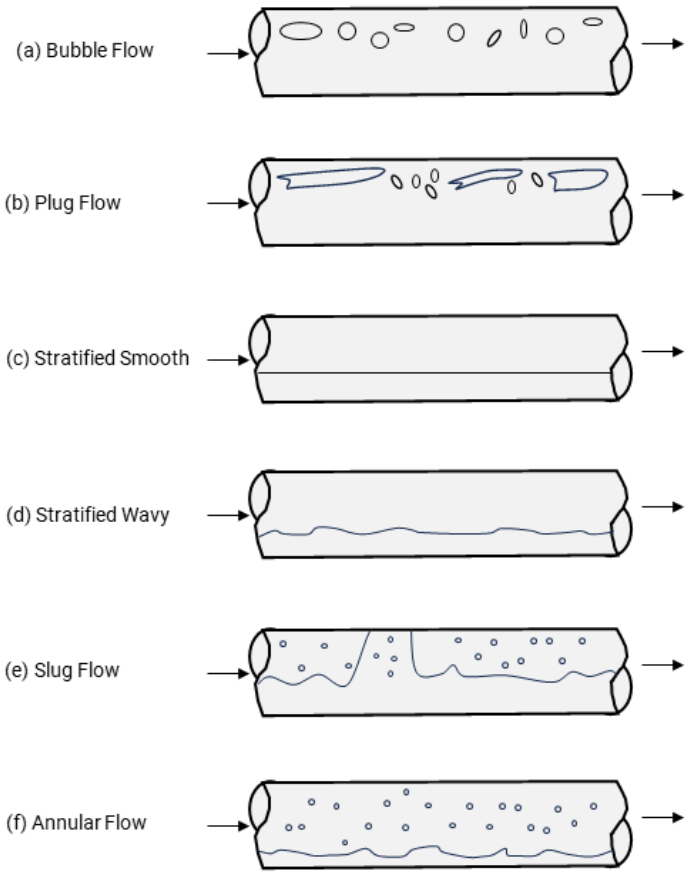

Figure 2.7: Types of horizontal two-phase flow regimes, adapted from [62]. Bubble flow (a) presents as a liquid flow with gas bubbles. Plug flow (b) is still a liquid flow but with larger bubbles. Stratified flow (c&d) happens when the liquid and gas are separated. If the gas velocity increases, the stratified flow becomes wavier. In slug flow (e), the large gas bubbles and liquid droplets alternate and are pushed forward throughout the pipe. In annular flow (f), the liquid is present at the bottom, with a gas flow containing liquid droplets at the top.

To calculate the pressure drop, firstly, some non-dimensional numbers are introduced. The Bond number is the balance between the gravitational forces and the forces due to surface tension:

$$\text{Bo} = \frac{(\rho_l - \rho_g) g d^2}{\sigma} \tag{2.43}$$

where ρ is the density of the liquid or gas, g is the gravitational constant, d is the diameter of the tube, and σ is the surface tension of the electrolyte. For a bond number smaller than 3.37, the bubbles will not rise spontaneously [65], and the diameter will usually be between 1 and 2mm. A second non-dimensional number is the Froude number, which balances the inertial and gravitational forces:

$$\text{Fr} = \frac{u_b}{\sqrt{gd}} \tag{2.44}$$

where U_b is the bubble velocity. When the Froude number is plotted against the Bond number, it is found that the bubble velocity becomes 0 for a Bond number smaller than 4. A third non-dimensional number is the capillary number, which balances the viscous forces and the surface tension:

$$\text{Ca} = \frac{\mu_l u_b}{\sigma} \tag{2.45}$$

where μ_l is the viscosity of the liquid. The bubbles are not axisymmetric and flatten out for Ca<0.1, while the bubbles are more axisymmetric or round for Ca>>0.1. The asymptotic limit of the bubble size is then up to 0.68 times the diameter of the channel.

2.7.3. Gravitational Pressure Drop

The gravitational pressure drop is not dependent on the flow velocity and is calculated as follows:

$$\Delta P = \rho g \Delta h \tag{2.46}$$

where Δh is the vertical displacement of the fluid flow in m.

2.7.4. Frictional Pressure Drop

Using Perry's Handbook for Chemical Engineers [66], the standard formulas for the friction coefficient for several flow regimes are found, with one applicable for all regimes. The pressure drop is calculated as follows:

$$\Delta P = f \frac{L}{D_H} \frac{\rho u^2}{2} \tag{2.47}$$

For circular pipes, the diameter of the pipe can be used, but for rectangle-shaped pipelines, the hydraulic diameter D_H is used, which is the ratio between the cross-sectional area and the wetted perimeter of the flow:

$$D_H = \frac{4 * \text{area}}{\text{wetted perimeter}} = 4 * \frac{ab}{2(a+b)} \tag{2.48}$$

where a is the width of the channel and b, is the height of the channel.
For laminar flow ($Re \leq 2100$), the friction factor is described by the Hagen-Poiseuille equation:

$$f = \frac{16}{Re} \quad \text{(circular)}, f = \frac{14.2}{Re} \quad \text{(non-circular)} \tag{2.49}$$

The friction coefficient f can also be calculated using a single equation for all single-phase flow regimes:

$$\begin{aligned} f &= 2 \cdot \left[\left(\frac{8}{Re} \right)^{12} + \frac{1}{(A+B)^{3/2}} \right]^{1/12} \\ A &= \left[2.457 \ln \left(\frac{1}{\left(\frac{7}{Re} \right)^{0.9} + 0.27 \frac{\epsilon}{d}} \right) \right]^{16} \\ B &= \left[\frac{37530}{Re} \right]^{16} \end{aligned} \tag{2.50}$$

The frictional loss coefficient K can be determined for different types of losses and is related to the friction factor using the following equation:

$$K = f \frac{L}{D_H} \tag{2.51}$$

Expansion and contraction losses
Losses due to direct contractions are almost negligible since the flow is pushed together, which leaves little space. The loss coefficient for direct expansion K_{exp} is:

$$K_{exp} = \left[1 - \frac{A_{in}}{A_{out}}\right]^2 \tag{2.52}$$

where A is the cross-sectional area of the pipe.

Manifold losses
Manifolds are used to split and combine flows. The inlet manifold of the electrolyser splits the flow into the different cells, while the upper manifold combines the flows. For an optimal flow distribution, the total cross-sectional area of all branches combined must be a maximum of half of the total cross-sectional area of the manifold tube [67]. As shown in figure 2.8, the pressure drops at the branches have different frictional loss coefficients.

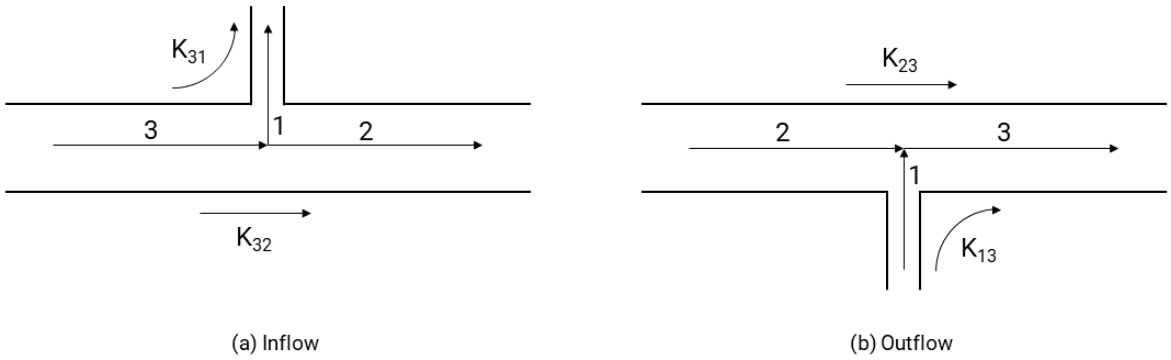

Figure 2.8: Inlet and outlet flows in branches, derived from [67].

These frictional loss coefficients K_{ij} are defined as:

$$K_{ij} = \frac{P_i - P_j}{\text{mean velocity pressure in 3}} \tag{2.53}$$

and can be found in figure 2.9, using the volumetric flow ratio Q_1/Q_3. This equation is valid for a flow ratio between 0 and 1.

Friction factor for non-circular channels
Angeli and Gavriilidis ([65]) looked into the hydrodynamics of Taylor flow in capillary channels. Elongated bubbles characterise Taylor flow with lengths equal to multiple times the diameter of the flow channel. For non-circular channels, like square channels, the friction factor can be calculated:

$$f = \frac{14.2}{Re}\left[1 + \alpha_l \frac{d}{L_s}\left(\frac{Re}{Ca}\right)^{1/3}\right] \tag{2.54}$$

where α_1 is a dimensionless fitting parameter. This equation is valid for $2 \times 10^{-3} < Ca < 4 \times 10^{-2}$ and Re of the order of 100 [61, 65]. If both the Reynolds and capillary numbers are very small ($Ca << 1$ and $Ca \times Re << 1$), the previous equation can be combined with the Bretherton equation [65]:

$$f = \frac{14.2}{Re}\left[1 + \frac{d}{L_s}\frac{0.456}{Ca^{1/3}}\right] \tag{2.55}$$

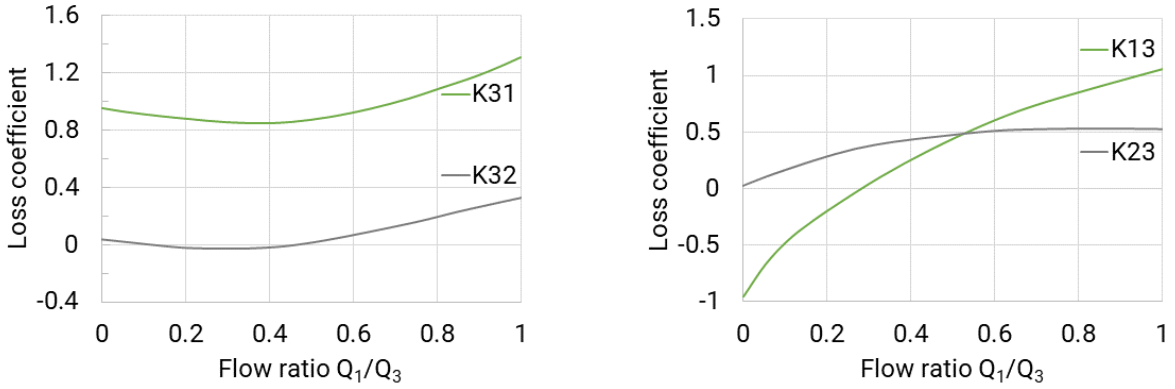

(a) Inflow (b) Outflow

Figure 2.9: Flow in dividing (a), and splitting (b) T-junctions. The loss coefficients K_{ij} depend on the volumetric flow ratio, defined as the ratio of the volumetric flow rate of the branch to that of the manifold. Derived from [67]

If the pipe is circular, then the first coefficient of 14.2 is changed into 16. The pressure drop ΔP can then be calculated using this formula:

$$\frac{\Delta P}{L} = \frac{2 f u_m^2 \rho_l}{d} \Phi_l \tag{2.56}$$

where L is the channel length, U_m is the flow velocity of the mixture, and Φ_l is the liquid phase volume fraction.

3

Methods

This chapter contains four sections, the first about the setup of experiments and the second and third about the design of two different models. Firstly, experiments are performed, which will be used to validate the models. Then, the first model is created in COMSOL Multiphysics software using the desired geometry from the experimental test cells. This model uses several modules that will be discussed in this second part. Lastly, several parameters can be changed to fit the data of the experiments to the COMSOL model, and these will be predicted using an already developed in-house model. Also, a model based on an equivalent electrical circuit of an electrolysis stack rather than multiphysics is used for validation. The fourth section is about calculating the pressure drop of the experimental setup.

3.1. Design of Experiments

Two setups were built to gather experimental data, comprising one R&D test cell, and a module consisting of eight cells of the same kind in series. The single-cell setup is needed to find the polarisation curve without leakage currents to find the single-cell losses. Afterwards, the multi-cell system was built using the same principle.

The R&D test cells used are not identical to the actual cells commercially used by XINTC but have different dimensions for two reasons: creating larger leakage currents and for the sake of confidentiality. The test cells are all connected in series, resulting in an almost constant current (aside from losses due to leakage currents) and a voltage equal to the cell voltage multiplied by the number of cells. The design of the cells is shown in figure 3.1 (2D) and figure 3.2 (3D). Hydrophobic diaphragms are used because they are considerably cheaper than hydrophilic diaphragms but have similar performance.

For both systems, the following data was measured:

- Total stack current
- Total stack voltage
- Temperature at both inlets, both outlets and separator tank
- Total stack Faraday efficiency
- Cell voltage
- Produced hydrogen per stack

The used flow meters are the Tylan FM360 and the Tylan FM380, which both have an accuracy of ±1%, while the repeatability is ±0.2% [68, 69].

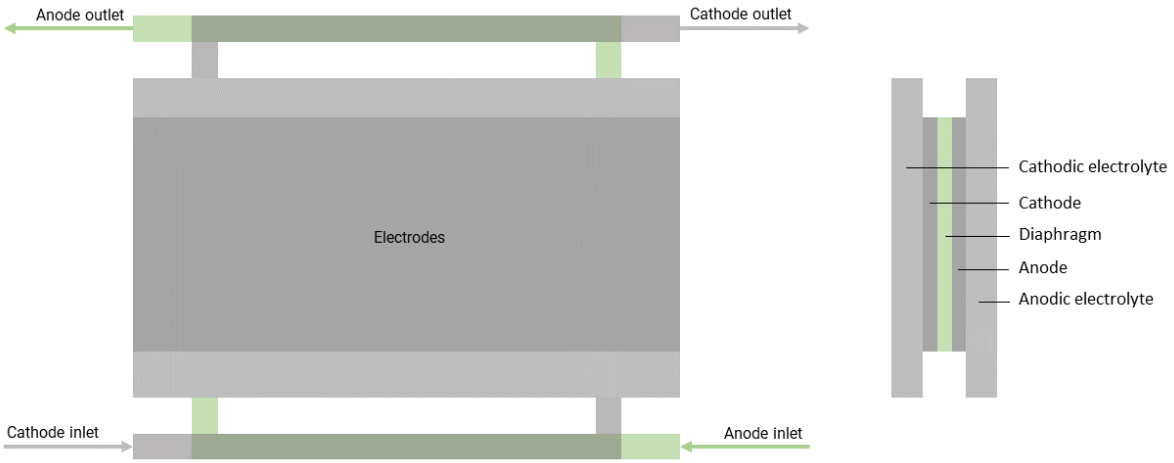

Figure 3.1: Graphical representation of a single electrolysis cell in 2D. The cell is pictured from the front (left) and the side (right). The liquid enters the cell via the inlets at the bottom and moves upwards along the electrodes towards the outlets. Bubbles are formed at the electrode via the electrolysis reactions. For these reactions to happen, hydroxide ions migrate from the cathodic side through the diaphragm to the anodic side. This figure does not scale with the actual cells.

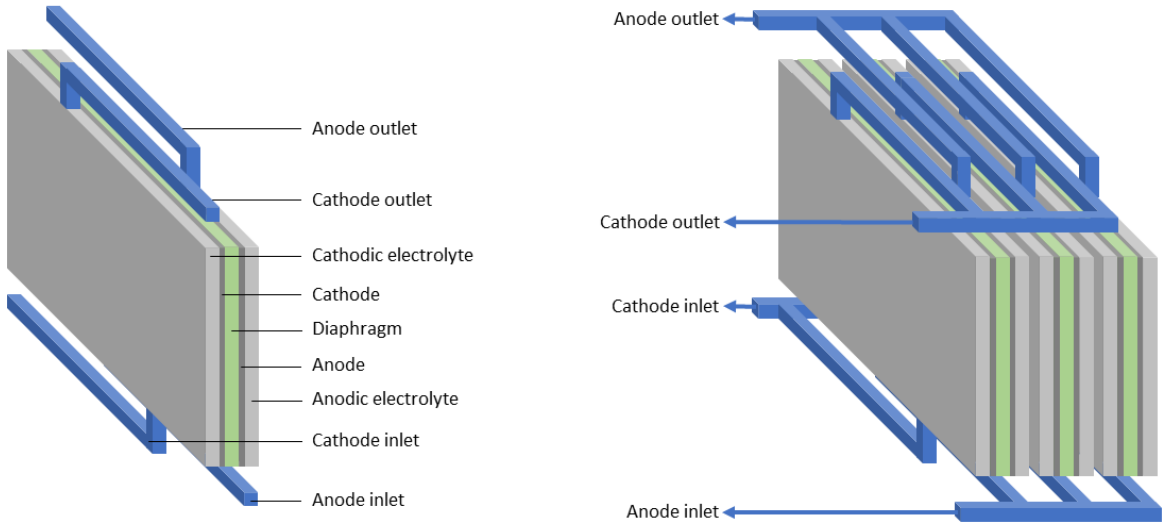

Figure 3.2: Graphical representation of a single electrolysis cell in 3D. In a multi-cell system, all inlets and outlets are connected in series via the manifold (right). The liquid enters the cell via the inlets at the bottom and moves upwards along the electrodes towards the outlets. Bubbles are formed at the electrode via the electrolysis reactions. For these reactions to happen, hydroxide ions migrate from the cathodic side through the diaphragm to the anodic side.

3.1.1. Design inlets

The inlet design is different from the outlet design. While the outlets are straight and have a similar length to the cell's width, the inlets are zigzag-shaped and narrowed. This lengthened the inlet channel by a factor of three, as shown in figure 3.3. In this thesis, two inlet designs are used. First, the long zigzag inlet is used, and this is later compared to the shorter inlets, which are the same size as the outlets.

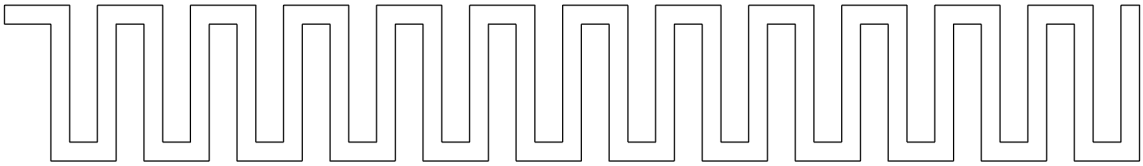

Figure 3.3: Zigzag inlet of electrolyser. The flow enters on the left and enters the active cell area on the right.

3.2. COMSOL Model

One or various modules must be chosen to build the COMSOL model. The main one is the Water Electrolyzer module. Also, a module for the flow has to be selected depending on the flow type through the system.

3.2.1. Water Electrolyzer

The water electrolyzer is a standard module of COMSOL [70], which has been adapted to match XINTC test cells. This module is used for modelling the alkaline electrolysis reactions. The electrolyte, hydrogen gas, and oxygen gas phases are assigned, as well as the current collectors (electrodes) and the separators (diaphragm). The module calculates the required input currents using a range of produced voltages. The cells are connected in series, so the current should be constant.

This module produces several results. Firstly, a polarisation plot is made for the range of calculated current densities versus the cell potential. Also, the electrode and electrolyte potential are visualised, and the Faraday and total efficiency of the stack are calculated and plotted. These are calculated using equations 3.1 and 3.2. The found graphs can be fitted to match the experimental data by varying three parameters, being the permeability of the membrane (between 30% and 50%), and the exchange current densities of the anode and cathode (between 10^{-6} and 100 A/m^2). The peak of values for the cathode lies between 1-10 A/m^2, while this peak is lower for the anode, around 10^{-3} to 10^{-1} [71–75]. The main goal of using this module is to determine the basic electrochemical relations caused by the electrolysis reactions.

$$\eta_{coulombic} = \frac{\sum i_{H_2}}{i_{stack} \cdot N_{cells}} \tag{3.1}$$

$$\eta_{total} = \frac{\sum i_{H_2} * E_{eq,cell}}{i_{stack} \cdot E_{stack}} \tag{3.2}$$

in which $\sum i_{H_2}$ is the total current used for hydrogen production and i_{stack} is the inlet current.

3.2.2. Laminar Flow

The Reynolds number needs to be determined to determine if the flow is laminar or turbulent. This is calculated in the following steps:

$$Re = \frac{\rho v D}{\mu} \tag{3.3}$$

in which ρ is the density of the electrolyte:

$$\rho = \frac{\text{total mass}}{\text{total volume}} = \frac{300\text{kg} + 700\text{kg}}{0.142\text{m}^3 + 0.700\text{m}^3} = 1188\text{kg/m}^3 \tag{3.4}$$

and v is the velocity of the fluid:

$$v = 300\text{cm}^3/\text{min} = 2.083\text{cm/s} \tag{3.5}$$

using an inlet height of 1.2cm and a width of 2.0cm. Using these values, also the equivalent diameter can be calculated:

$$D_{eq} = \frac{4 \cdot A}{P} = \frac{4 \cdot 2.0 \cdot 1.2}{2.0 + 2.0 + 1.2 + 1.2} = 1.5\text{cm} \tag{3.6}$$

Lastly, the viscosity of the mixture is taken to be 1.7mPa·s [76]. Combining all of the above, a Reynolds number of 218 is found. For a Reynolds number smaller than 2000, the flow is assumed to be laminar, so in this case, it is valid to assume that the flow in the electrolyser is laminar. The laminar flow module is used in the COMSOL model to help model the flows in the system and calculate more accurate results using the Water Electrolyzer module.

By calculating the results whilst using the two modules above, several plots can be produced. Firstly, the coulombic efficiency (also known as the Faraday efficiency) for several inlet currents can be plotted. This efficiency is calculated as in equation 3.1. Also, the leakage current for each of the four escape options per cell (two inlets and two outlets) is calculated and plotted per cell. This can then be used to plot the current through the cells by subtracting all losses.

3.3. Equivalent Electrical Circuit (EEC) Model

Rather than using physical relations, Jupudi et al. [20] researched quantifying leakage currents using an electrical circuit. By calculating all resistances, they attempted to find the fraction of current leaking per cell by finding the resistance for each possible path. All inlet resistances only consider the electrolyte resistance, but the gas fraction is also considered for other resistances throughout the cell. However, much rewriting is needed to solve this set of equations simultaneously, including some simplifications. The results obtained from implementing the work by Jupudi et al. show a near-constant current leakage throughout the stack, which does not seem physical. As will be demonstrated throughout this thesis, the observed behaviour may stem from a numerical artefact resulting from the use of difference calculus by Jupudi et al. [20].

Therefore, a new model of the electrolyser stack was developed based on an equivalent electrical circuit (EEC), as shown in figure 3.4, for which all resistances need to be defined. To do so, first, the molarity and conductivity need to be determined. The molarity (mol/L) and conductivity (S/cm) of the electrolyte are both temperature dependent and calculated as in equations (3.7, 3.8) for a KOH-solution with a weight percentage of 30% [77, 78]:

$$m = wt * \left(183.1221 - 0.56845 * T + 984.5679 * \exp\left(\frac{wt}{115.96277}\right)\right)/(100 * 56.105) \tag{3.7}$$

$$k = -2.041*m - 0.0028*m^2 + 0.005332*m*T + 207.2*\frac{m}{T} + 0.001043*m^3 - 0.0000003*m^2*T^2 \tag{3.8}$$

Furthermore, the gas fraction in the outlet ports of the anode and cathode section needs to be calculated before determining the various resistances. This is done in the following steps [79, 80]:

$$\theta = \left(-97.25 + 182 * \left(\frac{T}{T_{ref}}\right) - 84 * \left(\frac{T}{T_{ref}}\right)^2\right) * \left(\frac{I}{30 * A}\right)^{0.3} \tag{3.9}$$

$$\epsilon = \frac{2}{3} * \theta \tag{3.10}$$

$$\begin{aligned} a_{e,C} &= 2 * \epsilon \\ a_{e,A} &= \epsilon \end{aligned} \tag{3.11}$$

where θ is the bubble coverage, ϵ is a factor for calculating the void fraction in the electrolyte, with $T_{ref} = 300K$, and $a_{e,C/A}$ is the gas fraction at the top of the electrolysis. Several equations can be used to describe the increased resistance due to the gas fraction at the outlet. In this thesis, the Maxwell relation is chosen [36]. The various resistances in the electrolyser can be calculated as follows:

$$R_i = \frac{L_i}{kA_i} \tag{3.12}$$

in which R_i is the inlet resistance, L_i is the length of the inlet, k is the conductivity, and A_i is the area through which the fluid flows in the inlet.

$$R_{m,i} = \frac{L_{m,i}}{kA_{m,i}} \tag{3.13}$$

in which $R_{m,i}$ is the resistance of the manifold connecting the inlets, $L_{m,i}$ is the length of the manifold, k is the conductivity, and $A_{m,i}$ is the area through which the fluid flows in the manifold.

$$R_e = R_i * \mathrm{g}(a_{e,C/A}) \tag{3.14}$$

$$R_{m,e} = R_{m,i} * \mathrm{g}(a_{e,C/A}) \tag{3.15}$$

in which R_e is the resistance of the outlet, $R_{m,e}$ is the resistance of the manifold connecting the outlets, $\mathrm{g}(a_{e,C/A})$ is a function of the gas fraction at the top of the cell, as described via the Maxwell relation [36]:

$$g(x) = \frac{1 + 0.5 \cdot x}{1 - x} \tag{3.16}$$

R_e can also be calculated using the Bruggeman relation, which, for the range used in this work, gives the same values as the Maxwell relation [36]:

$$R_e = \frac{d_{C/A}}{kA} \cdot (1 - a_{e,C/A})^{-1.5} \tag{3.17}$$

in which R_e is the electrolyte resistance for the anodic or cathodic side. $d_{C/A}$ is the cathodic or anodic gap, and ϵ is the void fraction in the electrolyte.

$$R_s = \frac{{\tau_s}^2 \cdot d_s}{k \cdot A \cdot \omega_s \cdot \epsilon_s} \tag{3.18}$$

where τ_s is the tortuosity, ω_s is the wettability, and ϵ_s is the porosity of the membrane. Other cell resistances, namely the extra resistance due to the cathodic and anodic overpotentials, are added to the diaphragm resistance in the model since the electrodes are next to the diaphragm. If the current is smaller than four times the exchange current density, then the overpotential is calculated as follows:

$$U_{cath/an} = \frac{R \cdot T}{z \cdot \alpha_{C/A} \cdot F} \cdot \operatorname{arcsinh} \frac{I}{2 \cdot i_{0,C/A}} \tag{3.19}$$

If the current is bigger than four times the exchange current density, then the overpotential is calculated using the Tafel equation:

$$U_{cath/an} = \frac{R \cdot T}{z \cdot \alpha_{C/A} \cdot F} \cdot \ln \frac{I}{i_{0,C/A}} \tag{3.20}$$

The electron transfer coefficients for a 30wt% KOH only depend on the temperature and can be calculated using the following relations [36, 81]:

$$\alpha_a = 0.0675 + 0.00095 * T \tag{3.21}$$

$$\alpha_c = 0.1175 + 0.00095 * T \tag{3.22}$$

Using all resistances above, an electrical circuit can be made in Python using the PySpice module. The resistance scheme was created for N number of cells, and using a simulator, the current at all resistances could be calculated, of which the final result is shown in figure 3.4. All named nodes and resistances need to have an individual number to calculate the current and voltage for individual resistances. Therefore, these are all numbered, using seven resistances and 11 nodes per cell. Since the default setting of Python is to start counting at 0 instead of 1, n needs to be replaced with n+1 in Python.

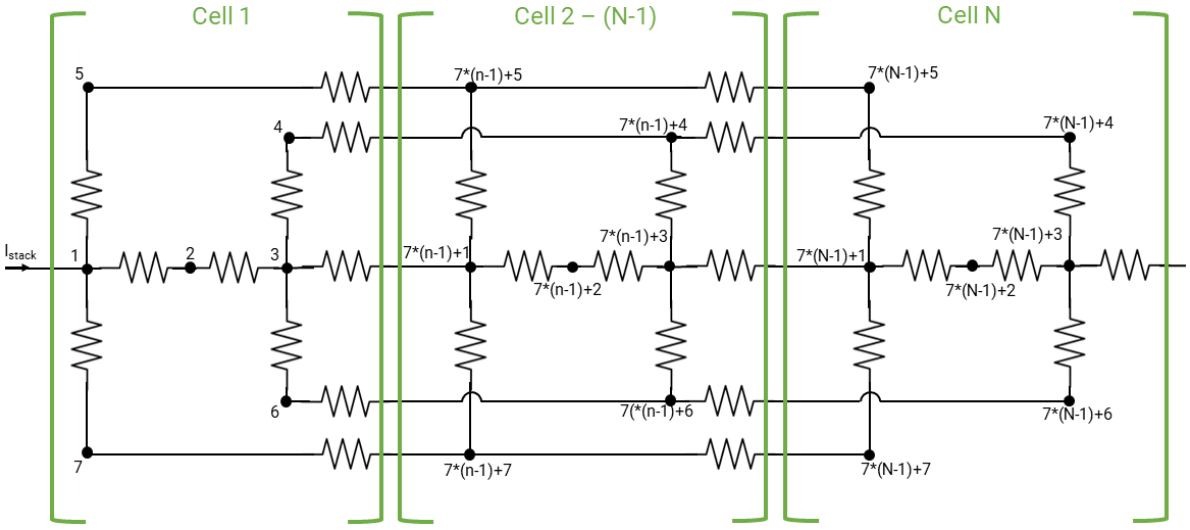

(a)

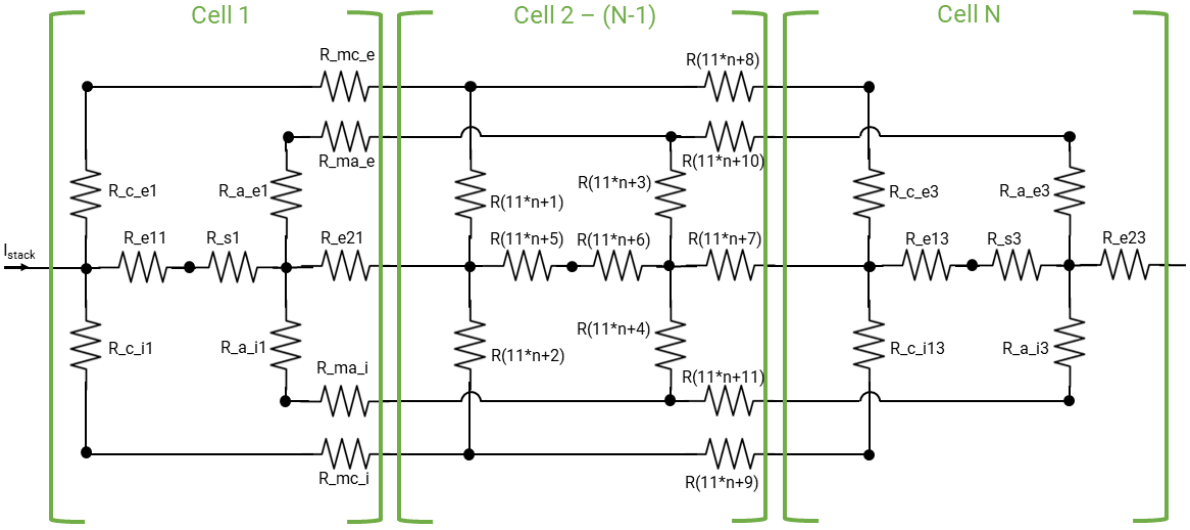

(b)

Figure 3.4: Resistance scheme of the EEC model with the names for the nodes (a) and the resistances (b). Cell 1 and N are fixed, but the middle cell can be repeated for N number of cells. To use the names for these nodes in Python, replace n with n+1.

3.3.1. Predicting Model for Exchange Current Densities

XINTC made the basis for a model in Python that can predict exchange current densities in a one-dimensional electrolysis cell. This model is made using the same resistances as above and using these to calculate the voltage in all resistances for a chosen current. An error is calculated as the difference between the found voltage using experiments and the modelled voltage. The exchange current densities are then determined by minimising this error. The initial guesses were 5.0A/m^2 and 0.01A/m^2 for the cathodic and anodic sides, respectively. The limit to find the exchange current densities was from 10^{-6} to 1 A/m2 for each fitting parameter.

3.4. Pressure Drop

An estimate can be made for the pressure drop in the test cells. The flow rate through each cell is 300mL/min, which translates to 5.0cm^3/s. Considering the depth of 18.3cm and width of 1.2mm per half cell, the flow velocity is 2.28cm/s for each half cell. First, the hydraulic diameter of the cell is

$$D_{H,cell} = \frac{4 * \text{area}}{\text{wetted perimeter}} = \frac{4 \cdot 18.3 \cdot 0.12}{2 * (18.3 + 0.12)} = 0.24\text{cm} \tag{3.23}$$

All pressure drops present are pictured in 3.5. These pressure drops are calculated individually below.

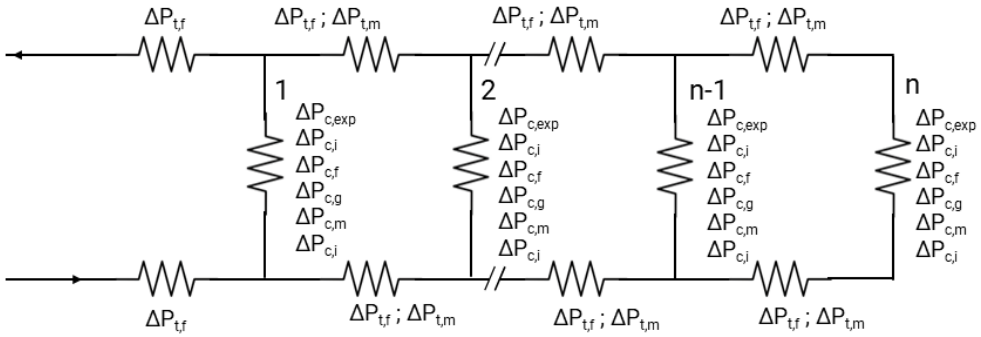

Figure 3.5: Pressure resistance scheme for n cells in an electrolyser stack. The bottom and top horizontal lines represent the manifold resistances, while the vertical resistance represents all inlet, outlet and cell resistances.

3.4.1. Frictional Loss Cell

The hydraulic diameter calculated above can then be used to estimate the Reynolds number in the half cell:

$$\text{Re}_{D,cell} = \frac{\rho U_c D_H}{\mu} = \frac{1188 \cdot 0.0228 \cdot (2.38 \cdot 10^{-3})}{1.7 \cdot 10^{-3}} = 38 \tag{3.24}$$

Using the relation of $f = 14.2/Re$ from chapter 2, it was found that this Reynolds number corresponds to a friction factor of $f = 0.37$. Now, the pressure drop per half cell can be calculated as follows:

$$\Delta P_{c,f} = f \cdot \frac{L_c}{D_H} \cdot \frac{\rho U_c^2}{2} = 0.37 \cdot \frac{0.083}{2.38 \cdot 10^{-3}} \cdot \frac{1188 \cdot (2.28 \cdot 10^{-2})^2}{2} = 4.02\text{Pa} \tag{3.25}$$

3.4.2. Frictional Loss Manifold Tube

The pressure drop in the connecting manifold tubes can also be calculated. The volumetric flow rate in the tubes is eight times the 300mL/min, which equals 40cm^3/s. The hydraulic

diameter of the tube is

$$D_{H,tube} = \frac{4 * \text{area}}{\text{wetted perimeter}} = \frac{4 \cdot 1.2 \cdot 2.0}{2 * (1.2 + 2.0)} = 1.5\text{cm} \tag{3.26}$$

Considering the height of 1.2cm and the width of 2.0cm, the flow velocity in the manifold tubes is 16.7cm/s. The Reynolds number now becomes:

$$\text{Re}_{D,tube} = \frac{\rho U_t D_t}{\mu} = \frac{1188 \cdot (16.7 \cdot 10^{-2}) \cdot (1.5 \cdot 10^{-2})}{1.7 \cdot 10^{-3}} = 1750 \tag{3.27}$$

This gives a friction factor of $f = 0.008$. The pressure drop now becomes:

$$\Delta P_{t,f} = f \cdot \frac{L_t}{D_t} \cdot \frac{\rho U_t^2}{2} = 0.008 \cdot \frac{9.54}{0.015} \cdot \frac{1188 \cdot (16.7 \cdot 10^{-2})^2}{2} = 0.85\text{Pa} \tag{3.28}$$

3.4.3. Frictional Loss Cell Inlets

The volumetric flow rate in the inlets is still 5cm^3/s, which for a height of 1.4cm and width of 0.12cm translates to a velocity of 29.8cm/s. The hydraulic diameter of the inlet is

$$D_{H,i} = \frac{4 * \text{area}}{\text{wetted perimeter}} = \frac{4 \cdot 1.4 \cdot 0.12}{2 * (1.4 + 0.12)} = 0.22\text{cm} \tag{3.29}$$

The Reynolds number then becomes:

$$\text{Re}_{D,i} = \frac{\rho U_i D_i}{\mu} = \frac{1188 \cdot (29.8 \cdot 10^{-2}) \cdot (0.22 \cdot 10^{-2})}{1.7 \cdot 10^{-3}} = 46 \tag{3.30}$$

which, using $f = 14.2/Re$, gives a friction factor of 0.031. This results in a pressure drop of

$$\Delta P_{i,f} = f \cdot \frac{L_i}{D_i} \cdot \frac{\rho U_i^2}{2} = 0.031 \cdot \frac{22.06}{0.22} \cdot \frac{1188 \cdot (29.8 \cdot 10^{-2})^2}{2} = 162.2\text{Pa} \tag{3.31}$$

3.4.4. Gravitational Loss Cell

Then, there's also a pressure drop due to gravity:

$$\Delta P_{c,g} = \rho g h = 1188 \cdot 9.81 \cdot 0.124 = 1445\text{Pa} \tag{3.32}$$

3.4.5. Manifold Loss Cell

The manifold loss coefficient K_{31} can be calculated using figure 2.9 from chapter 2. In this figure, the ratio of volumetric flow rates Q_1/Q_3 = 1/8=0.125 is used to find K_{31} = 0.93. This means that the pressure drop in the tube due to manifold losses are

$$\Delta P_{t,m} = K_{31} \frac{\rho U_t^2}{2} = 0.93 \frac{1188 \cdot (0.167)^2}{2} = 15.3\text{Pa} \tag{3.33}$$

The manifold loss coefficient K_{13} can also be calculated using figure 2.9 from chapter 2. In this figure, the ratio of volumetric flow rates Q_1/Q_3 is 1/8=0.125 and is used to find K_{31} = -0.93. This means that the pressure increases when the flow from the cell is added to the flow in the tube. Therefore, the lost 15.3Pa above is added again to the flow. In reality, the flow velocity will be slightly lower in the upper tube compared to the lower tube due to losses, but this difference is minimal.

3.4.6. Manifold Loss Tube

Using the same method as for the manifold losses in the cell, the manifold losses in the tube can be calculated. In the lower tube, K_{32} = 0 gives a pressure drop of 0Pa per cell. In the upper tube, K_{23} = 0.2 gives a pressure drop of 0.06Pa per cell, so 0.49Pa in total.

3.4.7. Expansion Losses

Using equation 2.52 from chapter 2, K_{exp} is found to be 0.85 and 0.86 for the inlet to cell and outlet to manifold, respectively. This gives a pressure drop of 1.39Pa and 1.40Pa per cell.

3.4.8. Total Pressure Drop

The total maximum possible pressure drop if taken the path of most resistance is

$$\begin{aligned}\Delta P_{tot} &= \Delta P_{t,f} + \Delta P_{t,m} + \Delta P_{c,f} + \Delta P_{i,f} + \Delta P_{c,g} + \Delta P_{c,m} + \Delta P_{c,exp} \\ &= 2 * 0.85 + 0.49 + 4.02 + 2 * 162.2 + 1445 + (15.3 - 15.3) + (1.39 + 1.40) \\ &= 1778.4\text{Pa} = 17.8\text{mbar}.\end{aligned} \tag{3.34}$$

The pressure drop over the inlet is taken twice to consider the outlets. If the inlet is taken three times the normal length to improve results, the total pressure drop becomes 2102.8Pa, equal to 21.0mbar. As shown in the calculations above, the gravitational pressure drop (69%

Also, the manifold losses will be lower for the cells further from the inlet since the difference in volumetric flow rates becomes lower. Therefore, this resistance will decrease. The manifold pressure drop is minimal compared to the total pressure drop (0.1%), so this will only have a small effect. Furthermore, it is now assumed that the gas fraction is tiny so that the top flow will be almost single-phase. This gas fraction could have values up to 36%, giving very different results.

In conclusion, the pressure drop is very small and will be mainly determined by the gravitational losses due to the upward flow stream.

If these calculations are repeated for 100 cells, the pressure drop becomes only slightly higher due to the extra manifold length, resulting in a pressure drop of 23.7mbar. Since the allowable pressure drop in this part of the system is set to 500mbarg by XINTC, this is well within limits. To calculate the pressure drop in COMSOL Multiphysics, a lot of extra computing power is needed, and because the pressure drop is already very low, this is not modelled.

4

Results

This chapter discusses the results from the experimental setup of the test cells, the COMSOL model, and the equivalent electrical circuit model (EEC model) for a 2D single-cell setup and a 3D setup of eight cells. Furthermore, the expected effect of scenarios on the leakage currents is predicted.

4.1. Single-cell in 2D

Firstly, single-cell experiments were performed at a temperature of 42.5°C and ambient pressure. The current was varied from 13mA/cm^2 to 156mA/cm^2. The found results are shown in figure 4.2 as blue dots and used to validate the COMSOL and EEC model. The models were fitted so that the error between the model and the experimental data was minimal.

In the Water Electrolyzer module, the gas fraction is taken into account as well. However, it needs an initial guess. A sensitivity analysis shows that this initial guess results in a deviation from the results found mainly for lower currents (below 78mA/cm^2) with a maximum of 1.5% between the initial guess of 0.01 and 0.3 gas fraction, as shown in figure 4.1. For a current density of 156mA/cm^2, the theoretical maximum gas fraction is 0.36. For a current density of 33mA/cm^2, the gas fraction is 0.1. A gas fraction of 0.01 is reached for a current density of only 3mA/cm^2. The results in figure 4.1 show that the found curves differ only slightly for the different input values. The higher the initial guess for the gas fraction, the lower the curve will start and the steeper the gradient towards higher current densities.

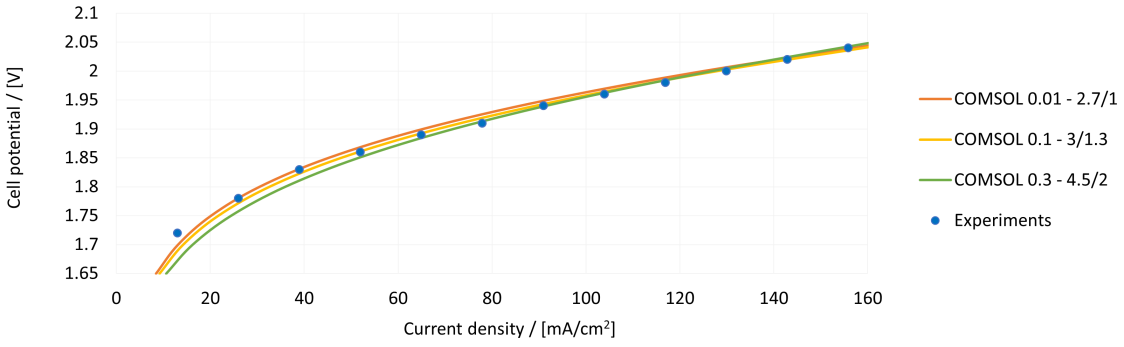

Figure 4.1: Polarisation plot of COMSOL results with varying input versus experimental data. The different fitting options have gas fraction varying from 0.01 to 0.3, and a cathodic and anodic exchange current density fit. This is shown in the legend as *COMSOL 'gas fraction' - cathodic exchange current density/anodic exchange current density* [A/m2].

Based on literature from section 3.2.1, initial guesses for the cathodic and anodic exchange current densities were 5 and 0.01A/m^2, respectively. These were then changed based on the result of the fit. The lower these parameters, the higher the cell potential would be for a constant current. The diaphragm porosity had to be between 0.3 and 0.5. The lower this porosity, the steeper the curve for the higher currents. This is due to the higher resistance of the diaphragm for lower porosity, which results in a higher required voltage, as per $V = I * R$.

It was found that the COMSOL model could be better fitted to the experimental data for high porosity, so 0.5. For this diaphragm porosity of 0.5, the cathode and anode exchange current density were found to be 3.0A/m^2 and 1.3A/m^2, respectively. Using the EEC model with the same membrane porosity, the models could be fitted using a cathode and anode exchange current density of 0.25A/m^2 and 0.05A/m^2, respectively. This fit is shown in figure 4.2. For cell currents lower than 40mA/cm^2, the COMSOL model estimates a lower voltage than found in experiments, while the EEC model predicts a higher voltage than found in experiments below 30mA/cm^2.

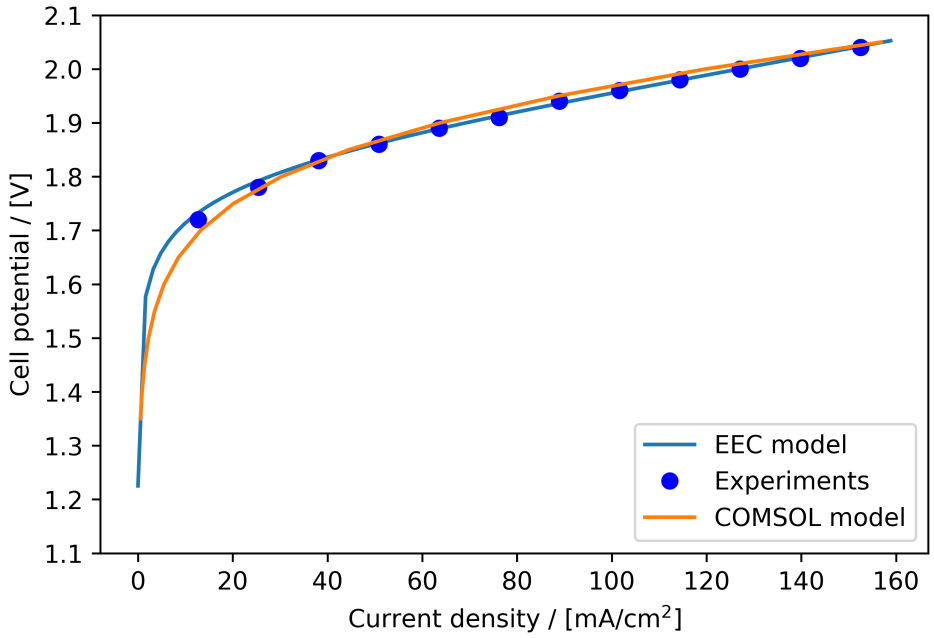

Figure 4.2: Polarisation curve of a single cell with results from experiments (blue dot), COMSOL model (blue line), and EEC model (orange line). All results are obtained for T=42.5°C and ambient pressure. In the COMSOL model, the anodic exchange current density is fitted for 1.3A/m^2, and the cathodic exchange current density is fitted for 3.0A/m^2. In the EEC model, the anodic exchange current density is fitted for 0.05A/m^2, and the cathodic exchange current density is fitted for 0.25A/m^2.

The used α_c and α_a are 0.42 and 0.37, respectively. In COMSOL, however, the model uses an input for α_a and assumes that α_c equals 1-α_a. This is an ideal case, which, for the conditions used in this thesis, is incorrect. To implement the small difference in transfer coefficients, the used α_c and α_a in COMSOL are 0.53 and 0.47, respectively, which gave the results above. As the Butler-Volmer equation shows, if the transfer coefficient increases, then the overpotential decreases. The only other parameter that can be changed is the exchange current density to get to the higher overpotential to fit the model. The lower this parameter, the higher the overpotential becomes. However, this parameter is inside a log function (or sinh for the lower current densities) and, therefore, decreases exponentially, which greatly changes the found parameters. The total current and potential through the system then needs to be

recalculated. To quantify the effect of the higher transfer coefficient on the exchange current densities, the higher transfer coefficients were entered into the EEC model, and new exchange current densities were calculated. To find an acceptable fit, the found exchange current densities were 10-20 times smaller than the original ones found in the EEC model. These results are discussed in more detail in appendix A. In conclusion, the resulting exchange current densities were 10-25 times higher in the COMSOL model than in the EEC model, and these are around 3-10 times too high if corrected for the higher transfer coefficient. Therefore, this cannot be compared between models and is only used as an estimate for the 3D models.

At low currents, non-linear behaviour is shown in figure 4.2, which is due to overpotentials as described in chapter 2. These losses become close to constant for higher currents since the overpotential is described by a logarithmic function (the Tafel equation). The potential also increases linearly with the ohmic losses, which are mainly the resistance of the electrolyte and the diaphragm.

In this work, the Tafel equation is used in the EEC model to calculate the overpotential. However, for low current densities, a sinus hyperbolic function is used. To explain the difference between those functions, the graph in figure 4.3 is made [82]. If the value for the electron transfer coefficient (α) is taken to be 0.5, then the sinh function matches the Butler-Volmer equation perfectly. In this thesis, α is taken to be 0.42 and 0.37 for the cathodic and anodic side, respectively, following equations 3.22 and 3.21. Then, the sinh-function gives only slightly higher but practically the same results for low current densities compared to the Butler-Volmer equation using those same transfer coefficients. If α were bigger than 0.5, the sinh-function would give lower results than the original Butler-Volmer equation. As shown in figure 4.3, the sinh-function is a better approximation than the Tafel equation for current densities smaller than four times the exchange current density. As shown in figure 2.4 from chapter

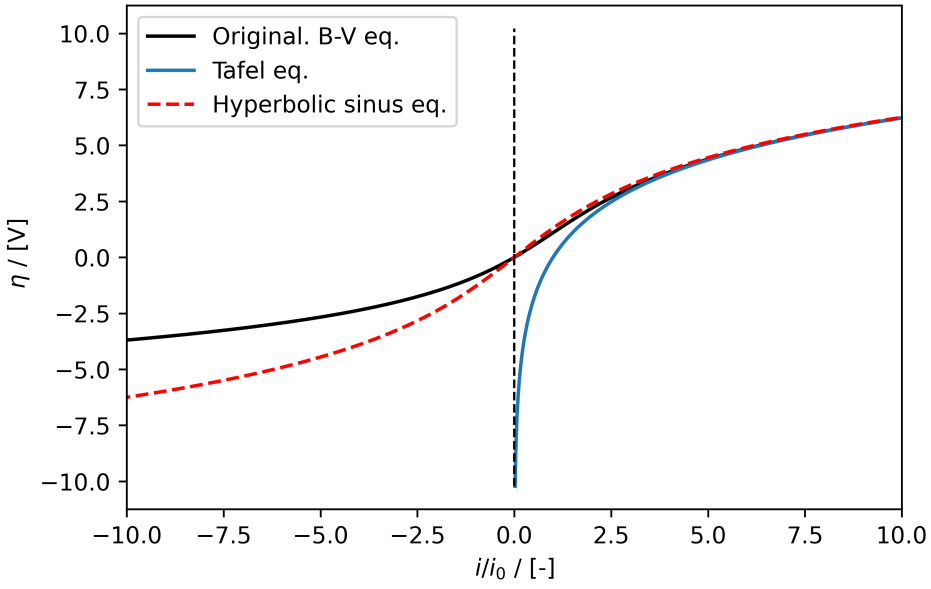

Figure 4.3: Comparison of overpotential for α=0.37 using the original Butler-Volmer equation (black line), the Tafel equation (blue line), and the sinus hyperbolic function (red dashed).

2, the overpotentials make up a large part of the cell potential. The guessed exchange current densities largely affect these overpotentials. Figure 4.4 is made to show the effect of the exchange current density value. This indicates that each time the exchange current density increases with a factor of 10, the cell potential drops by about 8%. Based on the results above, the found exchange current density in COMSOL is around 10-25 times higher than predicted in

the EEC model, which could give a deviation in the polarisation curve of 8-11%. In both models, it is assumed that the only extra cell resistance comes from the electrode overpotentials and the porosity of the diaphragm. However, as described in section 2.4, the overpotential could come from multiple resistances in the cell. For the EEC model, these resistances are calculated via the equations in chapter 3. For the COMSOL model, it is not exactly known how this is calculated, so the various resistances in the cell might be underestimated compared to the assumptions made for the EEC model. Therefore, the overpotential must be higher to mimic extra resistance within the cell.

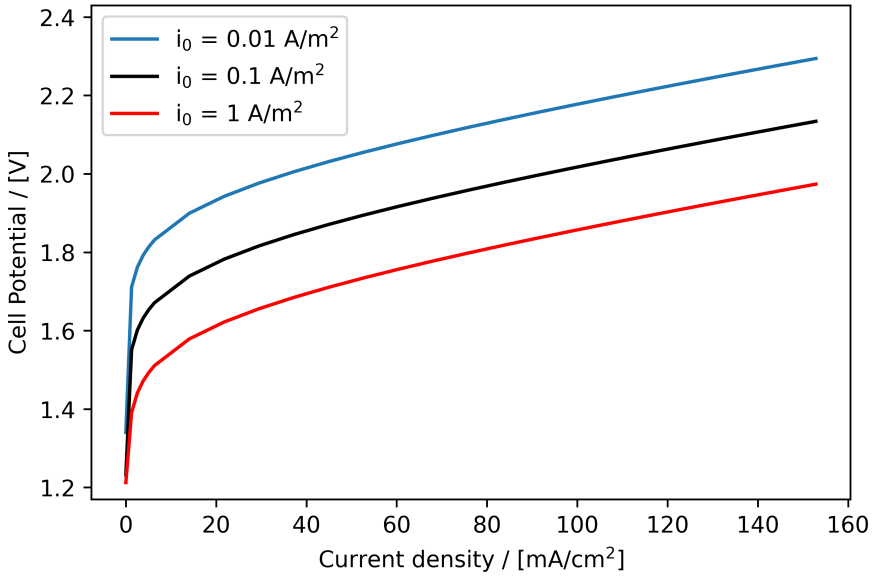

Figure 4.4: Comparison of various exchange current densities and the effect on the polarisation curve for T=42.5 °C and atmospheric pressure. When increasing the exchange current density with a factor of 10, the curve decreases by 8%.

4.2. 8-cell Stack in 3D

While the 2D analysis is mainly used to determine the relative fitting parameters and research if the models are comparable, the 3D analysis is focused on finding the effects of various parameters on the leakage currents. The data needed for validating these models was gathered using experiments of an 8-cell electrolysis stack. In this second part, the multi-cell experiments were performed at a temperature of 42.5°C and ambient pressure. Again, the current was varied from 130A/m^2 to 1558A/m^2, of which the found polarisation curve is shown in figure 4.6 as the light-blue line. The models were fitted to this experimental data using the same procedure as before to minimise errors between the experiments and models.

4.2.1. Design COMSOL Model

The electrolyser was first modelled in 3D in COMSOL, using the same parameters found in 2D of 3.0A/m^2 and 1.3A/m^2 for the cathodic and anodic exchange current density and a diaphragm porosity of 50%. In the 2D model, it was not possible to use the input transfer coefficients of α_a=0.37 and α_c=0.42 and therefore, the exchange current densities are underestimated compared to the 3D model since it is possible in the 3D model to use those exact transfer coefficients. After the model was built, the number of cells could be changed to determine how this affects the amount of leakage currents. Firstly, this was done for eight cells.

Monopolar Cells
While XINTC's R&D test setup uses monopolar electrodes connected in series, the Water Electrolyzer module in COMSOL uses bipolar electrodes connected in series. Due to the settings of COMSOL, this could not be changed to monopolar electrodes. When trying to change the design of the bipolar electrodes to mimic monopolar electrodes, this could be done by modelling the bipolar electrode as a hollow electrode where the ends of the plate were still connected and acted as a small conductive piece of metal, as shown in figure 4.5. It was found that modelling the electrodes as two plates with connecting wires was unnecessarily complicated. In calculations, this hollow electrode would come down to the same results as a bipolar electrode. The polarisation curve and the Faraday efficiency remained the same for the bipolar and monopolar electrodes. The shunt currents per cell would shift, but the total losses remained unchanged. Therefore, it was chosen to do further modelling with bipolar plates. The produced figures for a monopolar and bipolar system are enclosed in appendix B.

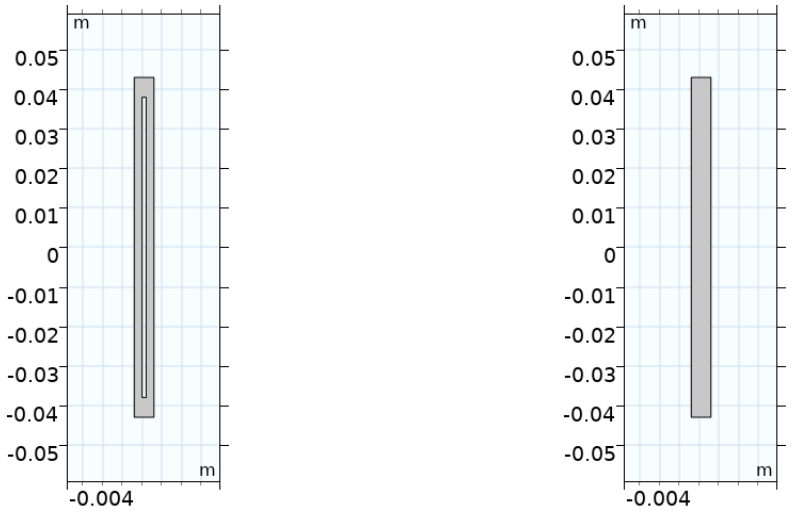

Figure 4.5: Monopolar (a) and bipolar (b) geometry of the electrode.

The COMSOL model was fitted to match the experimental results. The parameters used as input are shown in table 4.1. This gave fit for a diaphragm porosity of 0.50 again, the cathode and anode exchange current densities were found to be 6A/m^2 and 1.4A/m^2, respectively. The resulting polarisation curve is shown in figure 4.6. In this figure, the current is modelled from 130A/m^2 to 1558A/m^2. The modelled polarisation curve matches the experimental data well for the used fitting parameters, but the shape is different. The experimental data follows a more linear increase, while the COMSOL model predicts a curved line for lower currents. To increase this curve at the lower currents, there should be higher losses for these lower currents in either the electrode overpotentials, the electrolyte or the diaphragm. As described before, the electrode overpotentials can be increased, but this would lead to an upward shift of the whole polarisation curve, as shown in figure 2.4. The electrolyte resistance cannot be changed when COMSOL is used because none of the input values directly affect this. Also, as described in chapter 2, the electrolyte resistance is very low compared to the other resistances, especially for low currents. At these lower currents, the gas production is also lower, which means there is very little extra resistance due to bubbles. The curve at lower currents can also be steeper by increasing the diaphragm resistance, which is done in COMSOL by increasing

its porosity. However, then the whole curve becomes steeper and does not fit anymore for currents larger than 35mA/cm^2. In conclusion, the model predicts a lower cell resistance for low currents (<35mA/cm^2), but this is the best fit overall.

Table 4.1: Input constants for COMSOL model

	Name	Value
Height of active cell area	H_{cell}	83 mm
Width of active cell area	W_{cell}	182.6 mm
Anode/cathode gap	$d_{a/c}$	1.2 mm
Diaphragm thickness	d_s	0.6 mm
Length of long horizontal part inlet	$L_{i,1}$	153 mm or 459 mm
Length of short vertical part inlet	$L_{i,2}$	35 mm
Manifold height	H_{holes}	12 mm
Manifold width	W_{holes}	20 mm
Electrode thickness (bipolar)	d_e	2 mm
Electrode material	Nickel	
Electrolyte KOH	wt	30wt%
Electrolyte flow per half cell	Q_{cell}	0.3L/min
Initial gas fraction bottom cell	$\phi_{g,low}$	0.0
Initial gas fraction top cell	$\phi_{g,up}$	0.3
Cathodic transfer coefficient	α_c	0.42
Anodic transfer coefficient	α_a	0.37

The Faraday efficiency corresponding to these parameters is shown in figure 4.7. While the polarisation curve matches well, the Faraday efficiency of the COMSOL model is higher than that of the experiments. Both the experiments and the COMSOL model show very high efficiency, but this is expected because the inlet of the experiments was longer and narrower than the outlets.

The Faraday efficiency of the experimental results is determined by dividing the measured hydrogen gas production by the single-cell gas production for that current instead of the theoretical maximum. In COMSOL, it is assumed that the maximum hydrogen production in a single cell is the theoretical maximum corresponding to the current. Still, there was a systematic error in the experimental setup, as shown in figure 4.8 of 0.02463±1% L/min. Using the trendline, this means that 223.9A/m^2 was lost. When this error was subtracted from the results found in the experiments with eight cells, the results are as in figure 4.7.

The flow meters have a reported accuracy of ±0.2%, which would not explain this loss. Nevertheless, whether the meters were calibrated well is unclear, which could have led to this offset. It could also come from somewhere else in the setup since fluid leaked from the stack. However, since the offset is constant, it is more likely that this comes from a calibration error. It is implausible that it comes from the electrical circuit because the measurements for the polarisation curve did not have an offset of 223.9A/m^2 in the inlet current.

4.2.2. Meshing Sensitivity

A meshing sensitivity was performed to determine the size of the elements. This analysis aimed to determine the optimum meshing size concerning the calculation time of the model and the accuracy of the results. Table 4.2 shows the meshing size, number of elements, and calculation time. The stack current, the Faraday efficiency, and the current used for hydrogen production were calculated for every element size. It was found that the most significant absolute and fractional deviation was in the current for hydrogen production, so this data set was

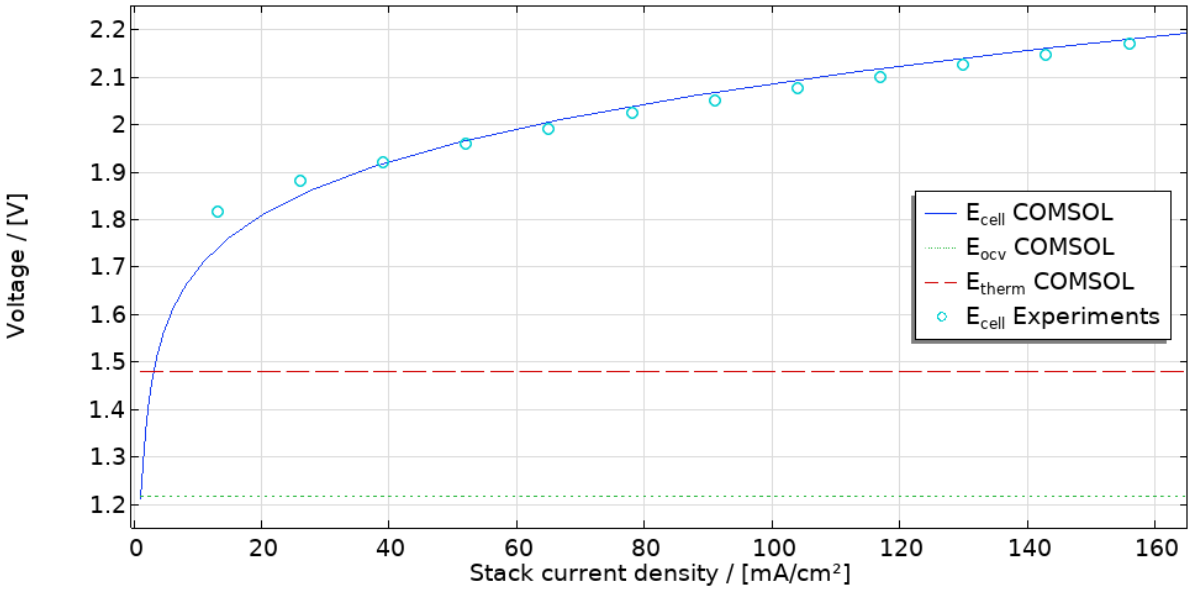

Figure 4.6: Polarisation curve of an electrolysis stack comprising eight cells of experimental data compared to COMSOL model. Experiments were performed for T=42.5°C and ambient pressure. The anodic exchange current density is fitted for 1.4A/m², and the cathodic exchange current density is fitted for 6.0A/m².

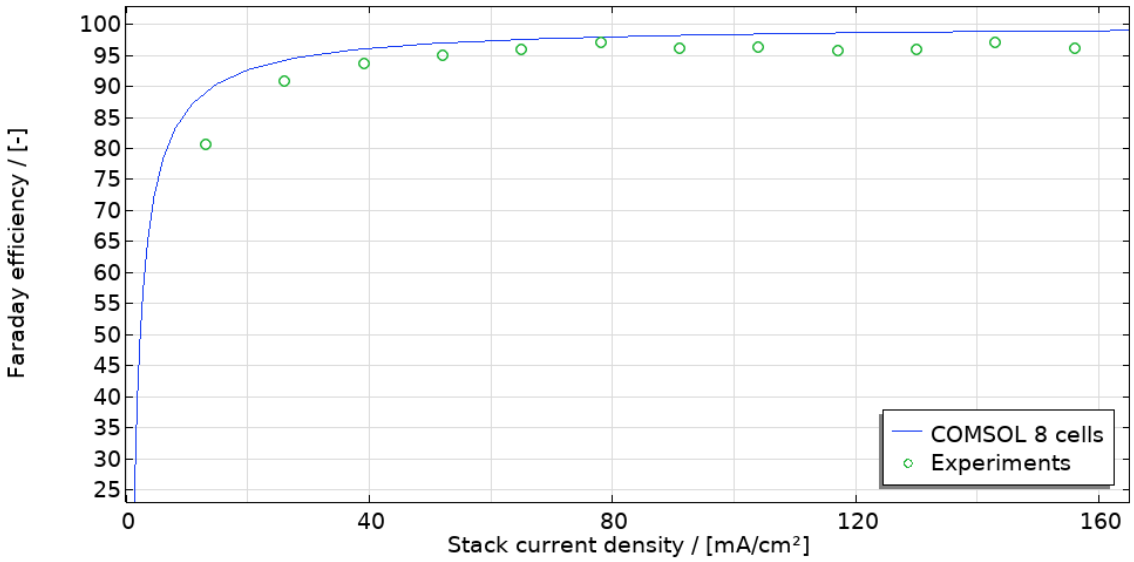

Figure 4.7: Faradaic efficiency of an electrolysis stack with zigzag inlets comprising eight cells of experimental data compared to COMSOL model.

Table 4.2: Mesh input with resulting number of elements and calculation times for meshing sensitivity analysis.

Meshing	Minimum element size (mm)	Maximum element size (mm)	Number of elements	Calculation time (s)
Normal	1.43	7.92	77,839	18
Fine	0.792	6.34	120,091	25
Finer	0.317	4.36	382,543	87
Extra fine	0.119	2.77	2,029,209	544
Extremely fine	0.0158	1.58	6,320,984	4105

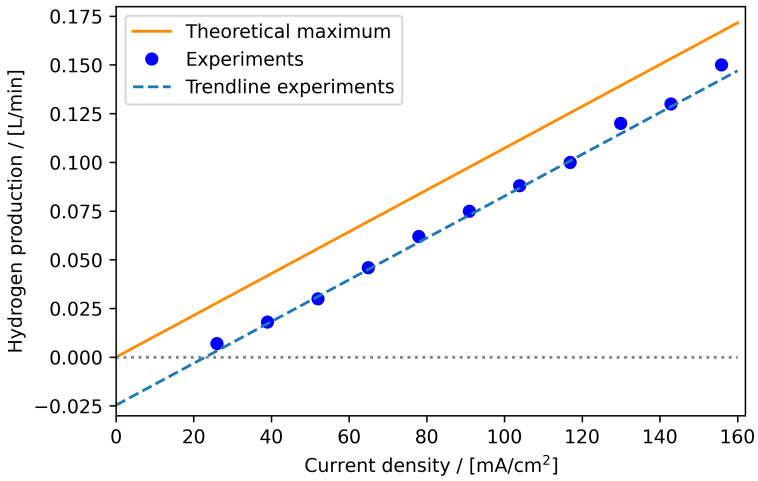

Figure 4.8: Theoretical maximum hydrogen production of a single cell (orange line) compared to the actual maximum hydrogen production of a single cell (blue dot), with a trendline (blue dashed line) following equation $y = 0.00110 * x - 0.02463$. All calculations for a temperature of T=42.5°C and ambient pressure.

used for the meshing analysis. As shown in figure 4.9, the deviation is very low for all element sizes. A first important note is that the smallest length in the model is the thickness of the separator, which is 0.6mm. Therefore, the minimum element size is preferably smaller than 0.6mm. COMSOL is able to create elements with a smaller size than the minimum in such cases, but this would take extra computation time. Based on these criteria and the computation time from table 4.2, the minimum mesh used should be the finer mesh, which takes about 1.5 minutes to calculate. Using the extra fine or extremely fine mesh is optional, but these give only a little extra accuracy while taking over 9 and 68 minutes, respectively, to calculate results. Concluding, the best mesh to use is the finer mesh, with an element size between 0.317 and 4.36mm.

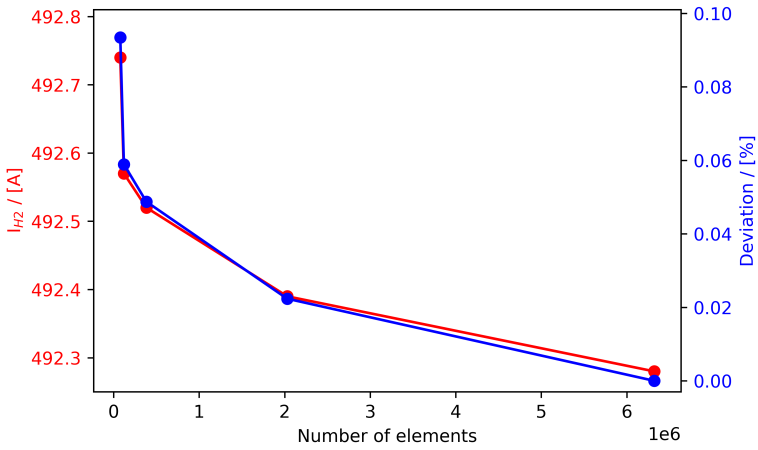

Figure 4.9: Current used for hydrogen production at 2.4V for varying mesh element sizes (red), and its deviation from the result found for the smallest mesh element size (blue).

4.2.3. Design EEC Model

XINTC already had an in-house model designed to solve an electrical circuit based on the work of Jupudi et al. [20]. Jupudi's original work and his derivations suffered numerical issues

for low current densities because it led to negative currents for cells in the middle of the stack. Even for very low current densities, the cell current should stay positive. This problem arose from his derivations since all current versus cell curves had the same curvature. For example, a 100A inlet current would give the same absolute loss in the middle cells as a 10A inlet current, ultimately leading to negative currents. In this work, the electrical circuit was revised and rebuilt using the PySpice module to compare electrical circuits to the experiments and COMSOL model. Both approaches solve first and second Kirchoff's laws for the circuit. However, in the approach by Jupudi, the system of algebraic equations is rewritten to a simplified system of equations using the difference calculus. To the best of our knowledge, this seems to introduce numerical artefacts in the solution, namely near uniform current density across the central cells of the stack. However, Pyspice uses its internal routines to solve Kirchoff's laws and could, therefore, be used to calculate leakage and cell currents for all inlet currents.

Other previous research has looked into multi-cell electrical circuits as a model for leakage currents via resistance ratios [56, 83, 84], or a set of equations based on Kirchoff's laws [20, 85]. However, both methods need simplifications to define this resistance ratio for every single cell.

When using the PySpice module, the voltage and current at every node and resistance can be calculated simultaneously based on the resistances and inlet current. Using the resistance scheme from figure 3.4, the current and potential are calculated for several scenarios. Since all middle cells have the same resistance layout, the model can easily be adjusted for a varying number of cells.

A sinus hyperbolic function was used instead of the Tafel equation for $I/i_0<4$ to find accurate cell potentials for low current densities, as from figure 4.3. The resistances are calculated using equations 3.12 - 3.18 from chapter 3. The found values are shown in table 4.3. It stands out that the inlet resistances are higher than the outlet resistances, but this is due to the inlets being three times as long as the outlets. The inlet resistances increase linearly with the length of the inlet, so if the inlet were to be the same length as the outlet, the resistance would have been 787Ω, which is lower than the outlet resistance. A second important note is that the geometry of the inlet is one of the most determining factors in the amount of leakage current since the resistance of the manifold is lower than the resistance of the cell, next to the resistance of the diaphragm, which varies widely for different input currents.

Table 4.3: Calculated resistances for a current in the range 0.006-156mA/cm². All cell and outlet resistances increase with an increasing current, except for the diaphragm resistance, which increases with a decreasing current.

	Inlet	Outlet
R_a	2361 Ω	796-1030 Ω
R_c	2361 Ω	806-1401 Ω
R_{ma}	0.47 Ω	0.47-0.62 Ω
R_{mc}	0.47 Ω	0.48-0.84 Ω
R_{e1}	0.9-1.2 $m\Omega$	
R_{e2}	0.9-1.2 $m\Omega$	
R_s	47-0.03 Ω	

When calculating the steady state condition of the electrical circuit, the current was varied from 13mA/cm² to 156mA/cm². The input data are shown in table 4.4. Figure 4.10 shows the resulting polarisation curve. By varying the exchange current densities, a fit was found for $i_{0,c}$= 0.064A/m² and $i_{0,a}$= 0.019A/m². The current densities from the single-cell Python model could not be reused as they were found for a different model. As stated earlier, the exchange current densities are used as a fitting parameter to compensate for the missing parts of the overpotential and may, therefore, differ per model. As corresponds to literature,

the model expects to find cell voltages as low as 1.21V when the current approaches 0A. This is expected as this is the equilibrium voltage, the minimum voltage needed for hydrogen production. The model gives a slightly lower cell potential for low currents (<30mA/cm^2), as was also seen in the COMSOL model.

Table 4.4: Input constants for EEC model based on the R&D test cell.

	Name	Value
Height of active cell area	H_{cell}	83 mm
Width of active cell area	W_{cell}	182.6 mm
Anode/cathode gap	$d_{a/c}$	1.2 mm
Diaphragm thickness	d_s	0.6 mm
Length of long horizontal part inlet	$L_{i,1}$	459 mm (inlet), 153 mm (outlet)
Length of short vertical part inlet	$L_{i,2}$	35 mm
Manifold height	H_{holes}	12 mm
Manifold width	W_{holes}	20 mm
Electrode thickness (bipolar)	d_e	2 mm
Electrolyte KOH	wt	30wt%
Electrolyte flow per half cell	Q_{cell}	0.3L/min
Cathodic transfer coefficient	α_c	0.42
Anodic transfer coefficient	α_a	0.37

As for the Faraday efficiency in the EEC model compared to the experiments, the differences are larger than for the COMSOL model, as shown in figure 4.11. This means that the EEC model underestimates shunt currents compared to the results obtained from the COMSOL model. The EEC model only takes into account the resistances calculated in chapter 3 and no electrochemical processes. COMSOL considers more of the cell processes and corrects for that, which results in a lower efficiency. If the efficiency of the EEC model is too high, then this might result from a smaller leakage current. This happens when the resistances in the inlet and outlet channels are set too high, resulting in more current used in the cell for hydrogen production. To adjust the EEC model to match the experimental data, the resistances of the inlets and outlets need to be reduced by at least 50%. From now on, it is chosen not to do this and to use the EEC model for qualitative research.

4.3. Leakage Currents

The effect of leakage currents on the cell current can be modelled by subtracting the losses via all four channels per cell from that cell current, which results in a parabolic curve. In the first few cells, a current is leaked via the inlets and outlets and in the last few cells, this comes back. While comparing the results of the COMSOL and EEC models, it was found that the two models did not have equal amounts of leakage currents when faradaic efficiencies were matched. A closer look into the COMSOL model showed that based on just the leakage currents, the faradaic efficiency should be higher in COMSOL. Since it is unclear where the other losses come from, the actual leakage currents through all four channels per cell were compared.

The results of these leakage currents are shown in figure 4.12. For the model in COMSOL (4.12a), it is found that the leakage occurs mostly via the outlet channels. Since the inlet channels were lengthened, the resistance in these channels increased as well, resulting in less current loss. The loss via the oxygen side is slightly higher than the hydrogen side but very similar. In the EEC model (4.12b), it is also predicted that the current loss is higher via the outlet channels than the inlet channels. The current losses are similar to the COMSOL model.

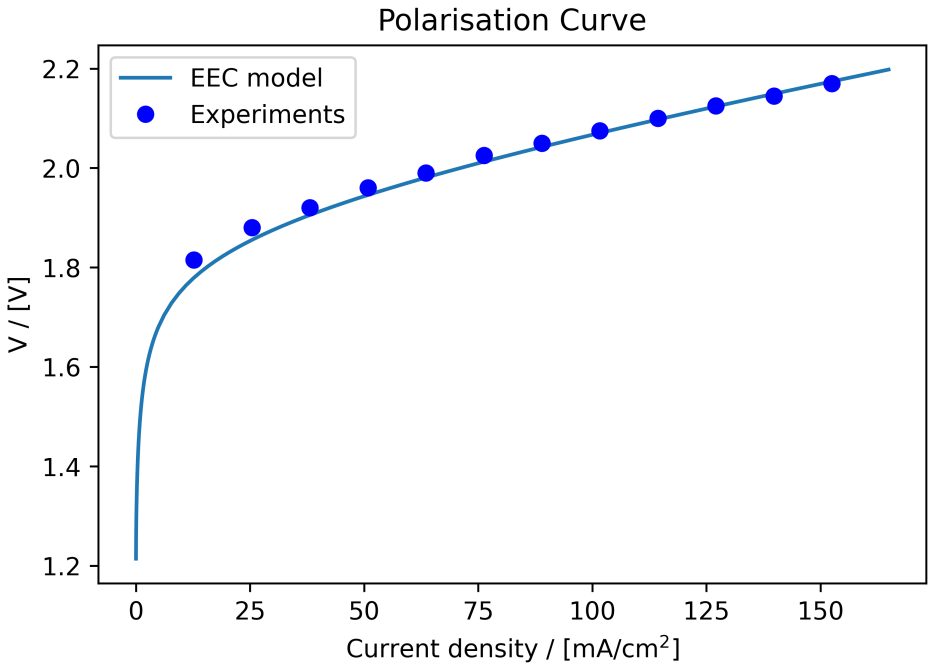

Figure 4.10: Polarisation curve of EEC model fitted to experimental data from the R&D test system with exchange current densities of $i_{0,c}$= 0.064A/m² and $i_{0,a}$= 0.019A/m². The current used is the inlet current, while the voltage is the average measured voltage over the stack. This applies to both the experiments and the EEC model.

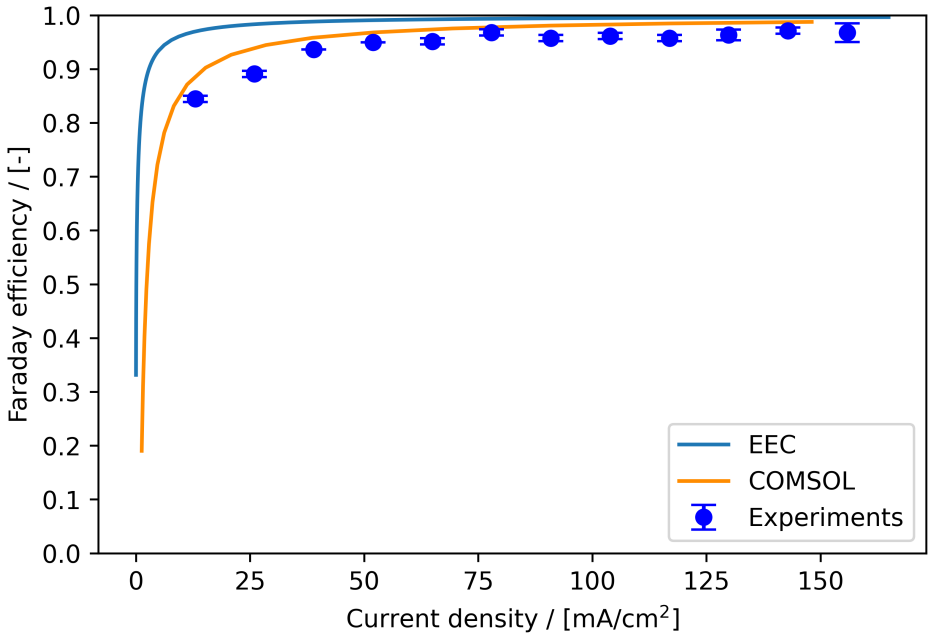

Figure 4.11: Faradaic efficiency of experimental data from the R&D test system, of an electrolysis stack with zigzag inlets, comprising eight cells (blue dots). This is compared to EEC model (light-blue line) and COMSOL model (orange line).

However, the losses via the outlet channels are lower than in COMSOL, while the losses via the inlet channels are higher than in COMSOL. The change in magnitude due to the length of the inlets is not the same for both models.

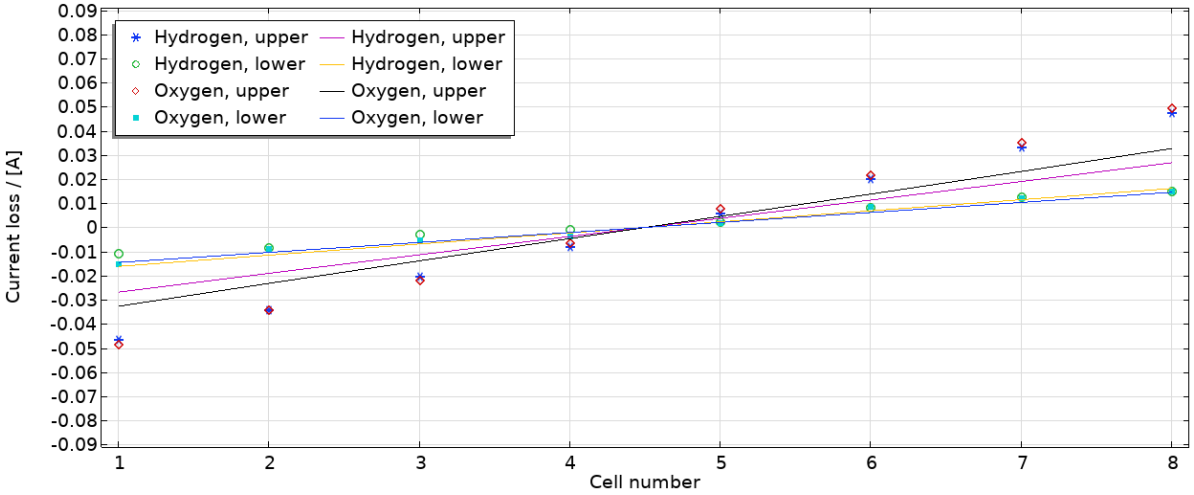

Figure 4.12: Leakage current per cell for each of the two inlets and two outlets in 8 cells. Modelled using COMSOL (o) and EEC (-). Geometry with zigzag inlets.

In both the COMSOL and the EEC model, the leakage current is higher for the outlet channels than the inlet channels. As stated before, this is due to the extra length of the inlet. Therefore, if the inlets were the same length as the outlet, it is expected that the leakage current would be higher via the inlets. There are no bubbles in the inlets, which leads to lower resistance and more loss. To research this, the models were adapted to have shorter inlets to have the same length as the outlets. The resulting leakage currents per cell are found in figure 4.13, which shows that it is indeed true that the losses via the inlets increase. For the COMSOL model (left), the inlet losses were around a fifth of the outlet losses, but this increases to almost double the outlet losses. In the EEC model, the effect is smaller but still visible. The inlet leakage current was around half of the loss via the outlets, increasing to almost double the loss as well. The absolute values for the leakage current are lower than in the COMSOL model, but the trend is the same. Overall, these results show that the inlet length and, therefore, the inlet resistance significantly affect the leakage current.

The higher leakage current for the shorter cell inlets also results in a lower Faraday efficiency, as shown in figure 4.14, compared to figure 4.11. This figure shows that the COMSOL can predict the efficiency of the stack very close to the values found in the experiments. The EEC model still predicts a higher efficiency than found in the data from the experiments, but the efficiency becomes lower than for the longer inlets. The effect of the length of the inlets is smaller in the EEC model than in the COMSOL model, so it might be that the resistance of the inlets is overestimated in the EEC model. In that case, the leakage current will become lower, and more current will be used for hydrogen production, resulting in a higher faradaic efficiency.

To get a better overview of the deviation of both models compared to the experiments, table 4.5 is made. This table presents the Faraday efficiency for both models and the experiments at three different current densities and for long and short inlets. The deviation from the Faraday efficiency of the experiments is higher for lower currents. For higher currents, the deviation becomes around 2.5-4.0% in the EEC model and below 2.5% in the COMSOL model. Since the data points from the experiments fluctuate a little bit (as found in figures 4.11 and 4.14), the deviation fluctuates a little bit as well.

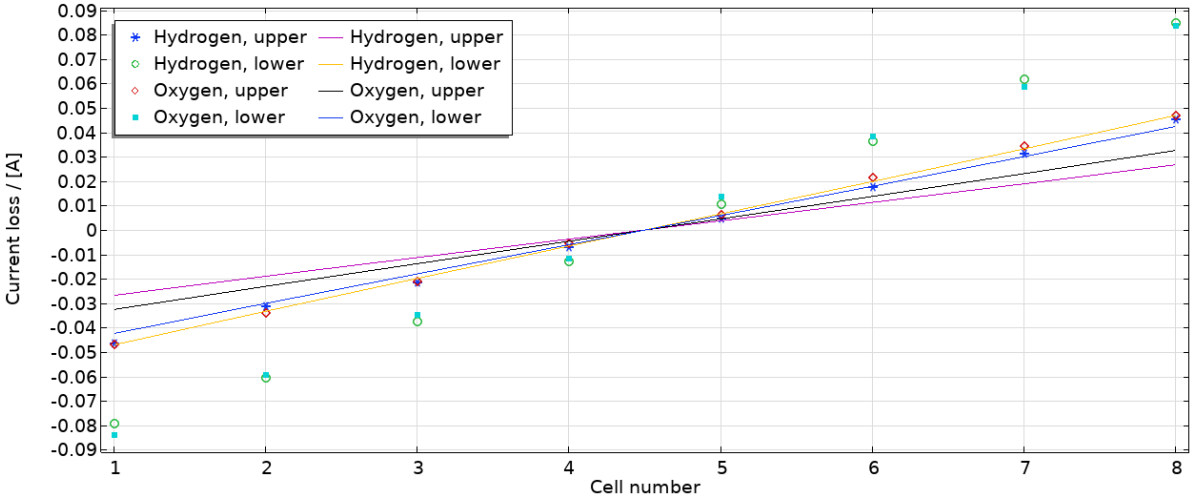

Figure 4.13: Leakage current per cell for each of the two inlets and two outlets in 8 cells. Modelled using COMSOL (o) and EEC (-). Geometry with short inlets.

4.3.1. Knowledge Gap

When comparing the results and performance of both models, it is found that not all is known about the COMSOL model. In the EEC model, every relation and variable is known as the code is developed in-house. However, in COMSOL, a lot is unknown due to it being a commercial software, often described as a 'black box model'. While some parameters have larger effects than others, it is hard to compare the models and see where the differences come from if the information is unknown. As shown in the results section above, the COMSOL model is often better at matching the experimental data, so in the best-case scenario, all input from COMSOL is used in the EEC to research those results. This is impossible, and table 4.6 is made to showcase these struggles. In the EEC model, the reduced conductivity in the electrolyte in the cell, outlets, and manifolds is calculated in three steps. Firstly, a relation from Vogt [79] is used to calculate the bubbling rate, depending on the current and the temperature. This is then used to find the gas fraction, which differs for the cathodic and anodic compartments. Lastly, several equations can be found to calculate the reduced conductivity due to the gas fraction and the relation found by Maxwell is generally used the most [36]. These relations give various results for the increase in resistance but are very similar for gas fractions smaller than 0.2. The Maxwell relation used in the EEC model and the Bruggeman relation used in the COMSOL model give very similar results for gas fractions up to 0.4. This would make little difference since the maximum gas fraction in the experiments was 0.36. Unfortunately, this relation is the only part of the three-step calculation that can be changed since it is unclear how COMSOL calculates the gas fraction in the electrolyte. An initial guess is entered in the input, and the next step in COMSOL is the resulting polarisation curve and efficiency curves. Therefore, the relations used by COMSOL cannot be copied into the EEC model and reduce the difference between the models. In this case, it might very well be that this gas fraction affects the results since the change in leakage current is smaller for the EEC than COMSOL for different inlets.

4.3.2. Prediction for 100 Cells

The expected leakage current for 100 cells can be predicted using the results of both models for eight cells. While the figures for the eight cells show linear behaviour, this is not the case for a higher number of cells. Figure 4.15 shows the expected loss per cell for the long inlets and the shorter inlets of the same length as the outlets. Most loss and return occur in the cell on

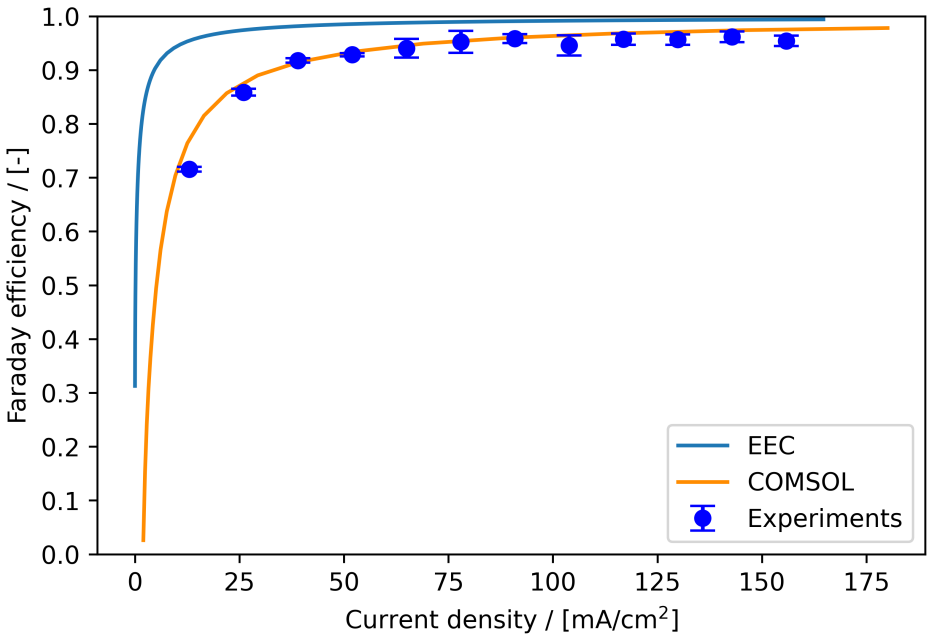

Figure 4.14: Faradaic efficiency of experimental data of an R&D test stack with short inlets, comprising eight cells (blue dots), compared to EEC model (light-blue line) and COMSOL model (orange line).

either end of the stack, while the middle cells have little loss. Again, it is found that the length of the inlet significantly affects the leakage current (orange and blue curves) because the leakage current for the outer cells is decreased by almost a factor of two when the length of the inlet becomes three times as long. These results also show that the extra inlet resistance leads to a more linear loss over the cells and, therefore, a smaller performance difference between the cells. As described in chapter 2, the maximum hydrogen production per cell depends on the current of that cell and a higher current leads to a higher efficiency. Therefore, it is favourable if all cells have a more equal current rather than a high current on the end cells and a lower current in the middle of the stack.

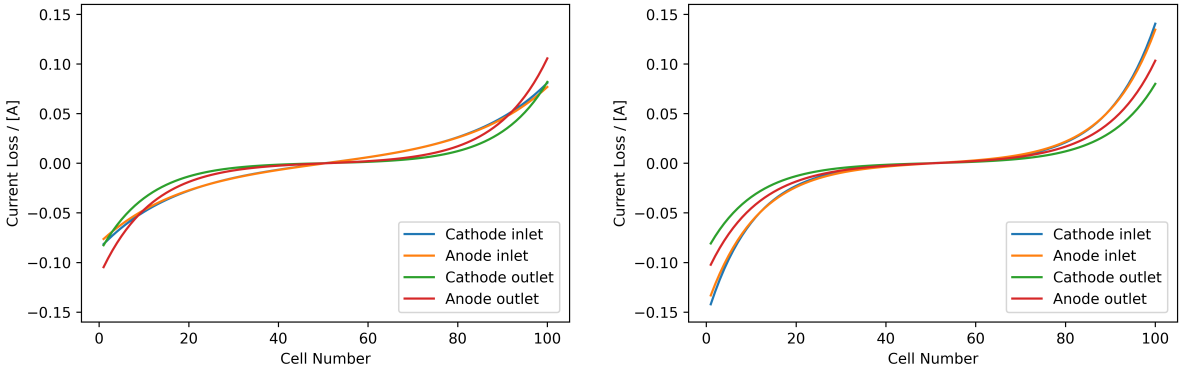

(a) (b)

Figure 4.15: Leakage current per cell for each of the two inlets and two outlets in 100 cells. Modelled as EEC in Python for 100 cells with long inlets (a) and short inlets (b).

The same results as found for 100 cells in the EEC model can be produced in COMSOL, of which the results are in figure 4.16. However, there are some issues with the solver of this model. The polarisation curve was fitted for a low number of cells, which showed a good

Table 4.5: Deviation of faradaic efficiency of EEC and COMSOL model from experimental data. The deviation is calculated at 26, 91, and 148 mA/cm² for the geometry using long zigzag inlets and short inlets.

Long inlets			
Current density (mA/cm^2)	Model	Faradaic efficiency (-)	Deviation from experiment (%)
26	Exp	0.8910	-
	COMSOL	0.9445	6.0
	EEC	0.9828	10
91	Exp	0.9575	-
	COMSOL	0.9807	2.4
	EEC	0.9941	3.8
148	Exp	0.9712	-
	COMSOL	0.9875	1.7
	EEC	0.9959	2.6
Short inlets			
Current density (mA/cm^2)	Model	Faradaic efficiency (-)	Deviation from experiment (%)
26	Exp	0.8587	-
	COMSOL	0.8748	1.9
	EEC	0.9725	13
91	Exp	0.9584	-
	COMSOL	0.9603	0.20
	EEC	0.9906	3.4
148	Exp	0.9615	-
	COMSOL	0.9743	1.3
	EEC	0.9934	3.3

Table 4.6: Relations used in EEC vs COMSOL model.

	COMSOL	EEC
θ (bubbling rate)	-	from Vogt [79]: $\theta = (-97.25 + 182 \cdot \frac{T}{T_{ref}} - 84 * (\frac{T}{T_{ref}})^2) * (\frac{I}{30 * Area})^{0.3}$
ϵ (gas fraction at top)	initial guess: 0.30 for cathode 0.15 for anode	$4/3 \cdot \theta$ for cathode $2/3 \cdot \theta$ for anode
reduced conductivity due to gas fraction	Bruggeman: $K_\epsilon/K_0 = (1-\epsilon)^{1.5}$	Maxwell: $K_\epsilon/K_0 = \frac{1-\epsilon}{1+0.5\epsilon}$

fit. When the number of cells was increased, the start of the polarisation curve at 1.21V was not found at currents close to 0 anymore but shifted to higher currents. This offset on the x-axis became larger for higher currents. If the leakage currents are calculated at the same current as before (143mA/cm^2), this corresponds to only 1.5V in the new polarisation curve, which flattens the leakage current curve. If the leakage currents are calculated at the previous corresponding 2.1V, then the magnitude of the leakage currents increases significantly since this now corresponds to an inlet current of 297mA/cm^2. The leakage current for the first cell then starts at -0.46A instead of -0.37A.

Due to the problem above, this COMSOL model is not quantitatively compared to the EEC model but is used to validate its conclusions. Using the results from figure 4.16, it is again found that the inlet length has a large effect on the leakage current via those channels. It is also found that the loss via those inlet channels is more linear than the loss via the outlets, resulting in a more constant current throughout the electrolysis stack.

When comparing the predicted cell current using the EEC model to Jupudi's work [20],

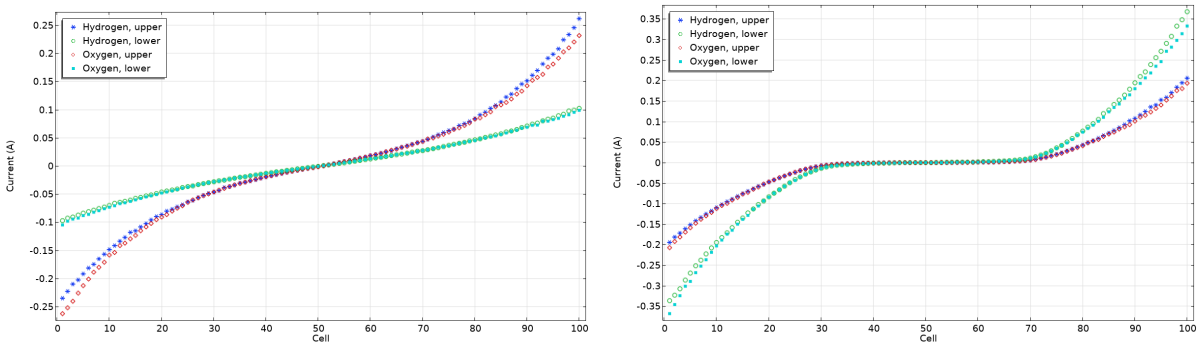

(a) (b)

Figure 4.16: Leakage current per cell for each of the two inlets and two outlets in 100 cells. Modelled in COMSOL for 100 cells with long inlets (a) and short inlets (b).

it is concluded that the EEC model is more adaptable and more physically representative. Figure 4.17 shows the cell current plotted per cell for various currents, using the EEC model (a) and Jupudi's model (b). It can be seen that the losses calculated in Jupudi's model are not dependent on the inlet current, while this is predicted by the EEC model. Based on literature and the experiments, those results are unlikely to be accurate. In the EEC model, the leakage currents do become less for lower inlet currents, which is as expected.

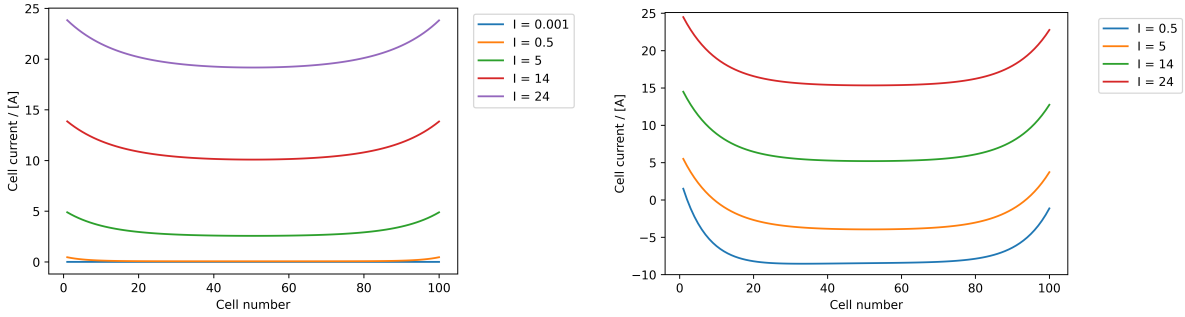

(a) (b)

Figure 4.17: Cell current throughout the stack. Modelled for 100 cells using EEC model (a) and Jupudi's model (b) at different inlet currents.

4.3.3. Effect of Cells on Efficiency

The effect of the number of cells on the Faraday efficiency was also researched. It is expected that the decrease in Faraday efficiency becomes smaller when the number of cells increases [20]. For example, increasing the number of cells in the stack from 10 to 20 will negatively impact the Faraday efficiency more than when it is increased from 100 to 200 cells. Ultimately, the number of cells will hardly affect the amount of shunt current and, therefore, the efficiency. For the EEC model, the Faraday efficiency was determined at 19, 54, 103 and 153mA/cm^2 for a cell number ranging from 8 to 200, of which the results are shown in figure 4.18. In this figure, the loss (equal to $1 - \eta_F$) is plotted versus the number of cells at different inlet current densities. This plot shows indeed that for a higher number of cells, the amount of leakage current is less affected.

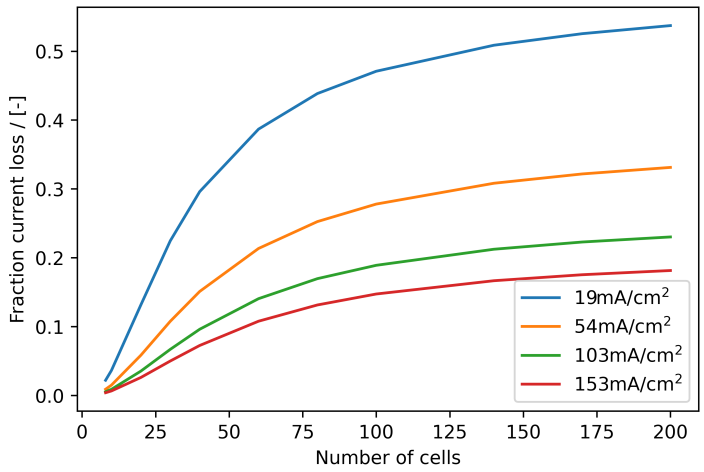

Figure 4.18: Fraction of current loss vs number of cells for 19, 54, 103 and 153mA/cm^2 in EEC model.

5

Conclusions and recommendations

In this last chapter, the main findings of this thesis are summarised to draw the most important conclusions. Furthermore, various points of attention and weaknesses were found during the research to further explore the effects of leakage currents. These are described in the recommendations.

5.1. Conclusion

In the introduction, it was stated the rapid increase in renewable energy utilisation leads to a lot of challenges. While solar and wind energy already provide a growing part of the energy, its intermittent nature calls for some buffer. Since the research into electrolysis has grown exponentially over the past couple of years, it is interesting to couple the buffering capability of hydrogen with intermittent renewable energy sources.

To achieve this stadium, first, some challenges in alkaline water electrolysis need to be overcome. This thesis focused on researching and reducing the leakage currents in the stack to increase the efficiency and safety of the electrolysis system. Based on the literature research, it was found that a research gap exists in modelling the leakage currents in three-dimensional models using physical data since the electrolysis process is only widely covered by empirical relations. Therefore, the main research question was formulated as follows:

Can a three-dimensional model of an electrolyser help to predict leakage currents?

And the following subquestions were set to help answer the main research question:

1. Can a 3D electrolyser be accurately modelled in COMSOL Multiphysics?
2. Can a 3D electrolyser be accurately modelled using an equivalent electrical circuit (EEC)?
3. What is the influence of design choices on the leakage currents?

5.1.1. COMSOL Model

The COMSOL model was built using electrochemical relations and physical behaviour in an alkaline water electrolyser. Using this software, the polarisation curve and faradaic efficiency could be found, as well as the shunt current per cell. This software was used to build a model mimicking the experiments as closely as possible. Firstly, the geometry was rebuilt in 2D and 3D and the parameters for inlet conditions, the electrolyte and materials were set. In this software, the difference in results for a bipolar or monopolar configuration was very minimal, while the bipolar electrodes took less computing power, so bipolar electrodes were used.

In 2D, it was found that the COMSOL model was able to result in a polarisation curve very close to the one found in experiments, with a fitted porosity of 50%, a cathodic exchange current density of 3.0A/m^2, and an anodic exchange current density of 1.3A/m^2. This was within the limits found in literature since the porosity could be 30-50%, and the exchange current densities could be between 10^{-6}-10^{2}A/m^2. In the 3D model for an electrolysis stack of eight cells, the polarisation curve could be fitted well for current densities larger than 30mA/cm^2 up to 160mA/cm^2. As fitting parameters, a porosity of 50% was used, as well as a cathodic exchange current density of 6.0A/m^2 and an anodic exchange current density of 1.4A/m^2. For lower current densities, the model underestimated the voltage for the given current. The COMSOL model gave very similar values for the Faraday efficiency compared to the experiments, with an error of below 2.5%. For the short inlets, the COMSOL model predicted values mostly within the error margin of the experimental data, with a maximum deviation of 1.5%. The rapidly increasing slope for low currents up to the almost constant efficiency at higher currents was replicated very closely in the model. For longer zigzag-shaped inlets, the results from the model were still very close to the experimental data but predicted a little higher values. For this model, it was unclear what exactly the effect of the zigzag-shaped inlet channels was since these were modelled as a straight line. Overall, the performance of this model is very good.

5.1.2. EEC Model

An in-house model using the same electrochemical relations as COMSOL was used to fit exchange current densities and validate the found parameters. In this model, again, a porosity of 50% was found to give the best fit, but the exchange current densities were found to be 0.25A/m^2 for the cathodic compartment and 0.05A/m^2 for the anodic compartment. This is 12 (cathode) and 26 (anode) times smaller than the values found in COMSOL. This could have several reasons, with the first one being that the COMSOL model overpredicts the exchange current densities since the transfer coefficients were set to be larger than those found in other research. Furthermore, parts of the overpotential that have not yet been corrected for are taken into the exchange current density to fit the experimental data. Since the models are not the same and do not have entirely matching input parameters, it could very well be that these overpotentials need different correction factors, which are represented in the exchange current density. Therefore, it was concluded that this 2D validation mainly shows that the exchange current densities are fitting parameters and do not necessarily match between models while still corresponding to the same experimental data.

The 3D EEC model was built by mimicking the electrolyser stack as an electrical circuit. It consisted of resistances for the inlets, outlets, manifolds and multiple resistances in the cell. The values for these resistances are calculated using relations from other research. The resistances were corrected for bubble formation, impacting both the cell and outlet resistance. The polarisation curve was fitted with exchange current densities of 0.064A/m^2 and 0.019A/m^2 for the cathodic and anodic sides, respectively. In this model, it is found that the polarisation approaches 1.21V when the current density approaches 0mA/cm^2, which is as expected since this is the minimum voltage for the electrolysis reactions to take place. The EEC model also underestimates the voltage for low currents, albeit less than the COMSOL model. This EEC model can predict the linear behaviour of the polarisation curve for higher currents quite well and fits well at higher currents. The results of this model also show that, regardless of the input current, the model consistently overestimates the Faraday efficiency, corresponding to around 3-4% for higher current densities. To improve this, the resistance of the inlets and outlets needs to be reduced drastically by around 50% to fit the experimental data. Overall, the results of this model showed an overestimation of the performance found in the experiments.

5.1.3. Prediction

In this part, both the COMSOL model and the EEC model were used to simulate new scenarios and find the effects on the electrolyser performance. It was found that the solver used in COMSOL gave an unwanted shift in the polarisation curve, which resulted in inaccurate results. Therefore, both models were used only to compare different scenarios and could not provide definite numbers.

Both models showed that a lengthened inlet resulted in a large decrease in leakage currents via those channels of about 80%. When this difference was extrapolated to 100 cells, it was found that the longer inlet also led to fewer leakage currents. Moreover, while the normal leakage current curve has an S-shape with the highest losses in the outer cells, the lengthened inlets resulted in a more linear curve. This linear curve will lead to a more evenly spread performance over all cells. The S-shaped curve was found in both the COMSOL and EEC models and was present irrespective of the inlet current. For lower inlet current, the middle part of the S-curve flattened, but the outer cells kept the exponential-shaped curve.

Furthermore, when comparing the results of the EEC model to the work of Jupudi [20], who also modelled the electrolyser stack as an equivalent electrical circuit, the EEC model showed a better performance. No negative currents were observed for low current densities, which was a problem in Jupudi's work. Therefore, the EEC model is better suited to predict various scenarios.

Lastly, it was found that for a constant set of parameters, the Faraday efficiency decreased towards an asymptotic value when the number of cells was increased. The efficiency decreased rapidly for a few cells, but this effect became smaller for up to 200 cells.

5.2. Recommendations

Starting with the experimental data, it would greatly improve the reliability of the models if the experiments were performed using more cells, for instance, 32 or over 60 cells. The results of the experiments showed signs of constant loss and inconsistent data, and when more cells are used, this error might be easier to define or reduce. Another recommendation is to implement experimental methods to measure current in the manifolds instead of hydrogen production directly. This removes the uncertainty from leakage problems in the measurements. The results could be directly compared to any of the two models, which could be validated more accurately.

The COMSOL model showed promising results but also had several weaknesses. It is inherently a black box model, and therefore, several input parameters could not be changed. For example, the water electrolyzer module required voltage as an input source and calculated the corresponding current, while in reality, this is the other way around. More modelling is needed to optimise this model and further validate its results. Also, to better model the effect of bubble formation and its results on resistances, making a transient model rather than a steady-state model is recommended. When the flow is modelled more accurately, it is expected that the flows throughout different cells change, and it is recommended to research how this affects the leakage currents.

The EEC model has the advantage that all input and calculations are clearly defined and can easily be changed. For further research, it is recommended that more experimental data is gathered to better fit the model to the data, especially for the Faraday efficiency. Since this model is so adaptable, it would be beneficial to optimise it and quantitatively define the effect of changes in geometry, inlet conditions or operating conditions. Since both the pressure and temperature are defined via relations in the model, the performance and amount of bypass current can be determined for different operating conditions, and aid in optimising the system.

Bibliography

[1] Johnston, Brenda ; Mayo, Michael C. ; Khare, Anshuman: Hydrogen: the energy source for the 21st century. In: *Technovation* 25 (2005), 6, Nr. 6, S. 569–585. http://dx.doi.org/10.1016/j.technovation.2003.11.005. – DOI 10.1016/j.technovation.2003.11.005. – ISSN 01664972

[2] UNFCCC: *The Paris Agreement*. https://unfccc.int/process-and-meetings/the-paris-agreement. Version: 2021

[3] IEA: The Netherlands 2020 - Energy Policy Review / IEA. Version: 9 2020. https://www.iea.org/reports/the-netherlands-2020. 2020. – Forschungsbericht

[4] Amirante, Riccardo ; Cassone, Egidio ; Distaso, Elia ; Tamburrano, Paolo: Overview on recent developments in energy storage: Mechanical, electrochemical and hydrogen technologies. In: *Energy Conversion and Management* 132 (2017), 1, S. 372–387. http://dx.doi.org/10.1016/j.enconman.2016.11.046. – DOI 10.1016/j.enconman.2016.11.046. – ISSN 01968904

[5] EERE Energy Efficicency & Renewable Energy: *Hydrogen Production: Electrolysis*. https://www.energy.gov/eere/fuelcells/hydrogen-production-electrolysis

[6] Brauns, Jörn ; Turek, Thomas: Alkaline Water Electrolysis Powered by Renewable Energy: A Review. In: *Processes* 8 (2020), 2, Nr. 2, S. 248. http://dx.doi.org/10.3390/pr8020248. – DOI 10.3390/pr8020248. – ISSN 2227–9717

[7] Wang, Mingyong ; Wang, Zhi ; Gong, Xuzhong ; Guo, Zhancheng: The intensification technologies to water electrolysis for hydrogen production – A review. In: *Renewable and Sustainable Energy Reviews* 29 (2014), 1, S. 573–588. http://dx.doi.org/10.1016/j.rser.2013.08.090. – DOI 10.1016/j.rser.2013.08.090. – ISSN 13640321

[8] IRENA International Renewable Energy Agency: Global Renewables Outlook: Energy Transformation 2050 / IRENA. Version: 2020. https://www.irena.org/-/media/Files/IRENA/Agency/Publication/2020/Apr/IRENA_GRO_Summary_2020.pdf?la=en&hash=1F18E445B56228AF8C4893CAEF147ED0163A0E47. 2020. – Forschungsbericht

[9] Gigler, J. ; Weeda, M.: Routekaart Waterstof / TKI Nieuw Gas. Utrecht, 3 2018. – Forschungsbericht

[10] Kellner, Marijke ; Martens, Rob ; Afman, Maarten: Transition of the Dutch energy system: scenario's 2030-2050 / Netbeheer Nederland. Version: 4 2023. https://www.netbeheernederland.nl/_upload/Files/Management_summary_Transition_of_the_Dutch_energy_system__scenario_s_2030-2050_272.pdf. Den Haag, 4 2023. – Forschungsbericht

[11] Netherlands Enterprise Agency (RVO): Excelling in Hydrogen: Dutch technology for a climate-neutral world / RVO, FME, and TKI New Gas (Topsector Energy).

Version: 4 2022. https://www.rvo.nl/sites/default/files/2022-05/NL-Dutch-solutions-for-a-hydrogen-economy-V-April-2022-DIGI.pdf. Utrecht, 4 2022. – Forschungsbericht

[12] Wijk, A. van: The Green Hydrogen Economy / Northern Netherlands Innovation Board. Groningen, 4 2017. – Forschungsbericht

[13] Renssen, Sonja van: The hydrogen solution? In: *Nature Climate Change* 10 (2020), 9, Nr. 9, S. 799–801. http://dx.doi.org/10.1038/s41558-020-0891-0. – DOI 10.1038/s41558–020–0891–0. – ISSN 1758–678X

[14] Ursua, Alfredo ; Gandia, Luis M. ; Sanchis, Pablo: Hydrogen Production From Water Electrolysis: Current Status and Future Trends. In: *Proceedings of the IEEE* 100 (2012), 2, Nr. 2, S. 410–426. http://dx.doi.org/10.1109/JPROC.2011.2156750. – DOI 10.1109/JPROC.2011.2156750. – ISSN 0018–9219

[15] Nowotny, Janusz ; Veziroglu, T. N.: Impact of hydrogen on the environment. In: *International Journal of Hydrogen Energy* 36 (2011), 10, Nr. 20, S. 13218–13224. http://dx.doi.org/10.1016/j.ijhydene.2011.07.071. – DOI 10.1016/j.ijhydene.2011.07.071. – ISSN 03603199

[16] Straits Research: Water Electrolysis Market / Straits Research. Version: 2022. https://straitsresearch.com/report/water-electrolysis-market. 2022. – Forschungsbericht

[17] Precedence Research: Electrolyzer Market / Precedence Research. Version: 2023. https://www.precedenceresearch.com/electrolyzer-market. Ottawa, Canada, 2023. – Forschungsbericht

[18] Pasimeni, Francesco ; Sezer, Ufuk ; Boshell, Francisco ; Boedt, Geert: Innovation Trends in Electrolysers for Hydrogen Production / EPO and IRENA. Vienna, 2022. – Forschungsbericht

[19] Ursúa, Alfredo ; Marroyo, Luis ; Gubía, Eugenio ; Gandía, Luis M. ; Diéguez, Pedro M. ; Sanchis, Pablo: Influence of the power supply on the energy efficiency of an alkaline water electrolyser. In: *International Journal of Hydrogen Energy* 34 (2009), 5, Nr. 8, S. 3221–3233. http://dx.doi.org/10.1016/j.ijhydene.2009.02.017. – DOI 10.1016/j.ijhydene.2009.02.017. – ISSN 03603199

[20] Jupudi, Ravichandra S. ; Zappi, Guillermo ; Bourgeois, Richard: Prediction of shunt currents in a bipolar electrolyzer stack by difference calculus. In: *Journal of Applied Electrochemistry* 37 (2007), 8, Nr. 8, S. 921–931. http://dx.doi.org/10.1007/s10800-007-9330-4. – DOI 10.1007/s10800–007–9330–4. – ISSN 0021–891X

[21] Guillet, Nicolas ; Millet, Pierre: Alkaline Water Electrolysis. Version: 2 2015. http://dx.doi.org/10.1002/9783527676507.ch4. In: *Hydrogen Production*. Weinheim, Germany : Wiley-VCH Verlag GmbH & Co. KGaA, 2 2015. – DOI 10.1002/9783527676507.ch4, S. 117–166

[22] Zeng, Kai ; Zhang, Dongke: Recent progress in alkaline water electrolysis for hydrogen production and applications. In: *Progress in Energy and Combustion Science* 36 (2010), 6, Nr. 3, S. 307–326. http://dx.doi.org/10.1016/j.pecs.2009.11.002. – DOI 10.1016/j.pecs.2009.11.002. – ISSN 03601285

[23] *XINTC electrolysers*. xintc.global. Version: 2023

[24] Buttler, Alexander ; Spliethoff, Hartmut: Current status of water electrolysis for energy storage, grid balancing and sector coupling via power-to-gas and power-to-liquids: A review. In: *Renewable and Sustainable Energy Reviews* 82 (2018), 2, S. 2440–2454. http://dx.doi.org/10.1016/j.rser.2017.09.003. – DOI 10.1016/j.rser.2017.09.003. – ISSN 13640321

[25] Sánchez, Mónica ; Amores, Ernesto ; Abad, David ; Rodríguez, Lourdes ; Clemente-Jul, Carmen: Aspen Plus model of an alkaline electrolysis system for hydrogen production. In: *International Journal of Hydrogen Energy* 45 (2020), 2, Nr. 7, S. 3916–3929. http://dx.doi.org/10.1016/j.ijhydene.2019.12.027. – DOI 10.1016/j.ijhydene.2019.12.027. – ISSN 03603199

[26] Ni, M ; Leung, M ; Leung, D: Technological development of hydrogen production by solid oxide electrolyzer cell (SOEC). In: *International Journal of Hydrogen Energy* 33 (2008), 5, Nr. 9, S. 2337–2354. http://dx.doi.org/10.1016/j.ijhydene.2008.02.048. – DOI 10.1016/j.ijhydene.2008.02.048. – ISSN 03603199

[27] David, Martín ; Ocampo-Martínez, Carlos ; Sánchez-Peña, Ricardo: Advances in alkaline water electrolyzers: A review. In: *Journal of Energy Storage* 23 (2019), 6, S. 392–403. http://dx.doi.org/10.1016/j.est.2019.03.001. – DOI 10.1016/j.est.2019.03.001. – ISSN 2352152X

[28] Guo, Yujing ; Li, Gendi ; Zhou, Junbo ; Liu, Yong: Comparison between hydrogen production by alkaline water electrolysis and hydrogen production by PEM electrolysis. In: *IOP Conference Series: Earth and Environmental Science* 371 (2019), 12, Nr. 4, S. 042022. http://dx.doi.org/10.1088/1755-1315/371/4/042022. – DOI 10.1088/1755–1315/371/4/042022. – ISSN 1755–1307

[29] Vermeiren, Ph. ; Adriansens, W. ; Leysen, R.: Zirfon: A new separator for Ni-H2 batteries and alkaline fuel cells. In: *International Journal of Hydrogen Energy* 21 (1996), 8, Nr. 8, S. 679–684. http://dx.doi.org/10.1016/0360-3199(95)00132-8. – DOI 10.1016/0360–3199(95)00132–8. – ISSN 03603199

[30] Vermeiren, Ph. ; Moreels, J. P. ; Leysen, R.: Porosity in composite zirfon□ membranes. In: *Journal of Porous Materials* 3 (1996), Nr. 1, S. 33–40. http://dx.doi.org/10.1007/BF01135359. – DOI 10.1007/BF01135359. – ISSN 1380–2224

[31] Kotowicz, Janusz ; Jurczyk, Michał ; Wecel, Daniel ; Ogulewicz, Włodzimierz: Analysis of hydrogen production in alkaline electrolyzers. In: *Journal of Power Technologies* 96 (2016), Nr. 3, S. 149. – ISSN 2083–4187

[32] Mamoon Rashid, Md ; Al Mesfer, M. K. ; Naseem, H. ; Danish, M.: Hydrogen Production by Water Electrolysis: A Review of Alkaline Water Electrolysis, PEM Water Electrolysis and High Temperature Water Electrolysis. In: *International Journal of Engineering and Advanced Technology* 4 (2015), 2, Nr. 3, S. 80–93

[33] Perry, Samuel C. ; León, Carlos Ponce d. ; Walsh, Frank C.: Review—The Design, Performance and Continuing Development of Electrochemical Reactors for Clean Electrosynthesis. In: *Journal of The Electrochemical Society* 167 (2020), 12, Nr. 15, S. 155525. http://dx.doi.org/10.1149/1945-7111/abc58e. – DOI 10.1149/1945–7111/abc58e. – ISSN 0013–4651

[34] Santos, Diogo M. F. ; Sequeira, César A. C. ; Figueiredo, José L.: Hydrogen production by alkaline water electrolysis. In: *Química Nova* 36 (2013), Nr. 8, S. 1176–1193. http://dx.doi.org/10.1590/S0100-40422013000800017. – DOI 10.1590/S0100–40422013000800017. – ISSN 0100–4042

[35] Bessarabov, Dmitri ; Millet, Pierre: Fundamentals of Water Electrolysis. Version: 2018. http://dx.doi.org/10.1016/B978-0-12-811145-1.00003-4. In: *PEM Water Electrolysis*. Elsevier, 2018. – DOI 10.1016/B978–0–12–811145–1.00003–4, S. 43–73

[36] Hammoudi, M. ; Henao, C. ; Agbossou, K. ; Dubé, Y. ; Doumbia, M.L.: New multi-physics approach for modelling and design of alkaline electrolyzers. In: *International Journal of Hydrogen Energy* 37 (2012), 10, Nr. 19, S. 13895–13913. http://dx.doi.org/10.1016/j.ijhydene.2012.07.015. – DOI 10.1016/j.ijhydene.2012.07.015. – ISSN 03603199

[37] Olivier, Pierre ; Bourasseau, Cyril ; Bouamama, Pr. B.: Low-temperature electrolysis system modelling: A review. In: *Renewable and Sustainable Energy Reviews* 78 (2017), 10, S. 280–300. http://dx.doi.org/10.1016/j.rser.2017.03.099. – DOI 10.1016/j.rser.2017.03.099. – ISSN 13640321

[38] Ulleberg, O: Modeling of advanced alkaline electrolyzers: a system simulation approach. In: *International Journal of Hydrogen Energy* 28 (2003), 1, Nr. 1, S. 21–33. http://dx.doi.org/10.1016/S0360-3199(02)00033-2. – DOI 10.1016/S0360–3199(02)00033–2. – ISSN 03603199

[39] Leroy, R: Industrial water electrolysis: Present and future. In: *International Journal of Hydrogen Energy* 8 (1983), Nr. 6, S. 401–417. http://dx.doi.org/10.1016/0360-3199(83)90162-3. – DOI 10.1016/0360–3199(83)90162–3. – ISSN 03603199

[40] Henao, Christian ; Agbossou, Kodjo ; Hammoudi, Mhamed ; Dubé, Yves ; Cardenas, Alben: Simulation tool based on a physics model and an electrical analogy for an alkaline electrolyser. In: *Journal of Power Sources* 250 (2014), 3, S. 58–67. http://dx.doi.org/10.1016/j.jpowsour.2013.10.086. – DOI 10.1016/j.jpowsour.2013.10.086. – ISSN 03787753

[41] Noren, D.A. ; Hoffman, M.A.: Clarifying the Butler–Volmer equation and related approximations for calculating activation losses in solid oxide fuel cell models. In: *Journal of Power Sources* 152 (2005), 12, S. 175–181. http://dx.doi.org/10.1016/j.jpowsour.2005.03.174. – DOI 10.1016/j.jpowsour.2005.03.174. – ISSN 03787753

[42] Lamy, Claude ; Millet, Pierre: A critical review on the definitions used to calculate the energy efficiency coefficients of water electrolysis cells working under near ambient temperature conditions. In: *Journal of Power Sources* 447 (2020), 1, S. 227350. http://dx.doi.org/10.1016/j.jpowsour.2019.227350. – DOI 10.1016/j.jpowsour.2019.227350. – ISSN 03787753

[43] Nagai, N: Existence of optimum space between electrodes on hydrogen production by water electrolysis. In: *International Journal of Hydrogen Energy* 28 (2003), 1, Nr. 1, S. 35–41. http://dx.doi.org/10.1016/S0360-3199(02)00027-7. – DOI 10.1016/S0360–3199(02)00027–7. – ISSN 03603199

[44] Sakas, Georgios ; Ibáñez-Rioja, Alejandro ; Ruuskanen, Vesa ; Kosonen, Antti ; Ahola, Jero ; Bergmann, Olli: Dynamic energy and mass balance model for an industrial alkaline

water electrolyzer plant process. In: *International Journal of Hydrogen Energy* 47 (2022), 1, Nr. 7, S. 4328–4345. http://dx.doi.org/10.1016/j.ijhydene.2021.11.126. – DOI 10.1016/j.ijhydene.2021.11.126. – ISSN 03603199

[45] Abe, Isao: Alkaline Water Electrolysis. In: *Energy Carriers and Conversion Systems* Bd. 1. Chiba, Japan : Encyclopedia of Life Support System (EOLSS), 2009, S. 146–166

[46] De Silva, Y. Sanath K. ; Middleton, Peter H. ; Kolhe, Mohan L.: Performance comparison of mono-polar and bi-polar configurations of alkaline electrolysis stack through 3-D modelling and experimental fabrication. In: *Renewable Energy* 149 (2020), 4, S. 760–772. http://dx.doi.org/10.1016/j.renene.2019.12.087. – DOI 10.1016/j.renene.2019.12.087. – ISSN 09601481

[47] Amores, Ernesto ; Rodríguez, Jesús ; Carreras, Christian: Influence of operation parameters in the modeling of alkaline water electrolyzers for hydrogen production. In: *International Journal of Hydrogen Energy* 39 (2014), 8, Nr. 25, S. 13063–13078. http://dx.doi.org/10.1016/j.ijhydene.2014.07.001. – DOI 10.1016/j.ijhydene.2014.07.001. – ISSN 03603199

[48] Eigeldinger, John ; Vogt, Helmut: The bubble coverage of gas-evolving electrodes in a flowing electrolyte. In: *Electrochimica Acta* 45 (2000), Nr. 27, S. 4449–4456. – ISSN 0013–4686

[49] Kuhn, A. T. ; Booth, J. S.: Electrical leakage currents in bipolar cell stacks. In: *Journal of Applied Electrochemistry* 10 (1980), 3, Nr. 2, S. 233–237. http://dx.doi.org/10.1007/BF00726091. – DOI 10.1007/BF00726091. – ISSN 0021–891X

[50] White, R. E. ; Walton, C. W. ; Burney, H. S. ; Beaver, R. N.: Predicting Shunt Currents in Stacks of Bipolar Plate Cells. In: *Journal of The Electrochemical Society* 133 (1986), 3, Nr. 3, S. 485–492. http://dx.doi.org/10.1149/1.2108606. – DOI 10.1149/1.2108606. – ISSN 0013–4651

[51] Dousek, F.P. ; Micka, K.: Advanced laboratory electrolyser for production of pure hydrogen. In: *Journal of Applied Electrochemistry* 23 (1993), 3, Nr. 3. http://dx.doi.org/10.1007/BF00241915. – DOI 10.1007/BF00241915. – ISSN 0021–891X

[52] Yang, Min-Zhi ; Wu, Han ; Selman, J. R.: A model for bipolar current leakage in cell stacks with separate electrolyte loops. In: *Journal of Applied Electrochemistry* 19 (1989), 3, Nr. 2, S. 247–254. http://dx.doi.org/10.1007/BF01062308. – DOI 10.1007/BF01062308. – ISSN 0021–891X

[53] Comninellis, Ch. ; Plattner, E. ; Bolomey, P.: Estimation of current bypass in a bipolar electrode stack from current-potential curves. In: *Journal of Applied Electrochemistry* 21 (1991), 5, Nr. 5, S. 415–418. http://dx.doi.org/10.1007/BF01024577. – DOI 10.1007/BF01024577. – ISSN 0021–891X

[54] Bonvin, G. ; Comninellis, Ch.: Scale-up of bipolar electrode stack dimensionless numbers for current bypass estimation. In: *Journal of Applied Electrochemistry* 24 (1994), 6, Nr. 6, S. 469–474. http://dx.doi.org/10.1007/BF00249844. – DOI 10.1007/BF00249844. – ISSN 0021–891X

[55] Colli, A. N. ; Girault, H. H.: Compact and General Strategy for Solving Current and Potential Distribution in Electrochemical Cells Composed of Massive Monopolar and Bipolar Electrodes. In: *Journal of The Electrochemical Society* 164 (2017),

Nr. 11, S. E3465–E3472. http://dx.doi.org/10.1149/2.0471711jes. – DOI 10.1149/2.0471711jes. – ISSN 0013–4651

[56] Doležel, M. ; Keslerová, K.: Measurement of Non-Effective Electric Current in Electrodialysis Stacks. In: *Journal of The Electrochemical Society* 164 (2017), 7, Nr. 9, S. E276–E282. http://dx.doi.org/10.1149/2.1481709jes. – DOI 10.1149/2.1481709jes. – ISSN 0013–4651

[57] Grimes, Patrick G.: *Shunt current elimination for series connected cells*. 3 1983

[58] Bellows, Richard J. ; Grimes, Patrick G.: *Electrochemical device having means for reducing shunt current*. 7 1984

[59] *Elektrochemische inrichting en werkwijze voor het daarin tot een minimum beperken van shunt-stromen*. 1 1994

[60] Paul, Clayton R.: *Fundamentals of Electrical Circuit Analysis*. 1. John Wiley & Sons, 2001

[61] Kreutzer, Michiel T. ; Kapteijn, Freek ; Moulijn, Jacob A. ; Kleijn, Chris R. ; Heiszwolf, Johan J.: Inertial and interfacial effects on pressure drop of Taylor flow in capillaries. In: *AIChE Journal* 51 (2005), 9, Nr. 9, S. 2428–2440. http://dx.doi.org/10.1002/aic.10495. – DOI 10.1002/aic.10495. – ISSN 0001–1541

[62] Mokhatab, Saeid ; Poe, William A. ; Mak, John Y.: Chapter 2 - Raw Gas Transmission. Version: 2015. http://dx.doi.org/https://doi.org/10.1016/B978-0-12-801499-8.00002-X. In: Mokhatab, Saeid (Hrsg.) ; Poe, William A. (Hrsg.) ; Mak, John Y. (Hrsg.): *Handbook of Natural Gas Transmission and Processing (Third Edition)*. Boston : Gulf Professional Publishing, 2015. – DOI https://doi.org/10.1016/B978–0–12–801499–8.00002–X. – ISBN 978–0–12–801499–8, 37–121

[63] Gupta, R. ; Fletcher, D.F. ; Haynes, B.S.: Taylor Flow in Microchannels: A Review of Experimental and Computational Work. In: *The Journal of Computational Multiphase Flows* 2 (2010), 3, Nr. 1, S. 1–31. http://dx.doi.org/10.1260/1757-482X.2.1.1. – DOI 10.1260/1757–482X.2.1.1. – ISSN 1757–482X

[64] Angeli, Panagiota ; Gavriilidis, Asterios: Taylor Flow in Microchannels. http://dx.doi.org/10.1007/978-0-387-48998-8{_}1526. In: *Encyclopedia of Microfluidics and Nanofluidics*. Boston, MA : Springer US. – DOI 10.1007/978–0–387–48998–8_1526, S. 1971–1976

[65] Angeli, P ; Gavriilidis, A: Hydrodynamics of Taylor flow in small channels: A Review. In: *Proceedings of the Institution of Mechanical Engineers, Part C: Journal of Mechanical Engineering Science* 222 (2008), 5, Nr. 5, S. 737–751. http://dx.doi.org/10.1243/09544062JMES776. – DOI 10.1243/09544062JMES776. – ISSN 0954–4062

[66] Green, Don W. ; Southard, Marylee Z. ; Green, Don W. (Hrsg.) ; Southard, Marylee Z. (Hrsg.): *Perry's Chemical Engineers' Handbook*. 9th Edition. New York : McGraw-Hill Education, 2018. – ISBN 9780071834087

[67] Miller, Donald S.: *Internal Flow Systems*. BHRA Fluid Engineering, 1978

[68] Mykrolis: *Tylan FC260/FM360 Mass Flow Controllers and Flowmeters*

[69] log-korea.com: *Tylan FC-280SA/FM-380SA Mass Flow Controllers and Flowmeters*

[70] COMSOL: *Shunt Currents in an Alkaline Electrolyzer Stack*. https://www.comsol.com/model/shunt-currents-in-an-alkaline-electrolyzer-stack-113041. Version: 2022

[71] Abdin, Z. ; Webb, C.J. ; Gray, E.MacA.: Modelling and simulation of an alkaline electrolyser cell. In: *Energy* 138 (2017), 11, S. 316–331. http://dx.doi.org/10.1016/j.energy.2017.07.053. – DOI 10.1016/j.energy.2017.07.053. – ISSN 03605442

[72] Wendt, H. ; Plzak, V.: Electrocatalytic and thermal activation of anodic oxygen- and cathodic hydrogen-evolution in alkaline water electrolysis. In: *Electrochimica Acta* 28 (1983), 1, Nr. 1, S. 27–34. http://dx.doi.org/10.1016/0013-4686(83)85083-X. – DOI 10.1016/0013–4686(83)85083–X. – ISSN 00134686

[73] Hu, Kewei ; Fang, Jiakun ; Ai, Xiaomeng ; Huang, Danji ; Zhong, Zhiyao ; Yang, Xiaobo ; Wang, Lei: Comparative study of alkaline water electrolysis, proton exchange membrane water electrolysis and solid oxide electrolysis through multiphysics modeling. In: *Applied Energy* 312 (2022), 4, S. 118788. http://dx.doi.org/10.1016/j.apenergy.2022.118788. – DOI 10.1016/j.apenergy.2022.118788. – ISSN 03062619

[74] Navarro-Flores, Elisa ; Chong, Zhiwen ; Omanovic, Sasha: Characterization of Ni, NiMo, NiW and NiFe electroactive coatings as electrocatalysts for hydrogen evolution in an acidic medium. In: *Journal of Molecular Catalysis A: Chemical* 226 (2005), 2, Nr. 2, S. 179–197. http://dx.doi.org/10.1016/j.molcata.2004.10.029. – DOI 10.1016/j.molcata.2004.10.029. – ISSN 13811169

[75] Yang, Timothy T. ; Patil, Rituja B. ; McKone, James R. ; Saidi, Wissam A.: Revisiting trends in the exchange current for hydrogen evolution. In: *Catalysis Science & Technology* 11 (2021), Nr. 20, S. 6832–6838. http://dx.doi.org/10.1039/D1CY01170G. – DOI 10.1039/D1CY01170G. – ISSN 2044–4753

[76] Le Bideau, Damien ; Mandin, Philippe ; Benbouzid, Mohamed ; Kim, Myeongsub ; Sellier, Mathieu: Review of necessary thermophysical properties and their sensivities with temperature and electrolyte mass fractions for alkaline water electrolysis multiphysics modelling. In: *International Journal of Hydrogen Energy* 44 (2019), 2, Nr. 10, S. 4553–4569. http://dx.doi.org/10.1016/j.ijhydene.2018.12.222. – DOI 10.1016/j.ijhydene.2018.12.222. – ISSN 03603199

[77] Jang, Dohyung ; Cho, Hyun-Seok ; Kang, Sanggyu: Numerical modeling and analysis of the effect of pressure on the performance of an alkaline water electrolysis system. In: *Applied Energy* 287 (2021), 4, S. 116554. http://dx.doi.org/10.1016/j.apenergy.2021.116554. – DOI 10.1016/j.apenergy.2021.116554. – ISSN 03062619

[78] Gilliam, R ; Graydon, J ; Kirk, D ; Thorpe, S: A review of specific conductivities of potassium hydroxide solutions for various concentrations and temperatures. In: *International Journal of Hydrogen Energy* 32 (2007), 3, Nr. 3, S. 359–364. http://dx.doi.org/10.1016/j.ijhydene.2006.10.062. – DOI 10.1016/j.ijhydene.2006.10.062. – ISSN 03603199

[79] Vogt, H. ; Balzer, R.J.: The bubble coverage of gas-evolving electrodes in stagnant electrolytes. In: *Electrochimica Acta* 50 (2005), 3, Nr. 10, S. 2073–2079. http://dx.doi.org/10.1016/j.electacta.2004.09.025. – DOI 10.1016/j.electacta.2004.09.025. – ISSN 00134686

[80] Milewski, Jaroslaw ; Guandalini, Giulio ; Campanari, Stefano: Modeling an alkaline electrolysis cell through reduced-order and loss-estimate approaches. In: *Journal of Power Sources* 269 (2014), 12, S. 203–211. http://dx.doi.org/10.1016/j.jpowsour.2014.06.138. – DOI 10.1016/j.jpowsour.2014.06.138. – ISSN 03787753

[81] Stewart, Katherine ; Lair, Laurianne ; De La Torre, Brenda ; Phan, Nguyen L. ; Das, Rupak ; Gonzalez, Demar ; Lo, Roger C. ; Yang, Yu: Modeling and Optimization of an Alkaline Water Electrolysis for Hydrogen Production. In: *2021 IEEE Green Energy and Smart Systems Conference (IGESSC)*, IEEE, 11 2021. – ISBN 978–1–6654–3456–0, S. 1–6

[82] Järvinen, Lauri ; Puranen, Pietari ; Kosonen, Antti ; Ruuskanen, Vesa ; Ahola, Jero ; Kauranen, Pertti ; Hehemann, Michael: Automized parametrization of PEM and alkaline water electrolyzer polarisation curves. In: *International Journal of Hydrogen Energy* 47 (2022), 9, Nr. 75, S. 31985–32003. http://dx.doi.org/10.1016/j.ijhydene.2022.07.085. – DOI 10.1016/j.ijhydene.2022.07.085. – ISSN 03603199

[83] Mandersloot, W.G.B. ; Hicks, R.E.: Leakage currents in electrodialytic desalting and brine production. In: *Desalination* 1 (1966), 7, Nr. 2, S. 178–193. http://dx.doi.org/10.1016/S0011-9164(00)84017-5. – DOI 10.1016/S0011–9164(00)84017–5. – ISSN 00119164

[84] Veerman, J. ; Post, J.W. ; Saakes, M. ; Metz, S.J. ; Harmsen, G.J.: Reducing power losses caused by ionic shortcut currents in reverse electrodialysis stacks by a validated model. In: *Journal of Membrane Science* 310 (2008), 3, Nr. 1-2, S. 418–430. http://dx.doi.org/10.1016/j.memsci.2007.11.032. – DOI 10.1016/j.memsci.2007.11.032. – ISSN 03767388

[85] Rubinstein, I. ; Pretz, J. ; Staude, E.: Open circuit voltage in a reverse electrodialysis cell. In: *Physical Chemistry Chemical Physics* 3 (2001), Nr. 9, S. 1666–1667. http://dx.doi.org/10.1039/b010030g. – DOI 10.1039/b010030g. – ISSN 14639076

A

Effect of transfer coefficients on exchange current densities

In chapter 4, it was described that for 2D simulations, COMSOL does not allow for the sum of the anodic and cathodic transfer coefficient to be other than 1. Therefore, using the EEC model, the effect of these different transfer coefficients on the found polarisation curve was researched. These results are shown in figure A.1. Compared to transfer coefficients of 0.42 and 0.37 for the cathodic and anodic compartments, respectively, the EEC curve was shown to be steeper for lower currents, resulting in an overestimation of the cell potential.

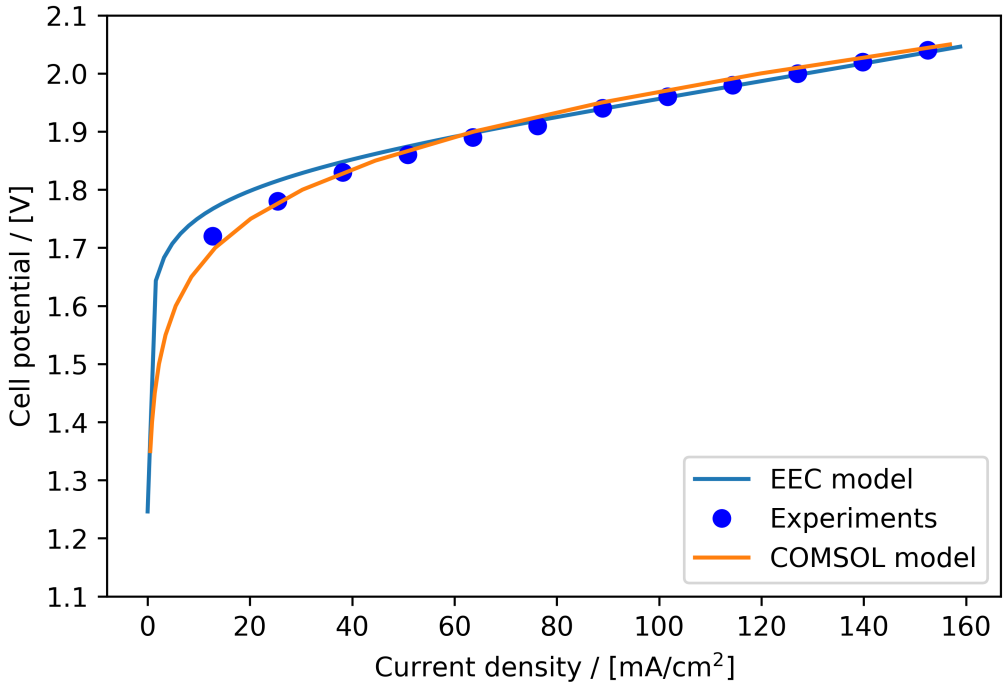

Figure A.1: 2D polarisation curve fit for α_a=0.47, α_c=0.53, with found exchange current densities of $i_{0,a}$=0.005A/m^2 and $i_{0,c}$=0.013A/m^2. Experiments and models are set at a temperature of 42.5°C and ambient pressure.

B

Monopolar versus bipolar stack configuration

For an 8-cell system using the XINTC cell geometry, the current losses occur in different cells for bipolar or monopolar electrodes, but the overall polarisation curve and Faraday efficiency remain the same. This is shown in figures B.1 (polarisation curves), B.2 (Faraday efficiency), and B.3 (leakage currents).

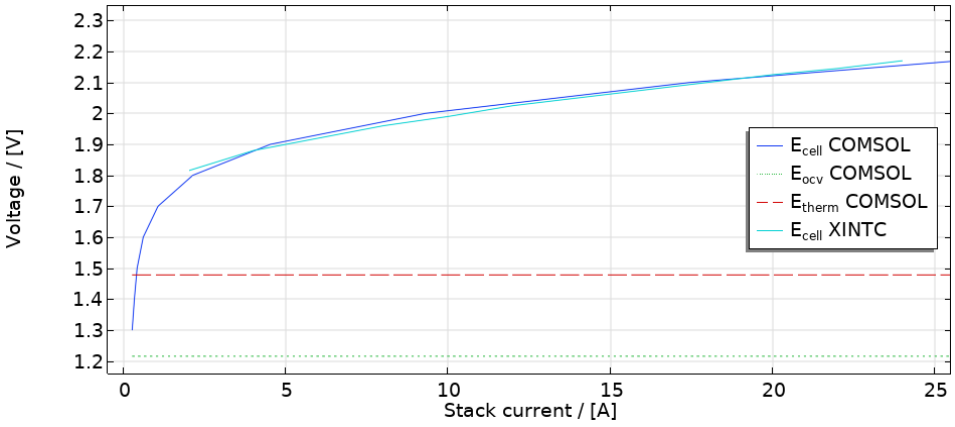

(a) Polarisation curve monopolar configuration

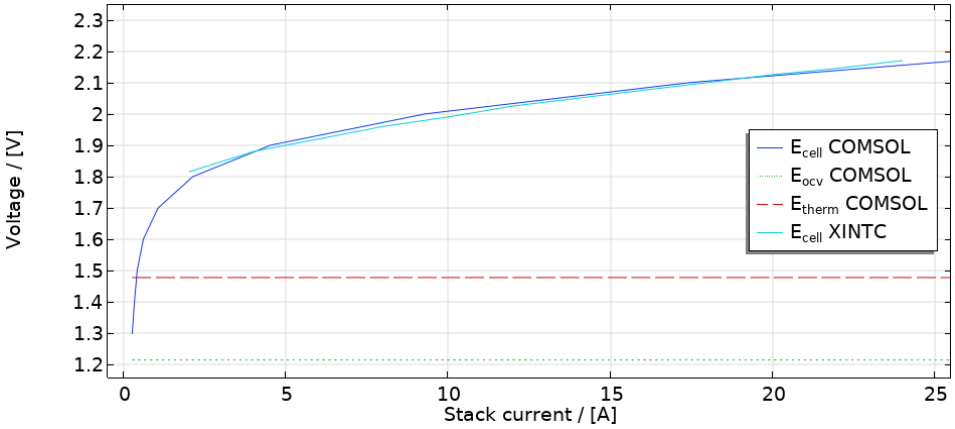

(b) Polarisation curve bipolar configuration

Figure B.1: Polarisation curve of monopolar (a) vs bipolar (b) configuration.

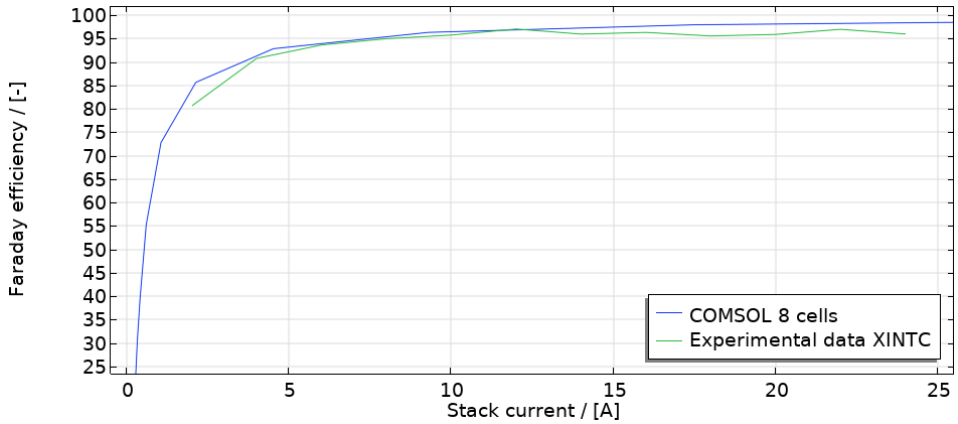

(a) Faradaic efficiency monopolar configuration

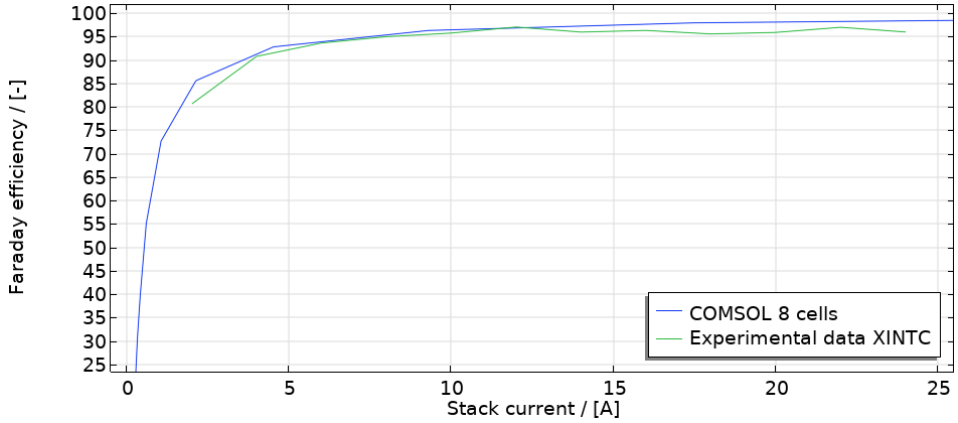

(b) Faradaic efficiency bipolar configuration

Figure B.2: Faraday efficiency of monopolar (a) vs bipolar (b) configuration.

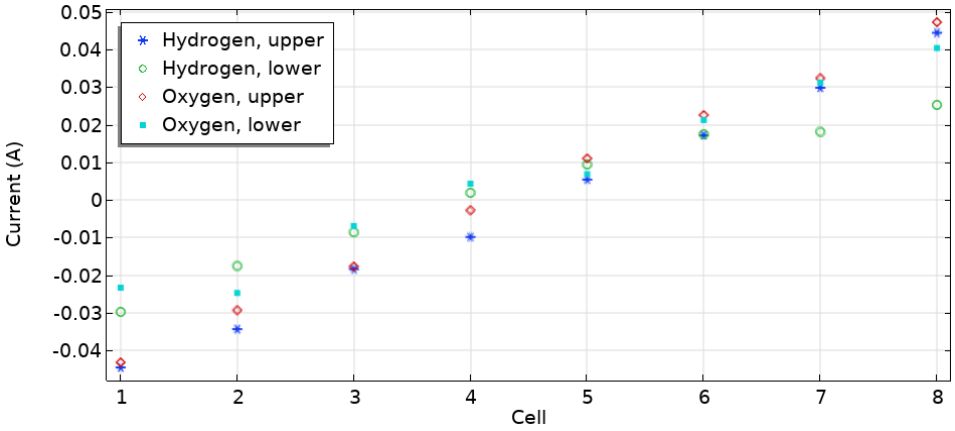

(a) Shunt currents monopolar configuration

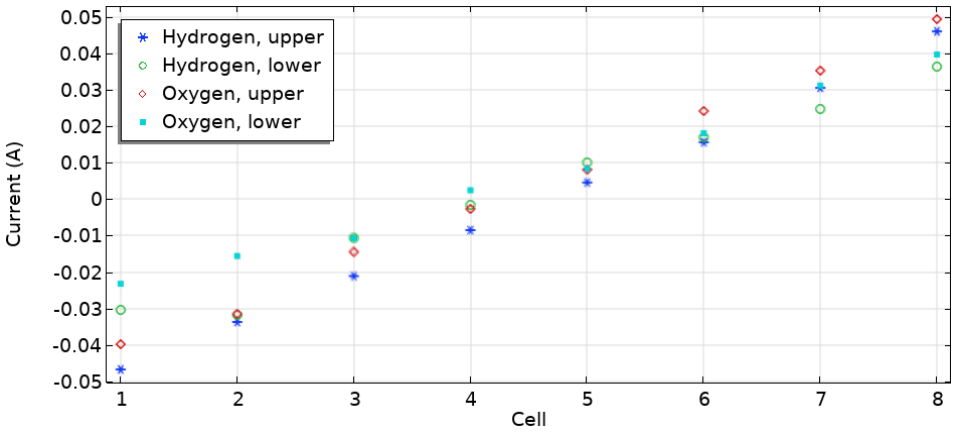

(b) Shunt currents bipolar configuration

Figure B.3: Shunt currents of monopolar (a) vs bipolar (b) configuration.